Q-space analysis of the orientationally averaged light scattering by particles of various shapes

by

Justin Birdwell Maughan

B.S., Fort Hays State University, 2013

AN ABSTRACT OF A DISSERTATION

submitted in partial fulfillment of the requirements for the degree

DOCTOR OF PHILOSOPHY

Department of Physics
College of Arts and Sciences

KANSAS STATE UNIVERSITY
Manhattan, Kansas

2020

Abstract

The scaling approach for determining the orientationally averaged light scattering in the 3d Rayleigh-Debye-Gans diffraction limit is reviewed and extended, and applied to spheroids, cylinders, hexagonal prisms, rectangular prisms, Gaussian random spheres, and droxtals. It will be shown that the scaling approach is not only able to predict the power laws that describe the diffractive light scattering by a variety of shapes, but also the coefficients to the power laws. It will also be demonstrated that the scaling approach is able to identify the crossover points between distinct scattering regimes with different power laws, due extreme aspect ratios. Application of the scaling approach to inhomogeneous spheres, and the effects on the scattering will also be demonstrated. The internal coupling parameter ρ' for any arbitrary shape will be derived and a numerical approach for calculating ρ' and the proper Rayleigh normalization for any arbitrary shape will be presented. The Rayleigh normalized orientationally averaged light scattered by spheroids, cylinders, hexagonal prisms, rectangular prisms, Gaussian random spheres, and droxtals was systematically studied. It will be shown that despite having different shapes, aspect ratios, refractive indexes, and sizes, there is an overall description of how particles scatter light. The internal coupling parameter ρ' will be shown to describe the region that the light scattering is in from the 3d Rayleigh-Debye-Gans diffraction limit to the 2d Rayleigh-Debye-Gans diffraction limit. It will also be shown that when the light scattering is in the 2d Rayleigh-Debye-Gans diffraction limit, ρ' describes the separation between the diffraction dominated region and the refraction dominated region of the scattering in q-space. Finally, it will be shown that the absorption parameter κkR, where κ is the imaginary part of the refractive index, and kR is the size parameter, is a universal parameter that describes the reduction in the

refractive effects, such as the refraction hump, generalized rainbows, and glories in the scattered light as the absorption increases.

Q-space analysis of the orientationally averaged light scattering by particles

by

Justin Birdwell Maughan

B.S., Fort Hays State University, 2013

A DISSERTATION

submitted in partial fulfillment of the requirements for the degree

DOCTOR OF PHILOSOPHY

Department of Physics
College of Arts and Sciences

KANSAS STATE UNIVERSITY
Manhattan, Kansas

2020

Approved by:

Major Professor
Dr. Christopher M. Sorensen

Copyright

Abstract

The scaling approach for determining the orientationally averaged light scattering in the 3d Rayleigh-Debye-Gans diffraction limit is reviewed and extended, and applied to spheroids, cylinders, hexagonal prisms, rectangular prisms, Gaussian random spheres, and droxtals. It will be shown that the scaling approach is not only able to predict the power laws that describe the light scattering by a variety of shapes, but also the coefficients to the power laws. It will also be demonstrated that the scaling approach is able to the crossover point between distinct scattering regimes with different power laws due to shapes with extreme aspect ratios. Application of the scaling approach to inhomogeneous spheres, and the effects on the scattering will also be demonstrated. The internal coupling parameter ρ' for any arbitrary shape will be derived and a numerical approach for calculating ρ' and the proper Rayleigh normalization for any arbitrary shape will be presented. The Rayleigh normalized orientationally averaged light scattered by spheroids, cylinders, hexagonal prisms, rectangular prisms, Gaussian random spheres, and droxtals was systematically studied. It will be shown that despite having different shapes, aspect ratios, refractive indexes, and sizes, there is an overall description of how particles scatter light. The internal coupling parameter ρ' will be shown to describe the region that the light scattering is in from the 3d Rayleigh-Debye-Gans diffraction limit to the 2d Rayleigh-Debye-Gans diffraction limit. It will also be shown that when the light scattering is in the 2d Rayleigh-Debye-Gans diffraction limit, ρ' describes the separation between the diffraction dominated region and the refraction dominated region of the scattering in q-space. Finally, it will be shown that the absorption parameter κkR, where κ is the imaginary part of the refractive index, and kR is the size parameter, is a universal parameter that describes the reduction in the refractive

effects, such as the refraction hump, generalized rainbows, and glories in the scattered light as the absorption increases.

Table of Contents

List of Figures

Acknowledgements

I would like to thank my advisor Dr. Christopher Sorensen. I do not believe I would have made it this far without his patience and endless thirst for understanding of the world we live in. I would also like to thank Dr. Amit Chakrabarti for his initial guidance when I came to Kansas State. I regret we could not have worked more together, but I understand that running the college of Arts and Science is a demanding job. Finally, I would like to thank Dr. Matthew Berg for always letting me drop by and pick his brain when I had questions.

Funding acknowledgments
“Experimental and theoretical studies of light scattering from irregularly shaped particles”, NSF AGM 12-61651, $391,000: Sorensen PI with Chakrabarti CoPI, 3/13 to 3/16.

"Q-space Scattering Power Laws and the Interior Fields of Particles" Army Research Office, $50,000, June 2014.

“Studies of Light Scattering by Particles of Arbitrary Shape”, NSF, $455,870; July 1, 2017 to December 31, 2020; Sorensen (PI) and Chakrabarti, AGS 1649783

Dedication

This work is dedicated to my Micols. To Micol my father, thank you for your endless patience and for never giving up hope that I could achieve. To Micol my son, I am sorry you had to grow up with a single father trying to make his way through a Ph.D. in physics. I know it could not have been easy to be stuck with a stressed-out, always busy dad, but I hope you are proud of me. I would like to also acknowledge my new children Jayna, Jenna, Jack and Jacob. I hope you are all proud of me as well. Finally, but certainly not least, I want to thank my beautiful wife for her patience and support without which I would not have succeeded.

Chapter 1 - Introduction

The study of how particles scatter light has been a subject of interest for many years. Lord Rayleigh published his work on light from the sky and its polarization and color in 1871 [1], and Mie published his work on the scattering by spheres in 1908 [2]. van de Hulst published one of the most well-known books on light scattering in 1957 [3], followed by the more modern works of Bohren and Huffman [4]. Some of the most recent widely known works on light scattering have come from Mishchenko and others [5–7]. Q-space analysis has also been around for many years, it has primarily been used in the fields of small angle x-ray (SAXS) and neutron scattering. Much of the SAXS formalism was produced in the 1940's and 1950's by names like Guinier and Fournet [8] and Kratky and Porod [9], while more modern works on the subject can be found by Feigin and Svergun (1987) [10]. Though the study of light scattering and SAXS have both been around for many years the application of q-space analysis in light scattering has not been widely adopted.

The distinction between typical light scattering techniques and q-space analysis comes from whether the scattering is plotted on a log-linear plot vs the scattering angle θ, or on a log-log plot vs the scattering wave vector q. When plotting on a log-log plot vs q, the scattering in the forward direction (small angles) is emphasized, which is why it is used in SAXS formulations. Even though q-space analysis emphasizes the forward directions of scattering, it also reveals quasi-universal descriptions of the scattered light with the internal coupling parameter ρ' [11–15]. It should be stressed that q-space analysis is not meant to be taken as a replacement of the analysis of light scattering vs θ. Q-space analysis provides another method to analyze the light scattering that can uncover additional information and descriptions that may not

be readily found when plotting vs θ. However, as will be shown in this work, the inverse statement is also true and in some cases θ-space provides a better picture.

Under the envelope of what is referred to as Q-space analysis is also the systematic study of light scattering. In this work the relative refractive index, size, and aspect ratio of particles with different shapes will be systematically varied. The focus will be looking for the similarities in the scattering as the parameters are varied to put together an overview of how particles scatter light. It will be shown that the forward scattering for any particle is described by the single internal coupling parameter ρ' and that the effects of absorption on the scattering can also be described by a single absorption parameter $\kappa k R_{veq}$.

1.1 Principles of Scattering

Light is a transverse electromagnetic wave that self-propagates in a direction perpendicular to the plane that the electric and magnetic waves oscillate in, or the plane of vibration. A beam of light propagating through a vacuum will do so unaffected. When a particle (or particles) are placed into the path of the beam the electromagnetic wave will interact with the charges within the particle (or particles) causing them to oscillate [4,16]. The oscillating charges are continuously accelerating and thus are radiating. Not only the field from the incident beam of light causes the charges to oscillate, but it is also the radiated fields from all of the other charges within the particle that cause the oscillation. The sum of the radiated fields from all of the charges within the particle (or particles) gives the scattered field. The oscillating charges may also transform some of the energy from the incident beam into other forms i.e. (thermal energy), this is referred to as absorption. The total amount of energy removed from the beam by either scattering or absorption is known as extinction [4,16].

To begin to describe scattering in more quantitative terms, take the beam of light, with a cross sectional area A_{beam}, and with power P_{inc} directed along the positive z axis as shown in Fig. 1.1. The intensity of this beam of light will be given by the power per unit area or $I_{inc} = P_{inc}/A_{beam}$. Now imagine that there is an arbitrary particle in the path of the beam of light as shown in Fig. 1.1. When the beam of light interacts with the particle, some of the incident power will be scattered by the particle, and some could be absorbed. Some of the power in the beam of light will not even interact with the particle and continues on unaffected.

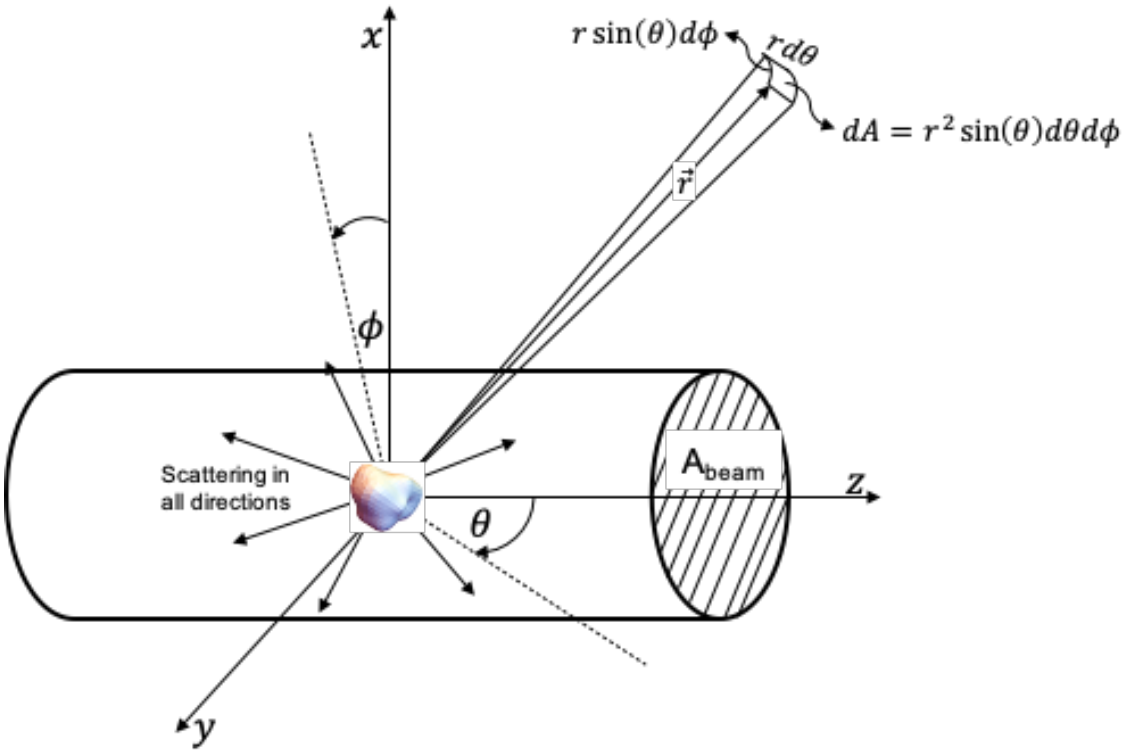

Fig. 1.1 An arbitrary particle in a beam of light will scatter in all directions. The particle can also absorb energy from the light, typically in the form of heat. The differential cross section is directly related to the amount of light scattered through the area dA.

At first glance one may think that the amount of power scattered by the particle is related to the particle's geometric cross section. If we considered the light as solely consisting of

photons that were being scattered by the particle, this may well be the case, but the dual wave and particle nature of light cannot be ignored. We can, however, define an "effective" scattering cross section. The total power scattered by the particle will be given by the product of this "effective" scattering cross section and the power per unit area of the incident beam of light

$$P_{sca} = I_{inc}C_{sca.} \tag{1.1}$$

C_{sca} is the total scattering cross section, as it tells us the total power scattered by a given particle. When a different particle is placed in the same beam of light, it will have a different C_{sca}, and a different amount of the incident power will be scattered.

Just as with the scattering if the particle absorbs some of the incident power, we can define an "effective" absorption cross section. The product of this "effective" absorption cross section and the incident power per unit area of the incident beam of light tells us the total power absorbed by the particle

$$P_{abs} = I_{inc}C_{abs}. \tag{1.2}$$

C_{abs} is the total absorption cross section, and it tells us the total power absorbed by the particle. The total power removed from the beam of light due to either scattering or absorption will be given by

$$P_{ext} = I_{inc}(C_{abs} + C_{sca}) = I_{inc}C_{ext} \tag{1.3}$$

C_{ext} is the total extinction cross section and tell us how much total power has been removed from the beam of light.

The total cross sections describe how much total power has been removed with no consideration of direction, and indeed with absorption and extinction there are no directions to consider. The total scattering cross section, as the name implies, is the sum of the scattering over all 4π steradians. What is of particular interest is the intensity scattered into a specific direction,

or how much of the scattered power is scattered into an area dA about the angles θ and ϕ as shown in Fig. 1.1. The scattered intensity into the direction θ and ϕ will be given by

$$I_{sca}(\theta,\phi) = \frac{dP_{sca}}{dA} \tag{1.4}$$

where dP_{sca} is the amount of the total scattered power P_{sca} that is scattered through the area dA. The differential area dA can be expressed in terms of a solid angle as $dA = r^2 \sin(\theta) d\theta d\phi = r^2 d\Omega$ [17] with r being the distance from the particle. Combining Eq. (1.1) and Eq. (1.4) and writing the differential area in terms of a solid angle leads to

$$I_{sca}(\theta,\phi) = \frac{I_{inc}}{r^2}\frac{dC_{sca}}{d\Omega}(\theta,\phi). \tag{1.5}$$

The term $\frac{dC_{sca}}{d\Omega}(\theta,\phi)$ in Eq. (1.5) is called the differential scattering cross section and is related to the total scattering cross section by [4]

$$C_{sca} = \int_{4\pi} \frac{dC_{sca}}{d\Omega}(\theta,\phi) d\Omega. \tag{1.6}$$

Typically, it is the differential scattering cross section that is of interest to study as it describes the angle dependent scattering in the direction described by θ and ϕ. When the differential scattering cross section is known it can be used to calculate the scattered intensity from the particle, at any distance and with any incident intensity.

Throughout this work, what will be considered is orientationally averaged scattering. Orientational averaging can be used to give the approximate behavior of many similar particles randomly oriented in a scattering volume. The incident field will always be considered as propagating in the z direction and the incident wave will be described by the wave vector $\vec{k}_{inc}$. Only elastic scattering will be considered, and so the scattered wave vector $\vec{k}_{sca}$ will have the same magnitude as the incident wave vector $|\vec{k}_{inc}| = |\vec{k}_{sca}| = k = 2\pi/\lambda$ where λ is the wavelength. The particle will scatter light in all directions, but what is measured is the light

scattered to the detector in the $\vec{k}_{sca}$ direction. The plane formed by the incident and scattering wave vectors is known as the scattering plane, this is shown in Fig. 1.2. The scattering plane will be taken to be the $z-y$ plane described by the scattering angle θ, with $\phi = \pi/2$ as shown in Fig. 1.2 unless noted otherwise.

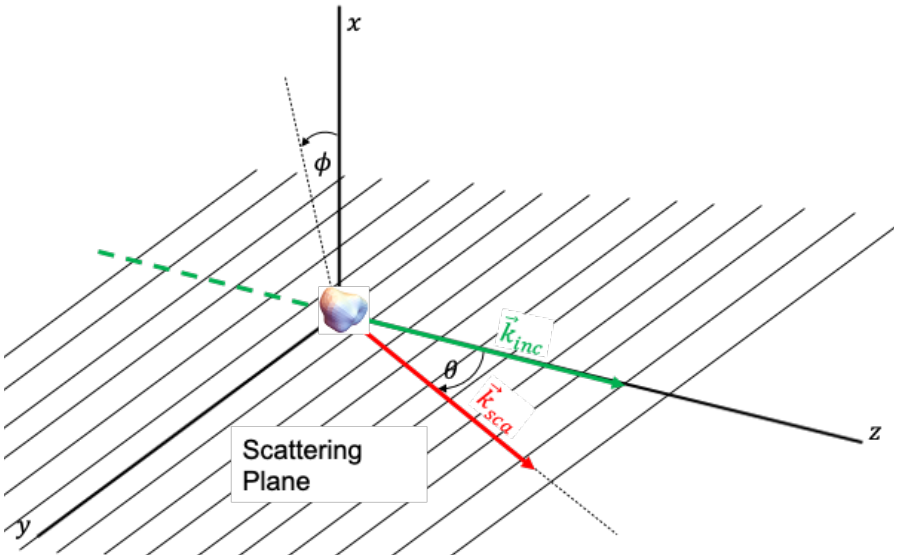

Fig. 1.2 The scattering plane is defined by the incident and scattering wave vectors, taken to be the y-z plane in this work. The scattering angle θ is measured from the z axis.

1.2 Polarization

As mentioned in the previous section, we must consider the wave nature of light, or more precisely, we must consider that light is a vector wave. We can describe an electromagnetic wave (light) propagating in the positive z direction with [18,19]

$$\vec{E} = Re(\tilde{E}_x)\hat{x} + Re(\tilde{E}_y)\hat{y} \tag{1.7}$$

$\tilde{E}_x$ and $\tilde{E}_y$ are the complex electric field components and are given by

$$\tilde{E}_x = E_{o,x}e^{i(kz-\omega t)}, \tag{1.8}$$

and

$$\tilde{E}_y = E_{o,y} e^{i(kz-\omega t+\Delta\varphi)}. \quad (1.9)$$

In Eq. (1.8) and Eq. (1.9) $E_{o,x}$ and $E_{o,y}$ are the field amplitudes, k is the wave vector magnitude given by $2\pi/\lambda$, with λ being the wavelength, ω is the angular frequency, and $\Delta\varphi$ is the phase difference between the x and y complex field components. Rewriting Eq. (1.7) using the real parts of Eq. (1.8) and Eq. (1.9) we get

$$\vec{E} = E_{o,x}\cos(kz-\omega t)\,\hat{x} + E_{o,y}\cos(kz-\omega t+\Delta\varphi)\,\hat{y}. \quad (1.10)$$

In general, an electric field described by Eq. (1.10) will be elliptically polarized. To understand this, imagine an observer looking down the z axis so that the observer is viewing the electric field vector described by Eq. (1.10) traveling toward them. The electric field vector has components in only the x-y plane, as it travels in the z direction toward the observer. What the observer would see is the electric field rotating in the x-y plane, and the tip of the electric field vector would trace out an ellipse. There are some special cases of the elliptical polarization that arise with specific values of the phase difference $\Delta\varphi$, and the field amplitudes [18].

1) If $E_{o,y} = 0$ and $E_{o,x} \neq 0$, the tip of the electric field vector will oscillate along the x-axis, and the field is said to be linearly polarized in the x-direction, vertically polarized, or polarized perpendicular to the scattering plane.
2) If $E_{o,x} = 0$ and $E_{o,y} \neq 0$, the tip of the electric field vector will oscillate along the y-axis, and the field is said to be linearly polarized in the y-direction, horizontally polarized, or polarized parallel to the scattering plane.
3) If $E_{o,x} = E_{o,y} = E_o$ and $\Delta\varphi = 0$, the tip of the electric field vector will oscillate along the $y = x$ direction, and the field is said to be linearly polarized at an angle of $+45°$ with respect to the x-axis.

4) If $E_{o,x} = E_{o,y} = E_o$ and $\Delta\varphi = \pi$, the tip of the electric field vector will oscillate along the $y = -x$ axis, and the field is said to be linearly polarized at an angle of $-45°$ with respect to the x-axis.
5) If $E_{o,x} = E_{o,y} = E_o$ and $\Delta\varphi = -\pi/2 + 2m\pi\ m = 0, \pm1, \pm2$ ..., the tip of the electric field vector will rotate clockwise tracing out a circle of radius E_o, and is said to be right circularly polarized.
6) If $E_{o,x} = E_{o,y} = E_o$ and $\Delta\varphi = \pi/2 + 2m\pi\ m = 0, \pm1, \pm2$ ..., the tip of the electric field vector will rotate counter-clockwise tracing out a circle of radius E_o, and is said to be left circularly polarized.

In this work the focus will be mainly on the scattering of light that is linearly polarized either perpendicular or parallel to the scattering plane.

To see how the polarization of the incident electric field can affect the scattering, consider an electric field incident upon a small dielectric sphere. The field will induce a force on the charged particles within the sphere and start them oscillating. In the electrostatics approximation, the field can be approximated as being uniform across the diameter of the sphere [20]. There are two conditions that must be met before being able to apply the electrostatics approximation. One condition is that the size parameter $R_{veq} \ll 1$, where R_{veq} is the radius of a sphere with the equivalent volume, which would be R in the case of a sphere. Another condition is that $|m|kR_{veq} \ll 1$ where $m = n + i\kappa$ is the complex relative index of refraction, or the ratio of the index of the scattering particle to the index of the surrounding medium [3,4]. Scattering particles, whether they are spheres or not, that meet these conditions are commonly referred to as being in the Rayleigh scattering limit.

The first condition $kR \ll 1$ is a direct comparison wavelength of the incident light and the size of the particle, as k is inversely proportional to the wavelength. When the wavelength is comparably large compared to the sphere the phase of the incident field can be taken to be relatively constant across the diameter of the sphere. When the incident field is in phase across the sphere, so will be the scattered fields, and the scattered fields will sum up constructively. The second condition considers the effects of the relative index, more precisely the imaginary part of the relative index κ on the field within the sphere. When $\kappa kR \ll 1$, the field will fully penetrate the sphere, but if it is not, the field will be absorbed before doing so and will no longer be uniform across the diameter of the sphere. Later in this work, it will be shown that κkR is a universal parameter describing the effects of absorption on the scattering from particles.

When the incident field is uniform across the sphere, the charged particles will oscillate in phase. The direction along which the particles oscillate will be the same direction that the incident electric field is polarized. The oscillating particles will radiate, and if the sphere is optically small, only the dipole terms will contribute significantly to the scattering [20]. The scattered field will have a polarization associated with it as well, which in general may be different than incident polarization. The differential scattering cross section for a small dielectric sphere, which has an incident field polarization described by $\hat{p}$, and a scattered field polarization described by $\hat{\epsilon}$ is equal to [20]

$$\frac{dC_{sca,Ray}}{d\Omega}(\theta) = k^4 R^6 \left|\frac{m^2-1}{m^2+2}\right|^2 \left[\hat{\epsilon}^* \cdot \left(\left(\hat{k}_s \times \hat{p}\right) \times \hat{k}_s\right)\right]^2 . \tag{1.11}$$

In Eq. (1.11), both $\hat{p}$ and $\hat{\epsilon}$ can be complex quantities when circularly polarized light is considered, and $\hat{k}_s$ is the unit vector pointing in the direction of the detector. The complex conjugate of $\hat{\epsilon}$ is used to correctly handle circular polarizations [20]. Using the vector identity [21]

$$\vec{A} \times \left(\vec{B} \times \vec{C}\right) = \vec{B}\left(\vec{A} \cdot \vec{C}\right) - \vec{C}\left(\vec{A} \cdot \vec{B}\right) \tag{1.12}$$

Eq. (1.11) can be expressed as

$$\frac{dC_{sca,Ray}}{d\Omega}(\theta) = k^4 R^6 \left|\frac{m^2 - 1}{m^2 + 2}\right|^2 [\hat{\epsilon}^* \cdot \hat{p}]^2 \,. \tag{1.13}$$

In Fig. 1.3 both the perpendicular (blue) and parallel (purple) polarizations are shown (double arrows) for incident (solid) and scattered (dashed) fields. In Fig. 1.3 it is clear that if the scattered field is polarized perpendicular to the scattering plane it will be polarized along the x direction and $\hat{\epsilon}_{perp} = \hat{x}$. However, for scattered fields that are parallel to the scattering plane the polarization will have a mix of both z and y components. The unit vector for parallel polarization of the scattered field will be perpendicular to $\hat{k}_s$, which in cartesian coordinates is given by

$$\hat{k}_s = \sin(\theta)\,\hat{y} + \cos(\theta)\,\hat{z}. \tag{1.14}$$

Rotating $\hat{k}_s$ by 90° in the scattering plane gives

$$\hat{\epsilon}_{par} = \begin{bmatrix} 0 & -1 \\ 1 & 0 \end{bmatrix} \begin{bmatrix} \sin(\theta) \\ \cos(\theta) \end{bmatrix} = -\cos(\theta)\,\hat{y} + \sin(\theta)\,\hat{z} \ . \tag{1.15}$$

Examining the dot product in Eq. (1.13), if the incident polarization is perpendicular (parallel) to the scattering plane, then the amount of the field scattered parallel (perpendicular) to the scattering plane will be zero as $\hat{\epsilon}^*$ and $\hat{p}$ would be perpendicular to each other by definition.

$$\frac{dC_{sca,Ray,\parallel\perp}}{d\Omega}(\theta) = \frac{dC_{sca,Ray,\perp\parallel}}{d\Omega}(\theta) = 0 \tag{1.16}$$

where the notation system used in the subscripts gives the incident polarization with the first symbol and the scattered polarization with the second. The subscript example, $\parallel\perp$ would be incident light that is polarized in a direction parallel to the scattering plane, and only considering the component of the scattered light that is polarized perpendicular to the scattering plane.

Experimentally this would be analogous to sending the scattered field through a linear polarizer that only allows light polarized perpendicular to the scattering plane to be transmitted.

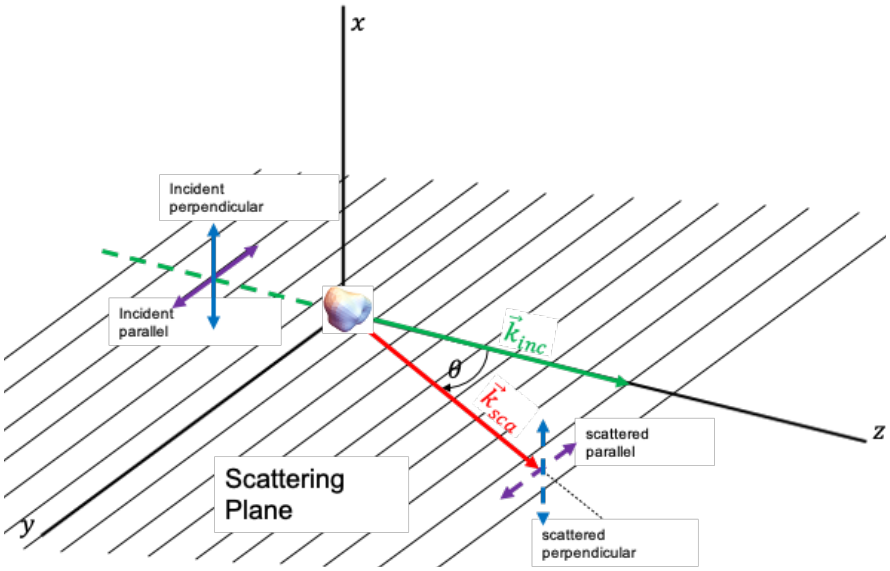

Fig. 1.3 Polarization directions with respect to the scattering plane. Purple arrows represent parallel polarization while the blue arrows represent perpendicular polarization.

When the incident field is polarized perpendicular to the scattering plane, $\hat{p} = \hat{x}$ and from Eq. (1.16) we know that the parallel component of the scattered field is zero, and so the only non-zero component of the scattered field is perpendicular to the scattering plane, $\hat{\epsilon} = \hat{x}$. The incident and scattered polarizations are parallel to each other and so the dot product will be equal to unity and the differential cross section will be given by

$$\frac{dC_{sca,Ray,\perp\perp}}{d\Omega}(\theta) = k^4 R^6 \left|\frac{m^2-1}{m^2+2}\right|^2. \tag{1.17}$$

When the incident field is polarized parallel to the scattering plane, $\hat{p} = \hat{y}$ and from Eq. (1.16) we know that the perpendicular component is zero, and so the only non-zero component of the scattered field is parallel to the scattering plane, $\hat{\epsilon} = -\cos(\theta)\,\hat{y} + \sin(\theta)\,\hat{z}$. The dot product of the incident and scattered fields will be equal to $-\cos(\theta)$, and the differential scattering cross section will be proportional to $\cos^2(\theta)$ and go as

$$\frac{dC_{sca,Ray,\parallel\parallel}}{d\Omega}(\theta) = k^4R^6\left|\frac{m^2-1}{m^2+2}\right|^2\cos^2(\theta). \tag{1.18}$$

When the incident light is unpolarized, the differential scattering cross section of the scattered field that is polarized perpendicular (parallel) to the scattering plane will be given by an average of the parallel and perpendicular incident polarizations

$$\frac{dC_{sca,Ray,U\perp}}{d\Omega}(\theta) = \frac{1}{2}\left(\frac{dC_{sca,\parallel\perp}}{d\Omega}(\theta) + \frac{dC_{sca,\perp\perp}}{d\Omega}(\theta)\right) = \frac{k^4R^6}{2}\left|\frac{m^2-1}{m^2+2}\right|^2, \tag{1.19}$$

and

$$\frac{dC_{sca,Ray,U\parallel}}{d\Omega}(\theta) = \frac{1}{2}\left(\frac{dC_{sca,\parallel\parallel}}{d\Omega}(\theta) + \frac{dC_{sca,\perp\parallel}}{d\Omega}(\theta)\right) = \frac{k^4R^6}{2}\left|\frac{m^2-1}{m^2+2}\right|^2\cos^2(\theta), \tag{1.20}$$

where the U stands for unpolarized light. Finally, if both the incident and scattered light are unpolarized the result is the sum of Eq. (1.19) and Eq. (1.20)

$$\frac{dC_{sca,Ray,UU}}{d\Omega}(\theta) = \frac{k^4R^6}{2}\left|\frac{m^2-1}{m^2+2}\right|^2\left(1+\cos^2(\theta)\right). \tag{1.21}$$

In general, Eq. (1.11)-Eq. (1.21) hold for particles of any shape as long as the electrostatic conditions are met, with the replacement of [3]

$$k^4R^6\left|\frac{m^2-1}{m^2+2}\right|^2 \rightarrow k^4V^2|\alpha(m)|^2, \qquad \left|\alpha_{sph}(m)\right| = \frac{3}{4\pi}\left|\frac{m^2-1}{m^2+2}\right| \tag{1.22}$$

where V is the volume of the particle and $\alpha(m)$ is the average volume polarizability. Fig. 1.4 shows the classic dipole pattern given by the angular behavior of Eq. (1.19)-Eq. (1.21).

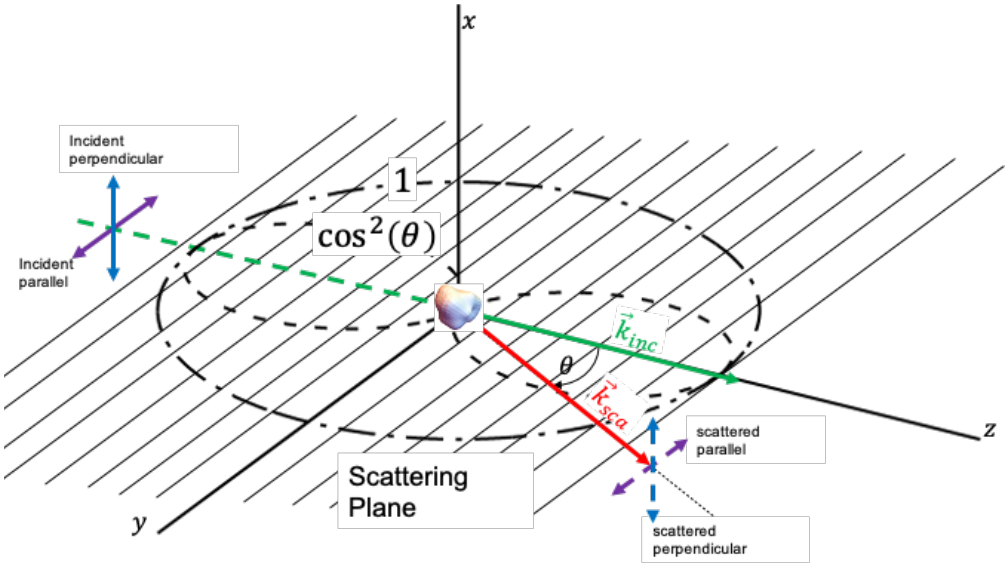

Fig. 1.4 Classic dipole pattern represented in the scattering plane. The circular dot dashed line represents the perpendicular scattering, while the dashed line is the parallel scattering.

It is clear that the polarization of the fields whether it be the incident or scattered field plays an integral role in scattering. Typically, it is the scalar intensity of the vector field that is measured by a detector and thus the information about the polarization is lost. Indeed, by examination of Eq. (1.16)-Eq. (1.21) it is apparent that the differential scattering cross sections, which are related to intensities by Eq. (1.5), have no information about the polarization state of the fields. More than one parameter will be needed to keep track of the intensities and polarization information.

1.3 Stokes Vector

As we have seen, having different polarizations of the incident field results in different angular behavior of the scattered intensity. Yet the measured intensity alone does not carry the polarization information with it. The Stokes vector, named after G. G. Stokes [18,22], is a four dimensional vector that describes not only the intensity of a wave but also the polarization state

in terms of measurable quantities. For an ideal beam of monochromatic light the elements of the Stokes vector are defined as [4,18]

$$I = I_{\parallel} + I_{\perp} \propto E_{\parallel}E_{\parallel}^{*} + E_{\perp}E_{\perp}^{*}, \tag{1.23}$$

$$Q = I_{\parallel} - I_{\perp} \propto E_{\parallel}E_{\parallel}^{*} - E_{\perp}E_{\perp}^{*}, \tag{1.24}$$

$$U = I_{+} - I_{-} \propto E_{\parallel}E_{\perp}^{*} + E_{\perp}E_{\parallel}^{*} \tag{1.25}$$

$$V = I_{R} - I_{L} \propto i\left(E_{\parallel}E_{\perp}^{*} - E_{\perp}E_{\parallel}^{*}\right). \tag{1.26}$$

Where $I_{\parallel}(\,I_{\perp})$ is the intensity of a beam of light after passing through a linear polarizer with its transmission axis parallel (perpendicular) to the scattering plane, $I_{+}(\,I_{-})$ is the intensity of a beam of light after passing through a linear polarizer with its transmission axis at a $+45^{\circ}(-45^{\circ})$ to the scattering plane. Finally, $I_{R}(\,I_{L})$ is the intensity of a beam of light after passing through a right (left) circular polarizer. In a real world experiment, the beam will not be perfectly monochromatic, but only quasi monochromatic and the stokes vectors will be given by [4,18]

$$I = I_{\parallel} + I_{\perp} \propto \langle\, E_{\parallel}E_{\parallel}^{*} + E_{\perp}E_{\perp}^{*}\rangle = \langle E_{o,x}^{2}\rangle + \langle E_{o,y}^{2}\rangle \tag{1.27}$$

$$Q = I_{\parallel} - I_{\perp} \propto \langle\, E_{\parallel}E_{\parallel}^{*} - E_{\perp}E_{\perp}^{*}\rangle = \langle E_{o,y}^{2}\rangle - \langle E_{o,x}^{2}\rangle \tag{1.28}$$

$$U = I_{+} - I_{-} \propto \langle E_{\parallel}E_{\perp}^{*} + E_{\perp}E_{\parallel}^{*}\rangle = \langle 2E_{o,x}E_{o,y}\cos(\Delta\varphi)\rangle \tag{1.29}$$

$$V = I_{R} - I_{L} \propto \langle i\left(E_{\parallel}E_{\perp}^{*} - E_{\perp}E_{\parallel}^{*}\right)\rangle = \langle 2E_{o,x}E_{o,y}\sin(\Delta\varphi)\rangle \tag{1.30}$$

Where $\langle\quad\rangle$ represents time averaging over a time interval that is long compared to the period. The last term in Eq. (1.27)-Eq. (1.30) comes from combining Eq. (1.10) with them and the fact that in this work the x direction has been denoted at perpendicular to the scattering plane while the y direction is parallel to it. All four of the Stokes vector elements I, Q, U, and V will have units of intensity, and all four elements can be measured using polarizers.

To see how the four elements of the Stokes vector provide information about the polarization state of a beam of light, Eq. (1.27)-Eq. (1.30) can be applied to beams of light with different polarizations. For an unpolarized beam of light there will be an equal amount of the light that is polarized perpendicular and parallel to the scattering plane so Eq. (1.27) gives $I = I_{o}$

where I_o is the intensity of the incident beam. Eq. (1.28) will lead to $Q = 0$ for unpolarized light. The unpolarized light will be incoherent and so the phase difference in Eq. (1.29) and Eq. (1.30) will be random with time, and the time average of $\cos(\Delta\varphi)$ and $\sin(\Delta\varphi)$ will be zero, and thus $U = V = 0$. When the light is linearly polarized perpendicular to the scattering plane $E_{\parallel} = 0$, and so $I = -Q$, and $U = V = 0$. If instead the light is linearly polarized parallel to the scattering plane $E_{\perp} = 0$, which causes $I = Q$, and $U = V = 0$. When the light is linearly polarized at a $+45^{\circ}$ angle with respect to the scattering plane, $E_{\parallel} = E_{\perp}$ and the phase difference $\Delta\varphi$=0, thus $U = I$, and $Q = V = 0$. Instead if the light is linearly polarized at a -45° angle with respect to the scattering plane, $E_{\parallel} = E_{\perp}$ and the phase difference $\Delta\varphi$=π, resulting in $U = -I$, and $Q = V = 0$. When the light is right circularly polarized, $E_{\parallel} = E_{\perp}$ and the phase difference $\Delta\varphi = -\pi/2 + 2m\pi \quad m = 0, \pm1, \pm2$ ..., thus $V = I$ and $Q = U = 0$. Instead if the light is left circularly polarized, $E_{\parallel} = E_{\perp}$ and the phase difference $\Delta\varphi = \pi/2 + 2m\pi \quad m = 0, \pm1, \pm2$ ..., thus $V = -I$ and $Q = U = 0$. The matrix representation of normalized Stokes vectors for all of these cases are shown in Fig. 1.5. In the normalized Stokes vector all of the elements are normalized by the first element I [18].

$$Un \begin{pmatrix} 1 \\ 0 \\ 0 \\ 0 \end{pmatrix} \quad \parallel \begin{pmatrix} 1 \\ 1 \\ 0 \\ 0 \end{pmatrix} \quad \perp \begin{pmatrix} 1 \\ -1 \\ 0 \\ 0 \end{pmatrix} \quad +45° \begin{pmatrix} 1 \\ 0 \\ 1 \\ 0 \end{pmatrix} \quad -45° \begin{pmatrix} 1 \\ 0 \\ -1 \\ 0 \end{pmatrix} \quad R \begin{pmatrix} 1 \\ 0 \\ 0 \\ 1 \end{pmatrix} \quad L \begin{pmatrix} 1 \\ 0 \\ 0 \\ -1 \end{pmatrix}$$

Fig. 1.5 Normalized stokes vectors for unpolarized, parallel, perpendicular, $+45°$, $-45°$, right and left circularly polarized light.

It can be worked out from Eq. (1.27)-Eq. (1.30) that $I^2 \leq Q^2 + U^2 + V^2$. The amount of the scattered light that is polarized in some fashion is given by the degree of polarization

$$P = \frac{\sqrt{Q^2 + U^2 + V^2}}{I}. \tag{1.31}$$

When $P = 1$ the light is fully polarized, and if $P < 1$ it is partially polarized. Similarly, the amount of light that is linearly polarized, whether it be perpendicular, parallel, $+45^{\circ}$, or -45° is denoted as the degree of linear polarization

$$P_l = \frac{\sqrt{Q^2 + U^2}}{I}. \tag{1.32}$$

When $P_l = 1$ the light is fully polarized and only has linearly polarized field components. Finally, the amount of light that is either right or left circularly polarized is given by the degree of circular polarization

$$P_c = \frac{\sqrt{V^2}}{I}. \tag{1.33}$$

Just as with P and P_l if $P_c = 1$, it will be fully polarized and only composed of right or left circularly polarized light. The Stokes vector for a beam of light describes the polarization state of the light in terms of readily measurable intensities. The scattering process, however, tends to change the polarization state and so a mechanism to transform the Stokes vector of the incident light into a Stokes vector for the scattered light is needed.

1.4 Mueller Matrices

When a beam of light interacts with an optical object of some form, the intensity and polarization of the light is in general transformed. How the incident light is transformed upon interaction with an optical object depends on what the object is and what direction the interaction is being viewed from. The Mueller matrix is an angle dependent, unitless 4×4 matrix that

describes the transformation of an incident intensity and polarization upon interaction with an optical object. Mathematically, the interaction is represented by a matrix multiplication, the Stokes vector representing the incident beam of light is multiplied by the Mueller matrix representing how the optical object transforms the light. The result of the matrix multiplication is a new Stokes vector representing the intensity and polarization state of the light after the interaction.

Some of the simpler optical objects that can be considered are polarizers. Fig. 1.6 shows the Muller matrices for linear polarizers with transmission axes that are parallel, perpendicular, $+45^{\circ}$, and -45° with respect to the scattering plane and right and left circular polarizers. As an example, consider an arbitrary beam of light incident upon a perpendicular polarizer, the resulting Stokes vector would be given by [18]

$$\begin{pmatrix} I_{sca} \\ Q_{sca} \\ U_{sca} \\ V_{sca} \end{pmatrix} = \frac{1}{2}\begin{pmatrix} 1 & -1 & 0 & 0 \\ -1 & 1 & 0 & 0 \\ 0 & 0 & 0 & 0 \\ 0 & 0 & 0 & 0 \end{pmatrix}\begin{pmatrix} I_{inc} \\ Q_{inc} \\ U_{inc} \\ V_{inc} \end{pmatrix} = \frac{1}{2}\begin{pmatrix} I_{inc} - Q_{inc} \\ -(I_{inc} - Q_{inc}) \\ 0 \\ 0 \end{pmatrix} \tag{1.34}$$

In Eq. (1.34) it can be seen that the scattered intensity I_{sca} is equal in magnitude but opposite in sign to Q_{sca}, which was the condition given for light polarized perpendicular to the scattering plane.

$$\underset{\frac{1}{2}\begin{pmatrix} 1 & 1 & 0 & 0 \\ 1 & 1 & 0 & 0 \\ 0 & 0 & 0 & 0 \\ 0 & 0 & 0 & 0 \end{pmatrix}}{\parallel} \qquad \underset{\frac{1}{2}\begin{pmatrix} 1 & -1 & 0 & 0 \\ -1 & 1 & 0 & 0 \\ 0 & 0 & 0 & 0 \\ 0 & 0 & 0 & 0 \end{pmatrix}}{\perp} \qquad \underset{\frac{1}{2}\begin{pmatrix} 1 & 0 & 1 & 0 \\ 0 & 0 & 0 & 0 \\ 1 & 0 & 1 & 0 \\ 0 & 0 & 0 & 0 \end{pmatrix}}{+45^{\circ}}$$

$$\underset{\frac{1}{2}\begin{pmatrix} 1 & 0 & -1 & 0 \\ 0 & 0 & 0 & 0 \\ -1 & 0 & 1 & 0 \\ 0 & 0 & 0 & 0 \end{pmatrix}}{-45^{\circ}} \qquad \underset{\frac{1}{2}\begin{pmatrix} 1 & 0 & 0 & 1 \\ 0 & 0 & 0 & 0 \\ 0 & 0 & 0 & 0 \\ 1 & 0 & 0 & 1 \end{pmatrix}}{R} \qquad \underset{\frac{1}{2}\begin{pmatrix} 1 & 0 & 0 & -1 \\ 0 & 0 & 0 & 0 \\ 0 & 0 & 0 & 0 \\ -1 & 0 & 0 & 1 \end{pmatrix}}{L}$$

Fig. 1.6 Mueller matrices for parallel, perpendicular, $+45°$, $-45°$, right and left circular polarizers.

For more complex optical objects like a scattering volume of particles, the most general Mueller matrix has 16 independent elements and is represented as

$$\begin{pmatrix} s_{11} & s_{12} & s_{13} & s_{14} \\ s_{21} & s_{22} & s_{23} & s_{24} \\ s_{31} & s_{32} & s_{33} & s_{34} \\ s_{41} & s_{42} & s_{43} & s_{44} \end{pmatrix}. \tag{1.35}$$

By making certain assumptions about the symmetries of the particles within a scattering volume the number of independent elements can be reduced. van de Hulst [3] gives a series of sets of different assumptions, the most common of which is used as follows. The scattering volume contains particles and their mirror images in equal number and in random orientations, or, the particles in the scattering volume have a plane of symmetry and are randomly oriented. These assumptions reduce the number of independent elements of the Mueller matrix to six and the Mueller matrix is given by

$$\begin{pmatrix} s_{11} & s_{12} & 0 & 0 \\ s_{12} & s_{22} & 0 & 0 \\ 0 & 0 & s_{33} & s_{34} \\ 0 & 0 & -s_{34} & s_{44} \end{pmatrix}. \tag{1.36}$$

In this work the orientationally averaged scattering from single particles will be studied, and the assumption will be made that orientationally averaging a single particle meets the assumptions that lead to Eq. (1.36). Orientationally averaging a particle also removes the angular dependence with the azimuthal angle ϕ. When the particles are spheres the number of independent elements is reduced yet again and the Muller matrix will be given by [4]

$$\begin{pmatrix} s_{11} & s_{12} & 0 & 0 \\ s_{12} & s_{11} & 0 & 0 \\ 0 & 0 & s_{33} & s_{34} \\ 0 & 0 & -s_{34} & s_{33} \end{pmatrix}. \tag{1.37}$$

The scattering Stokes vector of an orientationally averaged particle in terms of the Mueller matrix and incident Stokes vector is given by

$$\begin{pmatrix} I_{sca} \\ Q_{sca} \\ U_{sca} \\ V_{sca} \end{pmatrix} = \frac{1}{k^2 r^2} \begin{pmatrix} s_{11} & s_{12} & 0 & 0 \\ s_{12} & s_{22} & 0 & 0 \\ 0 & 0 & s_{33} & s_{34} \\ 0 & 0 & -s_{34} & s_{44} \end{pmatrix} \begin{pmatrix} I_{inc} \\ Q_{inc} \\ U_{inc} \\ V_{inc} \end{pmatrix}, \tag{1.38}$$

where the $1/k^2r^2$ in Eq. (1.38) comes from relating the incident and scattered fields, which are related by e^{ikr}/ikr and which has a magnitude squared given by $1/k^2r^2$. The inverse relationship with r^2 ensures that the amount of energy flowing through a spherical surface described by r is the same as the amount of energy flowing through a spherical surface described by $r + dr$. Comparing Eq. (1.38) and Eq. (1.5) it can be shown that the differential scattering cross sections can be written in terms of the Mueller matrix elements. When the incident field is unpolarized, Eq. (1.38) can be written as

$$\begin{pmatrix} I_{sca} \\ Q_{sca} \\ U_{sca} \\ V_{sca} \end{pmatrix} = \frac{I_{inc}}{k^2 r^2} \begin{pmatrix} s_{11} & s_{12} & 0 & 0 \\ s_{12} & s_{22} & 0 & 0 \\ 0 & 0 & s_{33} & s_{34} \\ 0 & 0 & -s_{34} & s_{44} \end{pmatrix} \begin{pmatrix} 1 \\ 0 \\ 0 \\ 0 \end{pmatrix} = \frac{I_{inc}}{k^2 r^2} \begin{pmatrix} s_{11} \\ 0 \\ 0 \\ 0 \end{pmatrix}. \tag{1.39}$$

The scattered intensity will be given by

$$I_{sca} = \frac{I_{inc} s_{11}}{k^2 r^2} = \frac{I_{inc}}{r^2} \frac{dC_{sca}}{d\Omega}(\theta), \tag{1.40}$$

leading to the differential scattering cross section for unpolarized indecent light in terms of Mueller matrix elements being given by

$$\frac{dC_{sca,UU}}{d\Omega}(\theta) = \frac{s_{11}}{k^2}. \tag{1.41}$$

Similar calculations can be done for incident light perpendicular to and parallel to the scattering plane, leading to

$$\frac{dC_{sca,\perp U}}{d\Omega}(\theta) = \frac{s_{11} - s_{12}}{k^2}, \tag{1.42}$$

$$\frac{dC_{sca,\parallel U}}{d\Omega}(\theta) = \frac{s_{11} + s_{12}}{k^2}. \tag{1.43}$$

One of the simplest Mueller matrices for a scattering particle is for Rayleigh scatters. The shape of the particle does not affect the Rayleigh Mueller matrix as long as the particle is in the Rayleigh scattering limit conditions. The general Rayleigh Mueller matrix is given by [3,4]

$$k^6V^2|\alpha(m)|^2\begin{pmatrix} \frac{1}{2}\left(1+cos^2(\theta)\right) & \frac{1}{2}\left(cos^2(\theta)-1\right) & 0 & 0 \\ \frac{1}{2}\left(cos^2(\theta)-1\right) & \frac{1}{2}\left(1+cos^2(\theta)\right) & 0 & 0 \\ 0 & 0 & cos(\theta) & 0 \\ 0 & 0 & 0 & cos(\theta) \end{pmatrix}. \tag{1.44}$$

Putting Eq. (1.44) to the test, suppose we have an incident beam of light that is polarized perpendicular to the scattering plane, that is incident about an arbitrary Rayleigh particle. The relationship between the incident and scattered Stokes vectors would be given by

$$\begin{aligned} &\begin{pmatrix} I_{sca} \\ Q_{sca} \\ U_{sca} \\ V_{sca} \end{pmatrix}_{Ray} \\ &= \frac{k^6V^2|\alpha(m)|^2}{k^2r^2}\begin{pmatrix} \frac{1}{2}\left(1+\cos^2(\theta)\right) & \frac{1}{2}\left(\cos^2(\theta)-1\right) & 0 & 0 \\ \frac{1}{2}\left(\cos^2(\theta)-1\right) & \frac{1}{2}\left(1+\cos^2(\theta)\right) & 0 & 0 \\ 0 & 0 & \cos(\theta) & 0 \\ 0 & 0 & 0 & \cos(\theta) \end{pmatrix}\begin{pmatrix} I_{inc} \\ -I_{inc} \\ 0 \\ 0 \end{pmatrix} \\ &= \frac{I_{inc}k^6V^2|\alpha(m)|^2}{k^2r^2}\begin{pmatrix} 1 \\ -1 \\ 0 \\ 0 \end{pmatrix}. \end{aligned} \tag{1.45}$$

The scattered intensity will be given by

$$I_{sca,Ray,\perp U} = \frac{I_{inc}}{r^2}k^4V^2|\alpha(m)|^2\,, \tag{1.46}$$

and the differential scattering cross-section will be

$$\frac{dC_{sca,Ray,\perp U}}{d\Omega}(\theta) = k^4V^2|\alpha(m)|^2. \tag{1.47}$$

Eq. (1.47) is consistent with Eq. (1.17) if the specific details of the spherical result in Eq. (1.17) are replaced with the general result by Eq. (1.22). Further on in this work, much of the scattering results will be Rayleigh normalized, which is the normalization of the differential scattering cross section of a particle by Eq. (1.47). Now that much of the groundwork for a discussion on

scattering has been covered, we can begin to look at the scattering in more detail beginning with the structure factor and diffraction.

Chapter 2 - Q-space Analysis of Diffraction

To begin the q-space analysis of the scattering by particles in general, a logical first step is the analysis of diffraction. As will be shown in the following chapters, when the internal coupling parameter $\rho' < 1$, the scattering will be in 3d diffraction limit. As the internal coupling parameter increases toward and above unity, the scattering will leave the 3d diffraction limit. When the internal coupling parameter reaches $\rho' \sim 30$, the scattering in the forward direction will again begin to follow a diffraction limit, but it will be the 2d diffraction limit. Thus, the understanding of diffraction is of critical importance.

2.1 Structure Factor

To begin a more detailed look at how shapes scatter light we will begin in the $|m-1|$, $\rho = 2kR_{veq}|m-1| < 1$ limit, where ρ is known as the phase shift parameter. This limit is commonly referred to as the Rayleigh-Gans limit or Rayleigh-Debye-Gans (RDG), the latter of which will be used here [3,4]. In the 3d RDG limit, we consider the particle to be discretized into scattering elements dv. With the $|m-1|$ condition, the scattering elements can be considered to be weakly scattering so in a first approximation they are considered to scatter independently. The $\rho < 1$ condition allows for the field at each element to be taken as the incident field, as the phase shift is small within the particle[4]. It will be shown in the following chapters that when the internal coupling parameter $\rho' < 1$, the scattering will be in this limit.

Beginning a discussion of the structure factor, we will describe the scattering wave vector $\vec{q}$. We will follow closely the descriptions given in [23,24], and the description of the scattering

wave vector will naturally lead into a description of the structure factor. Consider a small, point-like scattering element at a position described by $\vec{r}$, with a volume dv as shown in Fig. 2.1. Also consider a mono-chromatic plane wave incident upon this scattering element and described by an incident wave vector $\vec{k}_{inc}$, which for our purposes will be taken to be pointing in the positive z direction as shown in Fig. 2.1. Only elastic scattering will be considered in this work. When the scattering is elastic, the magnitude of the incident wave vector will be equal to the magnitude of the scattered wave vector. The incident wave at the scattering element will be given by

$$E_{inc}(\vec{r}) = E_o e^{i\vec{k}_{inc}\cdot\vec{r}} \tag{2.1}$$

where E_o is the incident wave amplitude and may be a complex quantity.

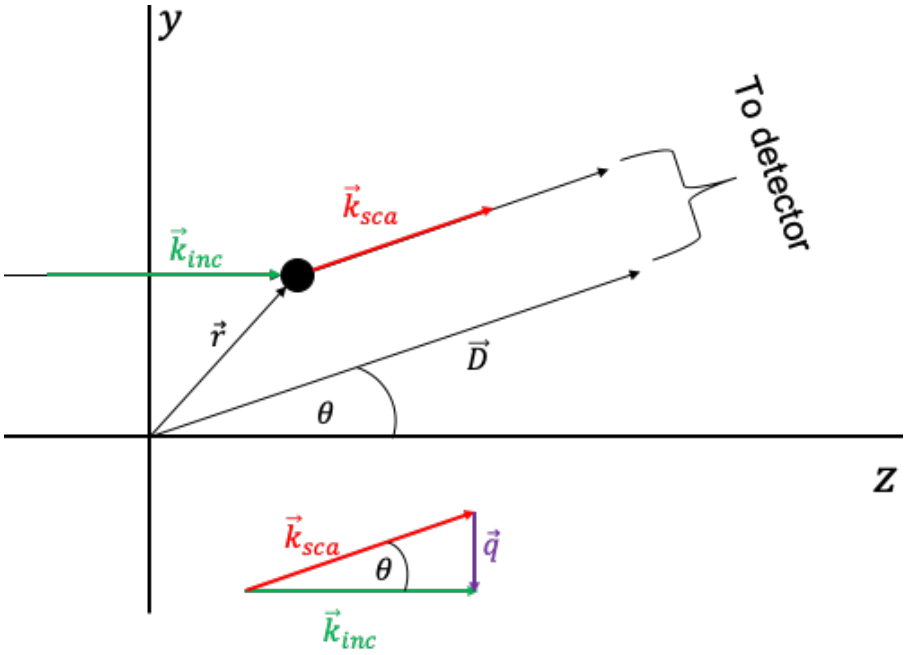

Fig. 2.1 Diagram of light scattering from a volume element, with incident wave vector $\vec{k}_{inc}$ and scattered wave vector $\vec{k}_{sca}$. The volume element at $\vec{r}$, black dot, scatters in all directions but what is measured is the light scattered in the direction θ to the detector.

The scattering element will scatter the field isotopically. What is measured in this instance will be the field that is scattered in the direction of the scattered wave vector $\vec{k}_{sca}$, out to the detector located at $\vec{D} \gg \vec{r}$ as shown in Fig. 2.1. The scattered field at $\vec{D}$ will then be given by [3,20]

$$E_{sca}(\vec{R}) = E_o k^2 dv |\alpha(m)| \frac{e^{i\vec{k}_{sca}\cdot\vec{D}}}{|\vec{D}-\vec{r}|} e^{i(\vec{k}_{inc}-\vec{k}_{sca})\cdot\vec{r}} \tag{2.2}$$

the term $|\vec{D}-\vec{r}|$ is the distance from the scattering volume to the detector. Since $\vec{D} \gg \vec{r}$ the distance from the scattering volume to the detector can be approximated as D. The scattering wave vector $\vec{q}$ is defined as the difference between the incident and scattered wave vector and has a magnitude of $q = 2k\sin(\theta/2)$ as shown in Fig. 2.1. To simplify Eq. (2.2) we can substitute $\vec{q}$ for $\vec{k}_{inc} - \vec{k}_{sca}$ and D in for $|\vec{D}-\vec{r}|$, also realizing that because $\vec{D} \gg \vec{r}$, $\vec{D}$ and $\vec{k}_s$ can be taken to be pointing in the same direction. Thus, their dot product is equal to the product of their magnitudes. With these simplifications Eq. (2.2) can be expressed as

$$E_{sca}(\vec{q}) = E_o k^2 dv |\alpha(m)| \frac{e^{ikD}}{D} e^{i\vec{q}\cdot\vec{r}}. \tag{2.3}$$

Now consider N scattering elements making up a particle. The total field from the N scattering elements will be given by the sum of the individual fields from each scattering element. The total field at $\vec{D}$ due to N scattering elements will be given by

$$E_{Tot,sca}(\vec{q}) = E_o k^2 dv |\alpha(m)| \frac{e^{ikD}}{D} \sum_{j=1}^{N} e^{i\vec{q}\cdot\vec{r}_j}, \tag{2.4}$$

where $\vec{r}_j$ is the position of the jth scattering element. The scattered intensity will then be given by the magnitude squared of Eq. (2.4) leading to

$$I_{sca,RDG}(\vec{q}) = \frac{I_o}{D^2} k^4 dv^2 |\alpha(m)|^2 \left| \sum_{j=1}^{N} e^{i\vec{q}\cdot\vec{r}_j} \right|^2. \tag{2.5}$$

The last term in Eq. (2.5) is the structure factor[20]

$$S(\vec{q}) = \left| \sum_{j=1}^{N} e^{i\vec{q}\cdot\vec{r}_j} \right|^2 . \tag{2.6}$$

Comments must be made here on the normalization of the structure factor in Eq. (2.6). Both Bohren and Huffman and van de Hulst [3,4] only define the structure factor as a continuous integral which they normalize by the volume squared. Normalization by the volume squared would be akin to normalization by N^2. Jackson [20], however, defines the structure as it has been in Eq. (2.6) which is the definition that will be used in this work. Ultimately which normalization to use is a matter of choice as long as it is used consistently. Eq. (2.6) can also be expressed as a double summation[20]

$$S(\vec{q}) = \sum_{j}^{N} \sum_{l}^{N} e^{i\vec{q}\cdot(\vec{r}_j - \vec{r}_l)}. \tag{2.7}$$

In Eq. (2.7) it can be seen that the structure factor depends solely on the physical distribution of scattering elements, or the structure of the scatterer[20], hence the name. The structure factor can be converted into an integral, which are generally easier to work with than summations, by using the fact that

$$N = \sum\nolimits_{j}^{N} = \int n(\vec{r}) d\,\vec{r} \tag{2.8}$$

where $n(\vec{r})$ is a number density function defined by

$$n(\vec{r}) = \sum_{j}^{N} \delta\left(\vec{r} - \vec{r}_j\right). \tag{2.9}$$

Combining Eq. (2.6), Eq. (2.8), and Eq. (2.9) leads to

$$S(\vec{q}) = \left| \sum_{j}^{N} e^{i\vec{q}\cdot\vec{r}_j} \right|^2 = \left| \int n(\vec{r}) e^{i\vec{q}\cdot\vec{r}}\, d\vec{r} \right|^2 . \tag{2.10}$$

In Eq. (2.10) it can be seen that the structure factor is the normalized Fourier transform squared of the density distribution of the particle. The Fourier transform takes the density function from a real space function to a reciprocal inverse space function of q.

So far, polarization effects of the fields have not been considered. Each of the scattering elements can be considered to be Rayleigh scatterers. Each of the Rayleigh scattering elements will have the same polarization dependence, and angular dependence is described for Rayleigh scatterers in chapter 1. The scattered Stokes vector for a three-dimensional particle in the RDG limit can be related to the incident Stokes vector by

$$\begin{pmatrix} I_{sca} \\ Q_{sca} \\ U_{sca} \\ V_{sca} \end{pmatrix}_{RDG} = \frac{k^4 dv^2 |\alpha(m)|^2}{r^2} S(q) \begin{pmatrix} \frac{1}{2}\left(1+\cos^2(\theta)\right) & \frac{1}{2}\left(\cos^2(\theta)-1\right) & 0 & 0 \\ \frac{1}{2}\left(\cos^2(\theta)-1\right) & \frac{1}{2}\left(1+\cos^2(\theta)\right) & 0 & 0 \\ 0 & 0 & \cos(\theta) & 0 \\ 0 & 0 & 0 & \cos(\theta) \end{pmatrix} \begin{pmatrix} I_{inc} \\ Q_{inc} \\ U_{inc} \\ V_{inc} \end{pmatrix}. \tag{2.11}$$

Comparing Eq. (2.11) and Eq. (1.45) it can be seen that the distinction is the introduction of the structure factor $S(q)$. In Eq. (2.11) the vector dependence on q has been dropped in consideration that Eq. (2.11) represents orientationally averaged scattering. If the incident polarization is unpolarized the scattered intensity in the RDG limit is given by

$$I_{sca,RDG,UU} = \frac{I_{inc}}{r^2}\frac{1}{2}\left(1+\cos^2(\theta)\right)k^4 dv^2 |\alpha(m)|^2 \, S(q). \tag{2.12}$$

Eq. (2.12) is the same result found in van de Hulst section 7.1, with the exception of an approximation used for $|\alpha(m)|^2$, and some different notation. The differential scattering cross section is then given by

$$\frac{dC_{sca,RDG,UU}}{d\Omega}(\theta) = \frac{1}{2}\left(1+\cos^2(\theta)\right)k^4 dv^2 |\alpha(m)|^2 \, S(q). \tag{2.13}$$

When the incident light is polarized parallel to the scattering plane the differential scattering cross section will be

$$\frac{dC_{sca,RDG,\parallel U}}{d\Omega}(\theta) = \cos^2(\theta) k^4 dv^2 |\alpha(m)|^2 \, S(q). \tag{2.14}$$

Finally, when the incident light is polarized perpendicular to the scattering plane the differential scattering cross section will be

$$\frac{dC_{sca,RDG,\perp U}}{d\Omega}(\theta) = k^4 dv^2 |\alpha(m)|^2 \, S(q). \tag{2.15}$$

and when Eq. (2.11) is Rayleigh normalized it will be equal to the structure factor

$$\frac{dC_{sca,RDG,\perp U}}{d\Omega}(\theta) \Big/ \frac{dC_{sca,Ray,\perp U}}{d\Omega}(\theta) = \frac{1}{N^2} S(q). \tag{2.16}$$

The primary focus of this work will be on the scattering due to incident light that is polarized perpendicular to the scattering plane. Doing so removes the angular dependences due to polarization and leaves those due to changes in structure.

2.2 Diffraction

Diffraction generally considers just the wave aspect of an electromagnetic wave incident upon a particle or screen, i.e. the structure factor. All of the scattered waves from scattering elements at the detector are summed up as in Eq. (2.10). Most students are introduced to it in their first year of physics and are taught to find the minima of the single slit diffraction pattern. Further on in more advanced classes they begin to study Fraunhofer diffraction as presented in Hecht[25]. Instead of approaching diffraction as most texts, Eq. (2.10) can be applied, and the square of the Fourier transform of the number density can be evaluated. Ultimately it will be shown that evaluating the Fourier transform in Eq. (2.10) to find the structure factor is the equivalent of Fraunhofer diffraction.

Consider an opaque screen with a small slit of length w and height $h \gg w$, or a thin wire with the same dimensions. Either a slit or wire will produce equivalent intensity patterns according to Babinet's principle of complementary screens [20,25]. Also consider a monochromatic plane wave incident upon the slit (wire) and propagating in positive z direction and perpendicular to the slit (wire) which is located at $z = 0, x = 0$. The slit (wire) will be taken to lie directly along the $y - axis$ from $-w/2 \leq y \leq w/2$. The density function in Eq. (2.10), $n(\vec{r})$ will then be a simple step function

$$n(\vec{r}) = \begin{cases} n = \frac{N}{w} & x = 0, \quad -w/2 \leq y \leq w/2, \quad z = 0 \\ 0 & x \neq 0, \quad y < -w/2, \quad y > w/2, z \neq 0 \end{cases}. \tag{2.17}$$

The $\vec{q} \cdot \vec{r}$ in Eq. (2.10) can be simplified as well due to the position vector only pointing along the $y - axis$, and so $\vec{r} = y\hat{y}$. With the position vector only pointing along the y-axis, only the y component of the dot product will survive and $\vec{q} \cdot \vec{r} = q_y y$. Eq. (2.10) can now be expressed in terms of Eq. (2.17) and $q_y y$ as

$$S_{slit}(\vec{q}) = \left| \int_{-\frac{w}{2}}^{\frac{w}{2}} n e^{iq_y y}\, dy \right|^2 = \left| \frac{N}{w} \int_{-\frac{w}{2}}^{\frac{w}{2}} e^{iq_y y}\, dy \right|^2 = N^2 \mathrm{sinc}^2\left(\frac{w}{2} q_y\right), \tag{2.18}$$

where the $\mathrm{sinc}(x) = \sin(x)/x$. As for q_y, we can go back to the original definition of the scattering wave vector

$$\vec{q} = \vec{k}_{inc} - \vec{k}_{sca} = k\hat{z} - k\cos(\theta)\,\hat{z} - k\sin(\theta)\hat{y} \tag{2.19}$$

$$q_y = -k\sin(\theta)\hat{y}. \tag{2.20}$$

Inserting Eq. (2.20) into Eq. (2.18) and using the fact that $\sin(-x) = -\sin(x)$ leads to

$$S_{slit}(\vec{q}) = N^2 \mathrm{sinc}^2\left(\frac{w}{2} k \sin(\theta)\right) = N^2 \mathrm{sinc}^2\left(\frac{w}{2} q_y\right). \tag{2.21}$$

The steps leading up to Eq. (2.21) are essentially Fraunhofer diffraction, and even if the approach is different than what is taken in most texts [19,25] the result is the same. The first minimum of Eq. (2.21) is found when

$$\theta \simeq \frac{\lambda}{w}. \tag{2.22}$$

The same approach can be taken for a circular aperture (thin disk). Consider a circular aperture (thin disk) described by a radius a. Take the aperture (thin disk) to be oriented in the $x-y$ plane so that the position vector $\vec{r} = r\cos(\phi)\,\hat{x} + r\sin(\phi)\hat{y}$. The scattering wave vector will still be given by Eq. (2.19), and the dot product will again be given by $\vec{q}\cdot\vec{r} = q_y y\sin(\phi) = -k\sin(\theta)r\sin(\phi)\,\hat{y}$. The density function can be defined as

$$n(\vec{r}) = \begin{cases} n = \frac{N}{\pi a^2} & r = \sqrt{x^2+y^2} \le a, \quad z = 0 \\ 0 & r = \sqrt{x^2+y^2} > a, \quad z \neq 0 \end{cases}. \tag{2.23}$$

The structure factor for a circular aperture (thin disk) can be expressed as

$$S_{disk}(\vec{q}) = \left| \int_0^a \int_0^{2\pi} n e^{iq_y r\sin(\phi)}\, r dr d\phi \right|^2 = \left| \frac{N}{\pi a^2} \int_0^a \int_0^{2\pi} e^{iq_y r\sin(\phi)}\, r dr d\phi \right|^2 \tag{2.24}$$

where πa^2 is the area of the aperture or disk. The integral over the azimuthal angle ϕ can be related to the zeroth order Bessel function by [21]

$$2\pi J_0(x) = \int_0^{2\pi} e^{ix\sin(\phi)}\, d\phi. \tag{2.25}$$

Using the relationship in Eq. (2.25) to evaluate the inner integral in Eq. (2.24) leads to

$$S_{disk}(\vec{q}) = \left| \frac{N}{\pi a^2} \int_0^a 2\pi r J_0(q_y r) dr \right|^2. \tag{2.26}$$

Making substitution into Eq. (2.26) of $u' = q_y r,\ u = q_y a\,, du' = q_y dr$

$$S_{disk}(\vec{q}) = \left| \frac{2N}{a^2 q_y^2} \int_0^u u' J_0(u') du' \right|^2. \tag{2.27}$$

The integration in Eq. (2.27) is given by the relationship [21]

$$\int_0^u u' J_0(u') du' = u J_1(u). \tag{2.28}$$

Finally, the structure factor of a circular aperture (thin disk) is given by

$$S_{disk}(\vec{q}) = N^2 \left| \frac{2J_1(q_y a)}{q_y a} \right|^2 = N^2 \left| \frac{2J_1(ak\sin(\theta))}{ak\sin(\theta)} \right|^2 . \tag{2.29}$$

Eq. (2.29) is a well-known result for circular aperture (thin disk) diffraction and can be found in many places, [19,21,25] are but a few. Again, we have arrived at the Fraunhofer diffraction result though we started differently than in most texts. The first minimum of Eq. (2.29) will be when

$$\theta \simeq 1.22 \frac{\lambda}{2a}. \tag{2.30}$$

Next Eq. (2.10) can be evaluated for the diffraction from a sphere of radius R. The density function will be given by

$$n(\vec{r}) = \begin{cases} n = \frac{N}{V} & r = \sqrt{x^2 + y^2 + z^2} \le R \\ 0 & r = \sqrt{x^2 + y^2 + z^2} > R \end{cases}. \tag{2.31}$$

Eq. (2.10) will become

$$S_{sphere}(\vec{q}) = \left| \int_0^R \int_0^{2\pi} \int_0^{\pi} n e^{i\vec{q}\cdot\vec{r}} r^2 \sin(\theta) d\theta \, d\phi dr \right|^2 \tag{2.32}$$

and taking advantage of the symmetry of a sphere, we can orient the coordinate system such that $\vec{q}$ is pointing in the z direction. Arranging the coordinate means that the angle between $\vec{q}$ and every position vector within the sphere is the polar angle θ. The dot product $\vec{q} \cdot \vec{r} = qr\cos(\theta)$, also to ease integration $\sin(\theta)d\theta = d(\cos(\theta))$ and Eq. (2.32) becomes

$$S_{sphere}(q) = \left| \frac{2\pi N}{V} \int_0^R \int_{-1}^{1} e^{iqr\cos(\theta)} r^2 d(\cos(\theta)) dr \right|^2 . \tag{2.33}$$

The vector dependence on q has been dropped as we can take this to be orientationally average when we could not for single slit and circular aperture. Integration over $d(\cos(\theta))$ leads to

$$S_{sphere}(q) = \left| \frac{4\pi N}{V} \int_0^R \frac{r^2 \sin(qr)}{qr} dr \right|^2 , \tag{2.34}$$

and finally, evaluating the integral over dr

$$S_{sphere}(q) = \left| 3N \frac{(sin(qR) - qR\, cos(qR))}{(qR)^3} \right|^2 = \frac{9N^2}{(qR)^6} (sin(qR) - qR\, cos(qR))^2 \tag{2.35}$$

or in terms of the scattering angle θ

$$S_{sphere}(q) = \frac{9N^2}{\left(2k \sin\left(\frac{1}{2}\theta\right)R\right)^6} \left(\sin\left(2k \sin\left(\frac{1}{2}\theta\right) R\right) - 2k \sin\left(\frac{1}{2}\theta\right) R \cos\left(2k \sin\left(\frac{1}{2}\theta\right) R\right)\right)^2 \tag{2.36}$$

The first minimum of Eq. (2.36) is found when

$$\theta \simeq 1.43 \frac{\lambda}{2R}. \tag{2.37}$$

In Fig. 2.2, Eq. (2.21), Eq. (2.29), and Eq. (2.35) have been plotted vs the scattering angle θ on a log-linear plot and also plotted vs qR_{eq} on a log-log plot, where R_{eq} is an equivalent radius i.e. $w/2$ for a wire, a for a disk, R for a sphere. Fig. 2.2 demonstrates the benefits of plotting the scattering vs the unitless qR_{eq} on a log-log plot. In Fig. 2.2(a) a series of ripples is seen with no readily quantifiable features to identify. In Fig. 2.2(b), however, quantifiable features are shown in the scattering. First, in the forward scattering lobe when $qR_{eq} < 1$, the scattering is constant with qR_{eq}. Second, in the Guinier regime when $qR_{eq} \sim 1$, $q^{-1} \sim R_{eq}$ which allows for the retrieval of particle sizes from the scattering using Guinier analysis [8,26].

After the Guinier regime is the Porod, or power law, regime. The ripples in the scattering follow a power law in this regime. The slope of the power law follows Porod's law which says that the slope will go as $-(2D_m - D_s)$ [27], where D_m is the mass scaling dimension and D_s is the surface scaling dimension. For a thin wire $D_m = 1$ and $D_s = 0$ leading to a slope of -2, while a thin disk would have $D_m = 2$ and $D_s = 1$ giving a slope of -3. A sphere would have a

$D_m = 3$ and $D_s = 2$ and a slope of -4. When examining Fig. 2.2(b) in the power law regime for the thin wire and disk, there is a distinct spike in the structure factor at large qR_{eq}. Fig. 2.2(a) shows that the structure factor is symmetric about $\theta = 90°$ for the thin wire and disk, this is what leads to the spike in Fig. 2.2(b). This insight is not readily available from Fig. 2.2(b), demonstrating that while plotting log-log vs qR_{eq} reveals insights into the scattering behavior, plotting vs the scattering angle provides insights as well and neither view should be ignored.

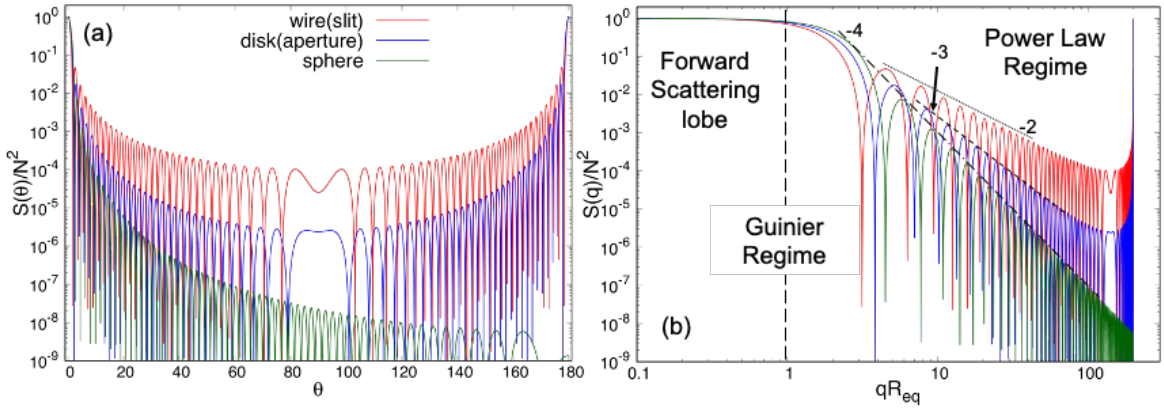

Fig. 2.2 The structure factor of a wire, disk and sphere vs the scattering angle θ in (a) and qR_{eq} in (b).

At the beginning of these diffraction derivations for the slit (thin wire), circular aperture (thin disk), and a sphere, it was stated that generally with diffraction only the wave nature is considered. To fold the diffraction into the overall picture of light scattering though, the polarization cannot be ignored. For a sphere, the inclusion of polarizations is already taken care of with Eq. (2.11), but for 1D and 2D diffraction changes to Eq. (2.11) must be made. To understand why, consider that Eq. (2.26) is dependent on q, where Eq. (2.21) and Eq. (2.29) are dependent on q_y. q_y is symmetric about $\theta = 90°$, and so the structure factor will increase past $\theta = 90°$ and will be equal in the forward and backward directions. Yang and Liou [28,29] have derived an what they refer to as an "improved scattering amplitude matrix" that addresses this

issue for 2D diffraction with the addition of a $\left(1+\cos(\theta)\right)^2/4$ term, this term is similar to the square of the "obliquity factor" arrived at through Kirchhoff's scalar diffraction theory in Hecht , but Yan and Liou use a full vector analysis instead of scalar. The addition of the a $\left(1+\cos(\theta)\right)^2/4$ term leads to [3,30]

$$\begin{pmatrix} I_{sca} \\ Q_{sca} \\ U_{sca} \\ V_{sca} \end{pmatrix}_{RDG,2D} = \left(\frac{k^2 dA^2}{r^2 4\pi^2} S(q)\left(1+\cos(\theta)\right)^2/4\right) \mathrm{x} \begin{pmatrix} \frac{1}{2}\left(1+\cos^2(\theta)\right) & \frac{1}{2}\left(\cos^2(\theta)-1\right) & 0 & 0 \\ \frac{1}{2}\left(\cos^2(\theta)-1\right) & \frac{1}{2}\left(1+\cos^2(\theta)\right) & 0 & 0 \\ 0 & 0 & \cos(\theta) & 0 \\ 0 & 0 & 0 & \cos(\theta) \end{pmatrix} \begin{pmatrix} I_{inc} \\ Q_{inc} \\ U_{inc} \\ V_{inc} \end{pmatrix}, \tag{2.38}$$

where dA is the area element of the projected area in the direction of the incident field. Eq. (2.38) describes what will be referred to as the 2d diffraction or 2d RDG limit. Fig. 2.3 shows the forward normalized scattered intensity for a slit (thin wire), circular aperture (thin disk), and a sphere in the diffraction or RDG limit plotted using Eq. (2.38). The curves in Fig. 2.3 demonstrate the behavior of the scattering from a thin wire and thin disk at angles $\theta > 90°$, when Eq. (2.38) is used. Also notice in Fig. 2.3 that the angles below $< 90°$, and the slopes in the power law regime remain unaffected.

The importance of 2D diffraction in the light scattering from 3D particles comes in when the particles have size parameters $kR_{veq} \gg 1$ and $\rho = 2kR_{veq}|m-1| \gg 1$ [3]. Under these conditions geometric optics approximation can be applied to calculate scattering by the particles [3,31]. In the forward most directions the scattering in the geometric optics approximation goes as the 2D diffraction of the projection of the particle in the direction of the incident field. It will be shown later in this work that by looking at the ratio of the Rayleigh scattering limit, and the

geometric limit, a single parameter can be derived that describes the behavior of the scattering in the forward directions from the Rayleigh limit to the geometric limit.

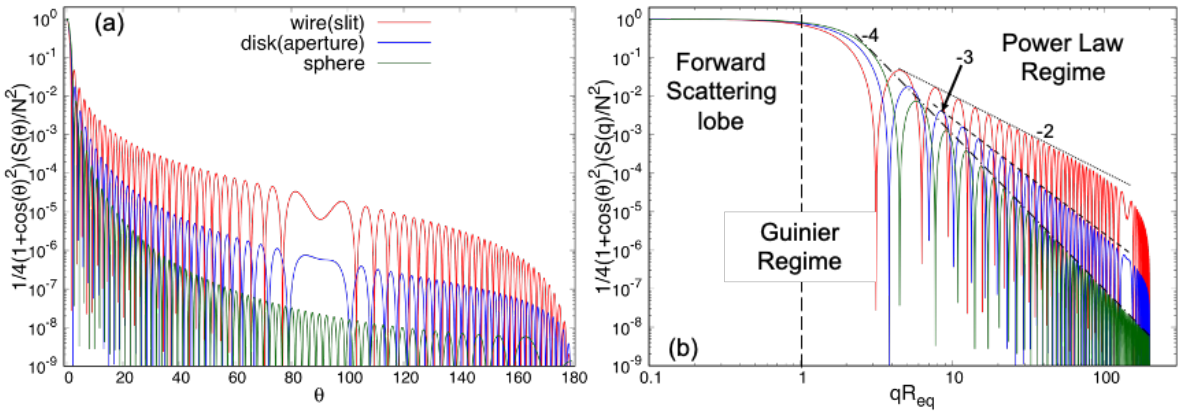

Fig. 2.3 The structure factor of a wire, disk and sphere times $\left(1+\cos(\theta)\right)^2/4$ vs the scattering angle θ in (a) and qR_{eq} in (b).

The analytical evaluation of Eq. (2.10) has been demonstrated for a single slit (thin wire), circular aperture (thin disk), and a sphere. Eq. (2.10) is valid for particles of any shape but can become extremely complicated to evaluate analytically. When more complicated particle shapes need to be evaluated, Eq. (2.7) can be employed to calculate the structure factor numerically. The exponential term Eq. (2.7) can be expressed in terms of sines and cosines leading to

$$S(\vec{q}) = \left|\sum_{j=1}^{N} \cos\left(\vec{q}\cdot\vec{r}_j\right) + i\sin\left(\vec{q}\cdot\vec{r}_j\right)\right|^2. \tag{2.39}$$

Taking the complex magnitude squared of Eq. (2.39) it becomes

$$S(\vec{q}) = \left(\sum_{j=1}^{N} \cos\left(\vec{q}\cdot\vec{r}_j\right)\right)^2 + \left(\sum_{j=1}^{N} \sin\left(\vec{q}\cdot\vec{r}_j\right)\right)^2. \tag{2.40}$$

While Eq. (2.40) is not the most convenient expression of the structure factor analytically, numerically it is ideal. Numerically a particle can be discretized onto a cubic lattice and Eq. (2.40) can easily be calculated. To numerically calculate the orientationally averaged structure

factor it is more numerically advantageous to hold the particle in specific orientation and rotate $\vec{q}$. This is done simply by stepping through magnitudes of q, for each magnitude a large number or random directions can be considered and averaged. Fig. 2.4 shows the numerical comparison of the structure factor of a sphere of radius $R = 10\mu m$, calculated using the analytical expression Eq. (2.35) and calculated numerically using Eq. (2.40). When analysis of the structure factor of a particle is needed and neither the numerical or analytical solution is readily available, approximations can be made using scaling arguments and comparison of the particle's length scales and the length scales of q^{-1} which has units of length.

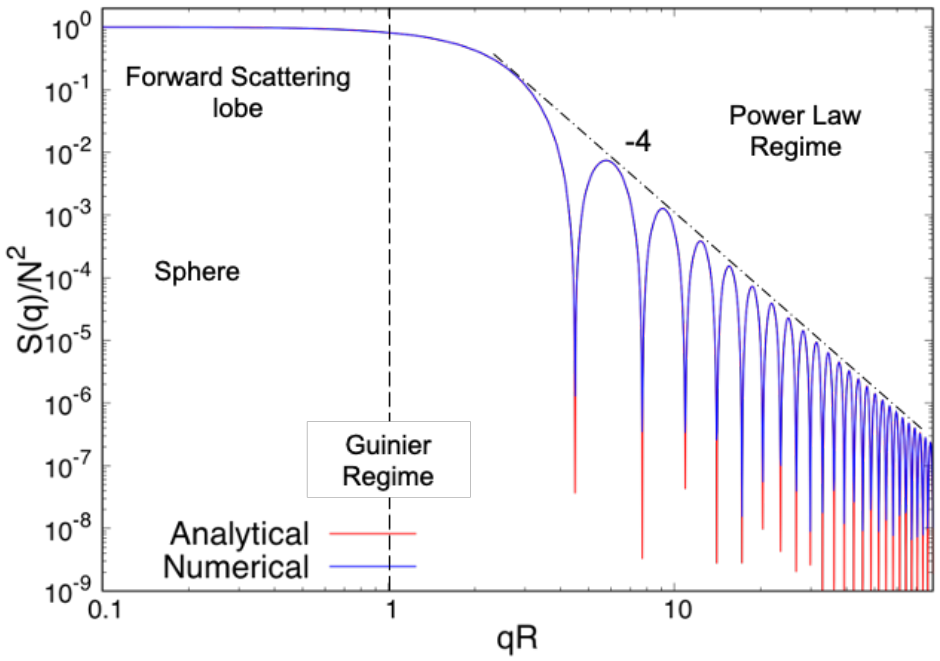

Fig. 2.4 Comparison of the analytical and numerical calculations of the structure factor of a sphere.

2.3 Scaling Approach

The scaling approach is a simple method for determining the structure factor of a single particle or a system of scatterers, first presented by Oh and Sorensen [32], and later expanded

upon by Maughan and Sorensen [33]. Much of what follows was presented in these works. There are many inherent length scales that describe a system of scatterers, whether that system be a scattering volume, aggregate of monomers, or a single particle discretized into volume elements. By comparing these inherent length scales with the length scale of q^{-1}, the structure factor can be approximated. The comparison of the length scales allows for the determination of whether the phases in the summation of Eq. (2.7) are in or out of phase, and thus whether they sum constructively or destructively. For a system of N scatterers there are two limiting cases when considering the phase given by $\vec{q} \cdot (\vec{r}_j - \vec{r}_l)$ [24,32].

1. If the N scattering elements are within q^{-1} of each other, then $q^{-1} \geq |\vec{r}_j - \vec{r}_l|$, which leads to $1 \geq q|\vec{r}_j - \vec{r}_l|$, and therefore, the dot product is $1 \geq \vec{q} \cdot (\vec{r}_j - \vec{r}_l)$. The phases of the N scattering elements will essentially be the same and the double summation in Eq. (2.7) will equal to N^2.
2. In the other extreme if the N scattering elements are separated by more than q^{-1} from each other, then $q^{-1} < |\vec{r}_j - \vec{r}_l|$, which leads to $1 < q|\vec{r}_j - \vec{r}_l|$, and therefore the dot product is $1 < \vec{q} \cdot (\vec{r}_j - \vec{r}_l)$. The phases of the N scattering elements will be random, and so the waves will sum up randomly. The inner summation of Eq. (2.7) will sum up randomly to $\sqrt{N}$, and the structure factor will go as N.
3. While not a limiting case, one more important point must be considered. Only fluctuations in the density of the scattering elements contribute to the scattering at nonzero scattering angles. If the particle is homogenous, then the scattering will come entirely from the discontinuity at the surface. On the other hand, if the particle is inhomogeneous, then both the discontinuity at the surface and fluctuations within the

particle will both contribute to the scattering. This is a consequence of the Ewald-Oseen extinction theorem [25,30].

To calculate the orientationally average structure factor for an arbitrary set of scattering elements, consider that instead of rotating the scattering volume, the q vector is rotated, similar to doing the numerical averaging. The q-vector will be rotated through all possible orientations, such that it forms spherical q-regions of radius q^{-1}. If q is small, then q^{-1} will be large, and all of the scattering elements will lie within a single q-region as shown in Fig. 2.5(a). As q begins to increase, the spherical q-region will decrease in size, and it will take multiple q-regions to encompass all of the scattering elements. If the particle is homogenous, the only fluctuations will be at the surface, and so only the q-regions on the surface as shown in Fig. 2.5(b) will contribute to the scattering. Instead, if the particle is inhomogeneous, q-regions throughout the particle will contribute.

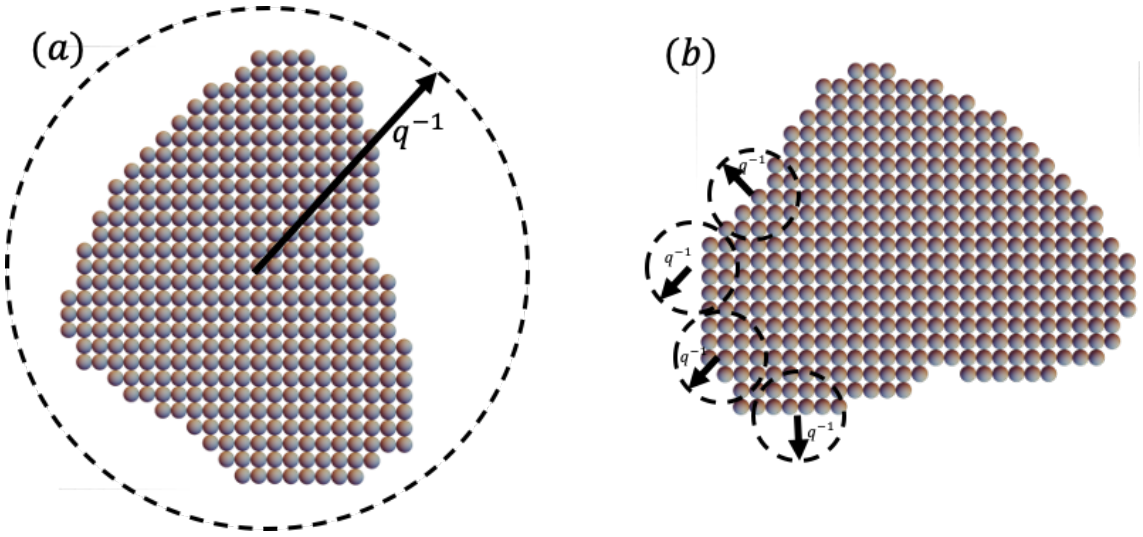

Fig. 2.5 A particle discretized into N point scatterers. (a) The entire particle fits within a single q-region. (b) Several q-regions cover the surface of the particle.

The number of scattering elements in a single q-region will be denoted by N_q. The number of q-regions that have density fluctuations within them will be referred to as n_q. All of the N_q scattering elements within a q-region will be within q^{-1} of each other, and thus, by condition 1, above they will sum up constructively and contribute a factor of N_q^2 to the structure factor. The n_q q-regions will all be separated by more than q^{-1} as a result of being spherical regions of radius q^{-1}. The n_q will thus sum up randomly and contribute a factor of n_q, and the structure factor will go as

$$S(q) = n_q N_q^2. \tag{2.41}$$

Assessing what n_q and N_q^2 are can be done by comparing the length scales of the geometric parameters of the particle and the length scales of the q-regions over a wide range of q values.

2.4 Application of the scaling approach

Consider a homogenous sphere of radius R that has been discretized onto a cubic lattice, with lattice spacing 2Δ with N lattice points, each one representing a scattering element. When q is small, q^{-1} will be large, and while $q^{-1} > R$ there will only be one q-region, so $n_q = 1$. All of the N scattering elements will be within the single q-region, and so they will all scatter relatively in phase with each and $N_q^2 = N^2$. The structure factor will then be given by

$$S(q) = N^2 \quad q^{-1} > R > \Delta\,. \tag{2.42}$$

As q increases in size, q^{-1} will decrease and the q-regions will become smaller. Once q^{-1} crosses through and becomes smaller than $> q^{-1} > \Delta$, and yet is still larger than a, there will be multiple q-regions covering the sphere. By condition 3 above only the q-regions on the surface will contribute to the structure factor. The number of scattering elements in a single q-region will be given by the product of number density, and the volume of a q-region $N_q =$

$N/V\ (4\pi/3)q^{-3}$. The number of q-regions can be approximated by the ratio of the surface area of the sphere and the cross-sectional area of a q-region $n_q = S/\pi q^{-2}$, where S is the surface area. The structure factor in this range of q will be given by

$$S(q) = \frac{16\pi N^2 S}{9V^2} q^{-4} = 4N^2(qR)^{-4}\ \ (sphere) \qquad R > q^{-1} > \Delta. \tag{2.43}$$

Guinier and Fournet arrived at similar result for the average behavior of an arbitrary homogenous three-dimensional particle given by

$$S(q) = \frac{2\pi N^2 S}{V^2} q^{-4} = \frac{9}{2} N^2(qR)^{-4}\ \ (sphere), \qquad R > q^{-1} \tag{2.44}$$

using a completely different semi-quantitative approach [8]. The ratio of Eq. (2.43) and Eq. (2.44) is ~0.88 showing just how close these distinct semi-quantitative approximations are to each other.

When q has grown large enough that the q-regions are equal to the lattice separations $q^{-1} \leq \Delta$, the q-regions will be so small they will contain only a single scatterer. In this case $N_q = 1$, and $n_q = S/\pi q^{-2}$ and the structure factor will be given

$$S(q) = Sq^2/\pi \qquad R > \Delta > q^{-1}. \tag{2.45}$$

The scattering will begin to transition and go as ~q^2 until the scattering is equal to the number of scattering elements on the surface $N_s = S/\pi\Delta^2$. The scattering will continue to go as N_s unless there are length scales smaller than Δ, which will be discussed below.

Although Eq. (2.42), Eq. (2.43), and Eq. (2.45) were arrived at by considering a sphere, the equations hold for any three-dimensional shape with aspect ratio ε~1. Shapes with very large or small aspect ratios, however, will require more consideration. In most cases it is beneficial to plot the structure factor vs the unitless qR_{veq}, where R_{veq} is the radius of a sphere with the equivalent volume. Eq. (2.42) and Eq. (2.45) are both independent of q and are thus unaffected

when plotting vs qR_{veq}. As for Eq. (2.43), all that is needed is to multiply and divide by R_{veq}^4 leading to

$$S(q) = \frac{16\pi N^2 S R_{veq}^4}{9V^2}\left(qR_{veq}\right)^{-4} \qquad R > q^{-1} > \Delta. \tag{2.46}$$

Similarly, Eq. (2.45) can be multiplied and divided by R_{veq}^2 leading to

$$S(q) = \frac{S}{\pi R_{veq}^2}\left(qR_{veq}\right)^{2} \qquad R > \Delta > q^{-1}. \tag{2.47}$$

Fig. 2.6 shows Eq. (2.42), Eq. (2.43), and Eq. (2.47) plotted vs qR_{veq} in their respective q range, compared to the numerical calculations of Eq. (2.7) for several shapes with aspect ratios of unity, including spheroids, cylinders, rectangular prisms, hexagonal prisms, droxtals [34], and Gaussian random spheres (GRS)[35] (see the appendix for more detailed shape descriptions). In Fig. 2.6 it can be seen that despite being different shapes, the scattering from all of the shapes considered exhibit the same quantitative features. As already described and seen in Fig. 2.2-Fig. 2.4, there is the forward scattering lobe that goes as N^2. When $q^{-1} = D/2$ where D is the dimension describing the particle, as an example, for a cylinder with an aspect ratio of unity $D = 2R = L$, the size of the q-regions are comparable to the size of the particle. As q increases so that q^{-1} begins to become smaller than $D/2$ and the scattering crosses through the Guinier regime, the scattering then begins its turn down into the power law regime, where the scattering follows Porod's law with a slope of -4, and the coefficient given in Eq. (2.46). When q^{-1} crosses through Δ the scattering begins to transition to go as Eq. (2.47), having a positive slope ~2, until $S(q) = S/\pi\Delta^2$, which is the number of scatterers on the surface. After reaching the number of scatterers on the surface, there is nothing that will change as q increases, because there are no other length scales in the particle.

Fig. 2.6 also shows the effects of the orientational averaging, and how surface roughness and lack of symmetry effects the rippling of the scattering. The scattering for the spheroids with an aspect ratio of unity or a sphere shows large regular rippling, while the GRS will show almost no ripples. The shapes with more symmetry produce more ripples in the orientationally averaged scattering, this is because distinct orientations produce ripples at different values of qR_{veq}. The more symmetry there is, the larger number of orientations with ripples at the same qR_{veq} values. The less symmetry, and the maximums and minimums of the rippling are distributed over a larger range of qR_{veq} values, and thus the average washes out more of the rippling.

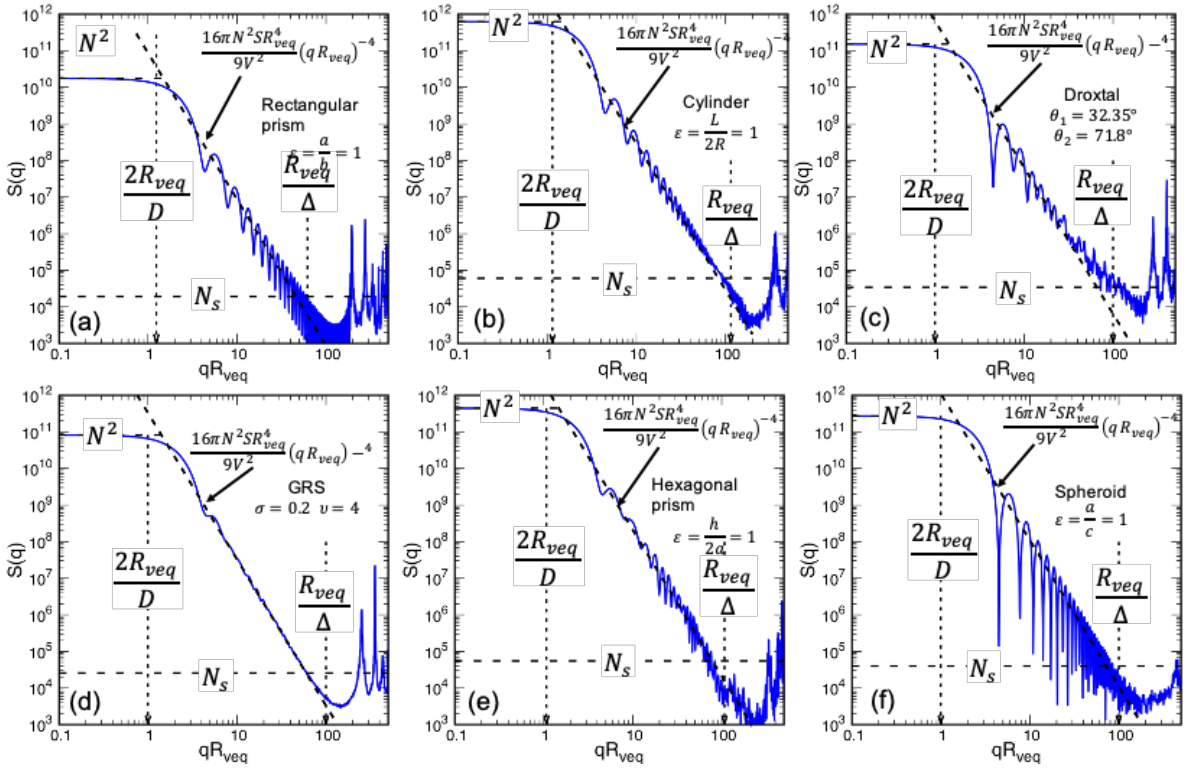

Fig. 2.6 The structure factor for a rectangular prism (a), cylinder (b), droxtal (c), GRS (d), hexagonal prism (e), spheroid (f) all with ε = 1. The solid blue curve shows the Fourier transform numerically calculated using Eq. (2.40). The dashed lines are computed using the scaling approach.

As will be shown below, the aspect ratio plays a significant role in the scattering in the RDG limit, in fact much of the scattering can be described solely in terms of the aspect ratio as

shown in Fig. 2.7 [33]. If the aspect ratio is much greater than or smaller than unity, there will be two Guinier regimes and two power law regimes. The first Guinier regime will occur when the size of the q-regions become comparable to the largest dimension describing the shape $q^{-1} = D_1/2$. The forward scattering lobe will transition into the first power law regime after the first Guinier regime, then when the size of the q-regions becomes comparable to the smaller dimension describing the shape $q^{-1} = D_2/2$, there will be a second Guinier regime. The second Guinier regime marks the transition into the second power law regime. Just as when the aspect ratio was close to unity calculating the behavior of the scattering in the first power law regimes can be done by determining what N_q and n_q are.

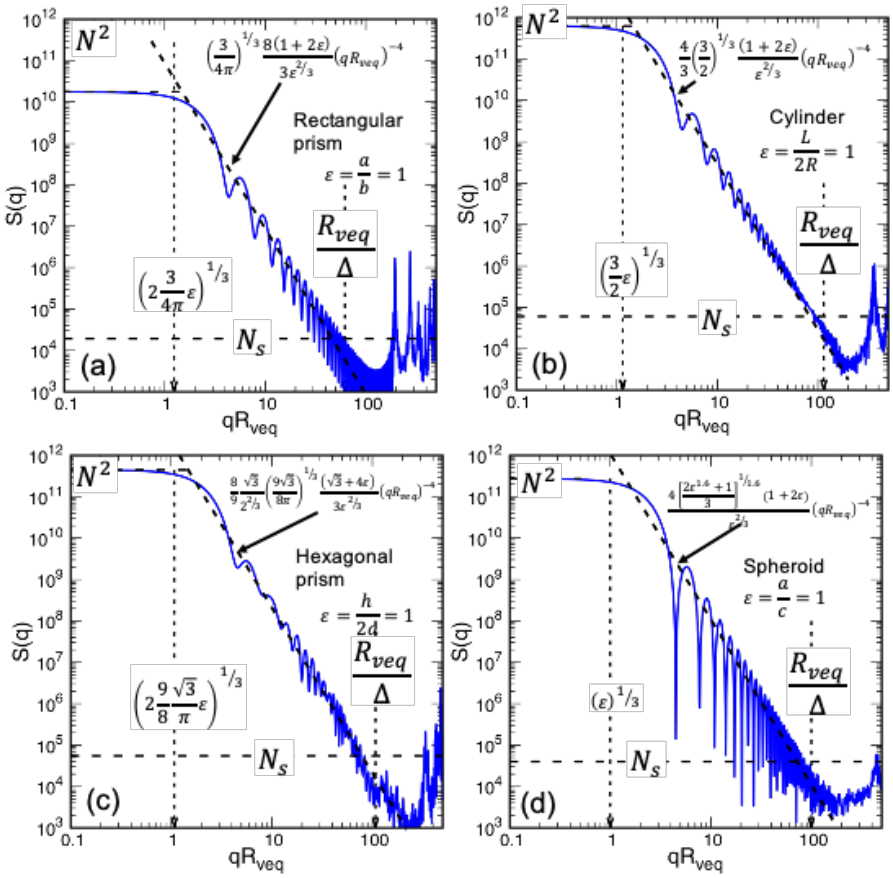

Fig. 2.7 The structure factor for a rectangular prism (a), cylinder (b), hexagonal prism (c), spheroid (d) all with ε = 1. The solid blue curve shows the Fourier transform numerically calculated using Eq (2.40). The dashed lines are computed using the scaling approach. The coefficients to the scattering in the power law regime, and the Guinier regime cross over points are described in terms of the aspect ratio ε.

2.5 Large aspect ratios

Consider a long cylinder with a large aspect ratio $\varepsilon = L/2R \gg 1$, as shown in Fig. 2.8. In this case, the largest dimension would be the length $D_1 = L$, and the smaller dimension would be diameter $D_2 = 2R$. When q is very small a single q-region will be larger than the entire particle $q^{-1} > D_1/2 > D_2/2$ and just as in Eq. (2.42) the scattering will go as N^2. As q increases, the q-region becomes smaller and will cross through the largest dimension, D_1, and $q^{-1} = D_1/2$ i.e. $L/2$ for a long cylinder, at the first Guinier regime.

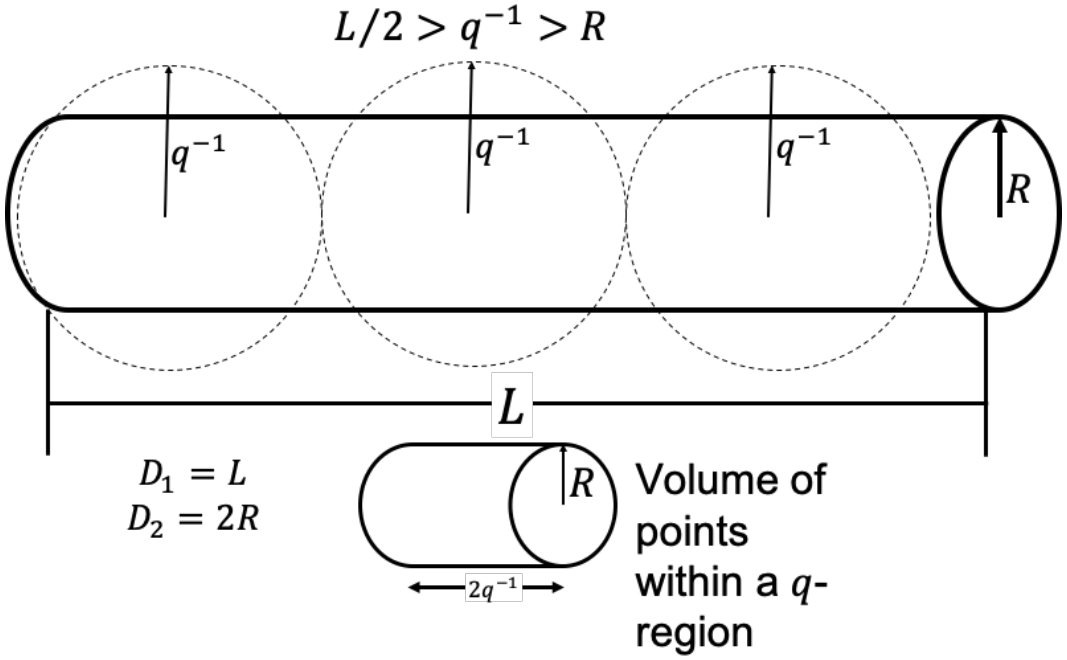

Fig. 2.8 A cylinder with $\varepsilon = L/2R = 10$. A finite number of q-regions fit within L, while all the q-regions overlap in R. The volume of a q-region can be approximated as smaller cylinders, as drawn below.

As the q-regions become smaller than D_1, and yet remain larger than D_2 so that $D_1/2 > q^{-1} > D_2/2$ i.e. $(L/2 > q^{-1} > R)$ for a long cylinder, the scattering will be in the first power law regime. In the first power law regime the q-regions will overlap the particle in the D_2 direction i.e. $2R$ for a long cylinder and as shown in Fig. 2.8 there will be a finite number of q-

regions that can fit within D_1 direction i.e. L for a long cylinder. The number of q-regions will be determined by the finite number that can fit within the D_1 direction i.e. L for a long cylinder, and will be given by D_1 divided by the length of a q-region leading to [33]

$$n_q = \frac{D_1}{2q^{-1}} \quad \varepsilon \gg 1 \quad \frac{D_1}{2} > q^{-1} > \frac{D_2}{2}. \tag{2.48}$$

The number of points in a q-region will be determined by D_2 i.e. $2R$ for a cylinder. The volume of a q-region in this regime can be estimated to be that of a cylinder with length $2q^{-1}$ and cross section C_{D_2} i.e. πR^2 for a long cylinder as shown in Fig. 2.8. The number density of points within the particle and the volume of a q-region will determine the number of points within a q-region

$$N_q = \frac{N}{V} C_{D_2} 2q^{-1} \quad \varepsilon \gg 1 \qquad \frac{D_1}{2} > q^{-1} > \frac{D_2}{2}. \tag{2.49}$$

Putting together Eq. (2.41), Eq. (2.48) and Eq. (2.49) the structure factor in the first power law region will be given by

$$S(q) = 2\frac{N^2}{V^2} C_{D_2}^2 D_1 q^{-1}\,. \tag{2.50}$$

Again, if plotting vs the unitless qR_{veq} Eq. (2.50) can be multiplied and divided by R_{veq} leading to

$$S(q) = 2\frac{N^2}{V^2} C_{D_2}^2 D_1 R_{veq} \left(qR_{veq}\right)^{-1} \qquad \frac{D_1}{2} > q^{-1} > \frac{D_2}{2}. \tag{2.51}$$

It can be seen in Eq. (2.51) that the scattering follows a power law of -1 in the first power law regime. As q continues to increase through the first power law regime, the size of the q-regions will become comparable to D_2, and the scattering will cross through the second Guinier regime and enter the second power law regime. In the second power law regime the q-regions will be smaller than either dimension and only the surface will contribute to the scattering and

the scattering will be given by Eq. (2.44). Finally, once the q-regions become comparable to the size of the individual scatterer, the scattering will be given by Eq. (2.45).

Fig. 2.9 shows Eq. (2.42), Eq. (2.50), Eq. (2.46), and Eq. (2.47) plotted vs qR_{veq} in their respective q range, compared to the numerical calculations of Eq. (2.7) for several shapes with aspect ratios of $\varepsilon = 10$, including spheroids, cylinders, rectangular prisms, and hexagonal prisms. As in Fig. 2.6 the scattering by all of the particles follows the same quantitative features despite being different shapes. There is the forward scattering lobe that goes as N^2, followed by the first Guinier regime when $q^{-1} = D_1/2$.

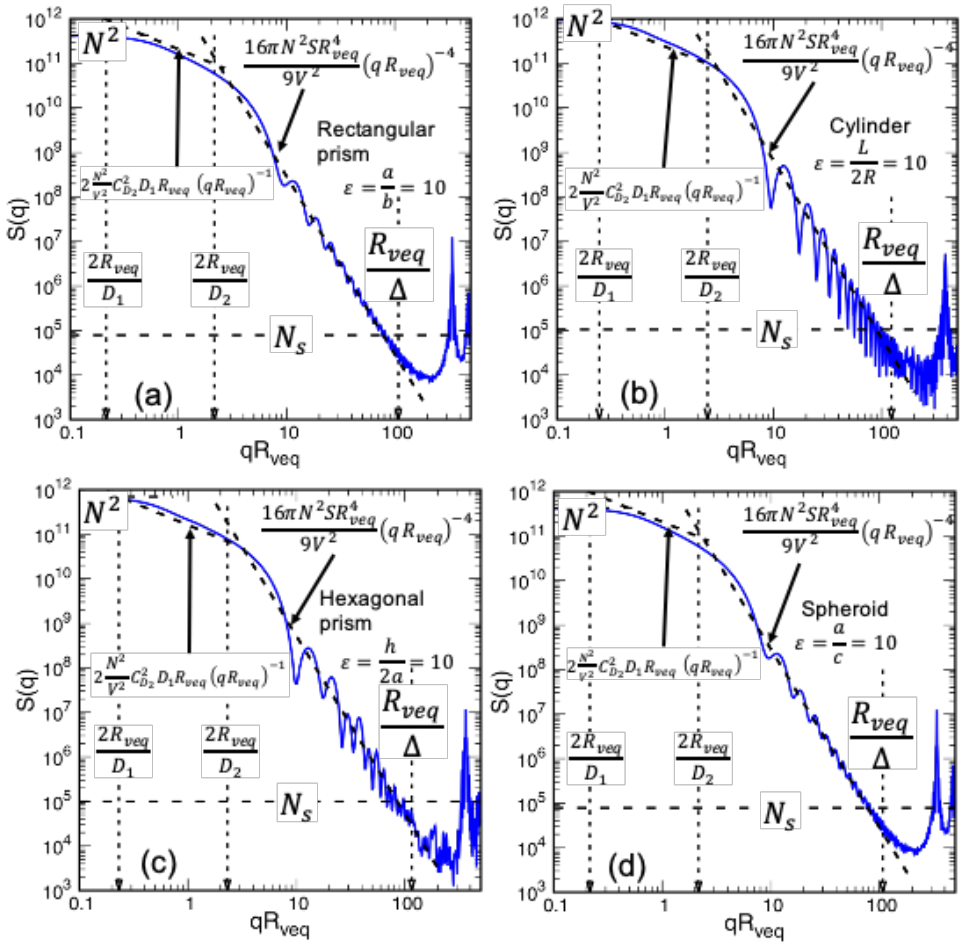

Fig. 2.9 The structure factor for a rectangular prism (a), cylinder (b), hexagonal prism (c), spheroid (d) all with $\varepsilon = 10$. The solid blue curve shows the Fourier transform numerically calculated using Eq. (2.40). The dashed lines are computed using the scaling approach.

At the first Guinier regime, the scattering transitions into the first power law regime that follows Eq. (2.51), with a power law of -1. The second Guinier regime is seen when $q^{-1} = D_2/2$, and is followed by the second power law regime that follows Eq. (2.46), with a slope of -4. Finally, when q^{-1} crosses through Δ, the scattering begins to transition to go as $S/\pi\Delta^2$. In Fig. 2.10 the scattering quantiles in Fig. 2.9 have been expressed in terms of the aspect ratio ε [33].

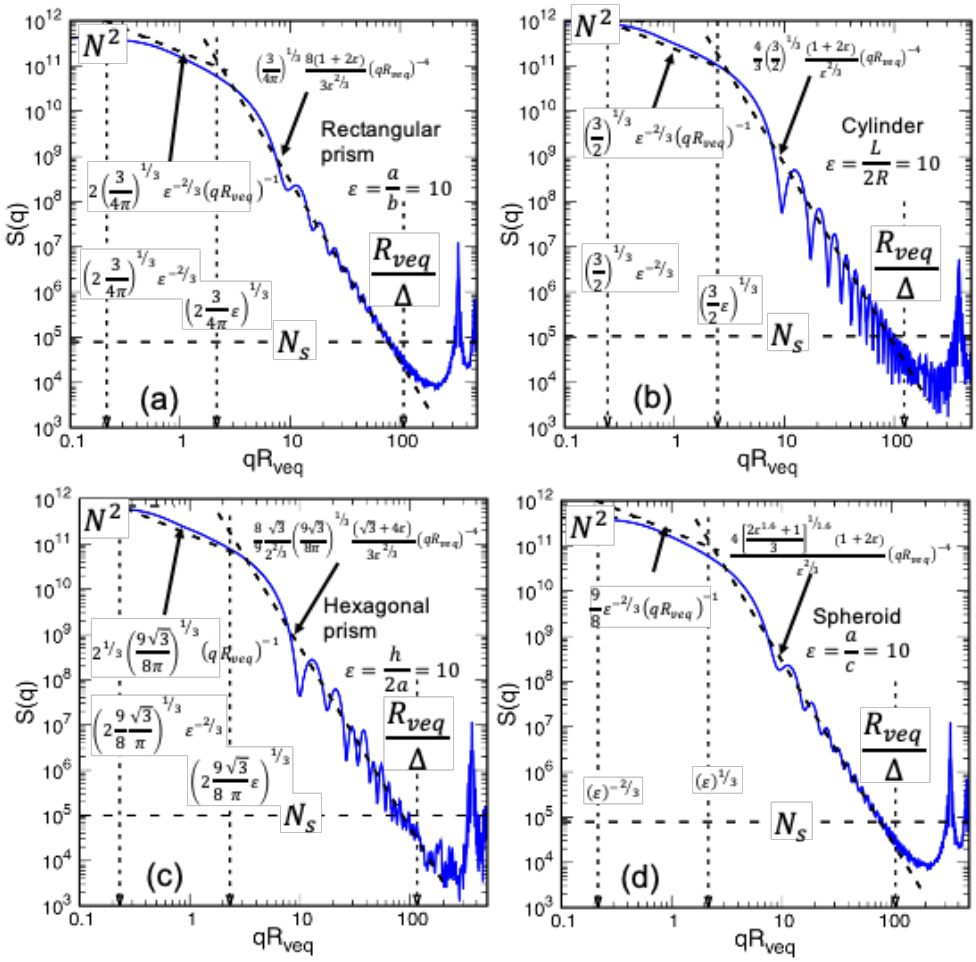

Fig. 2.10 The structure factor for a rectangular prism (a), cylinder (b), hexagonal prism (c), spheroid (d) all with $\varepsilon = 10$. The solid blue curve shows the Fourier transform numerically calculated using Eq. (2.40). The dashed lines are computed using the scaling approach. The coefficients to the scattering in the power law regime, and the Guinier regime cross over points are described in terms of the aspect ratio ε.

2.6 Small aspect ratios

Going to the other limit consider a thin disk with a small aspect ratio $\varepsilon = L/2R \ll 1$, as shown in Fig. 2.11. In this case the largest dimension would be the length $D_1 = 2R$ and the smaller dimension would be diameter $D_2 = L$. When q is very small a single q-region will be larger than the entire particle $q^{-1} > D_1/2 > D_2/2$ and just as in Eq. (2.42) the scattering will go as N^2. As q increases the q-region becomes smaller and will cross through the largest dimension D_1, and $q^{-1} = D_1/2$ i.e. R for a thin disk, at the first Guinier regime.

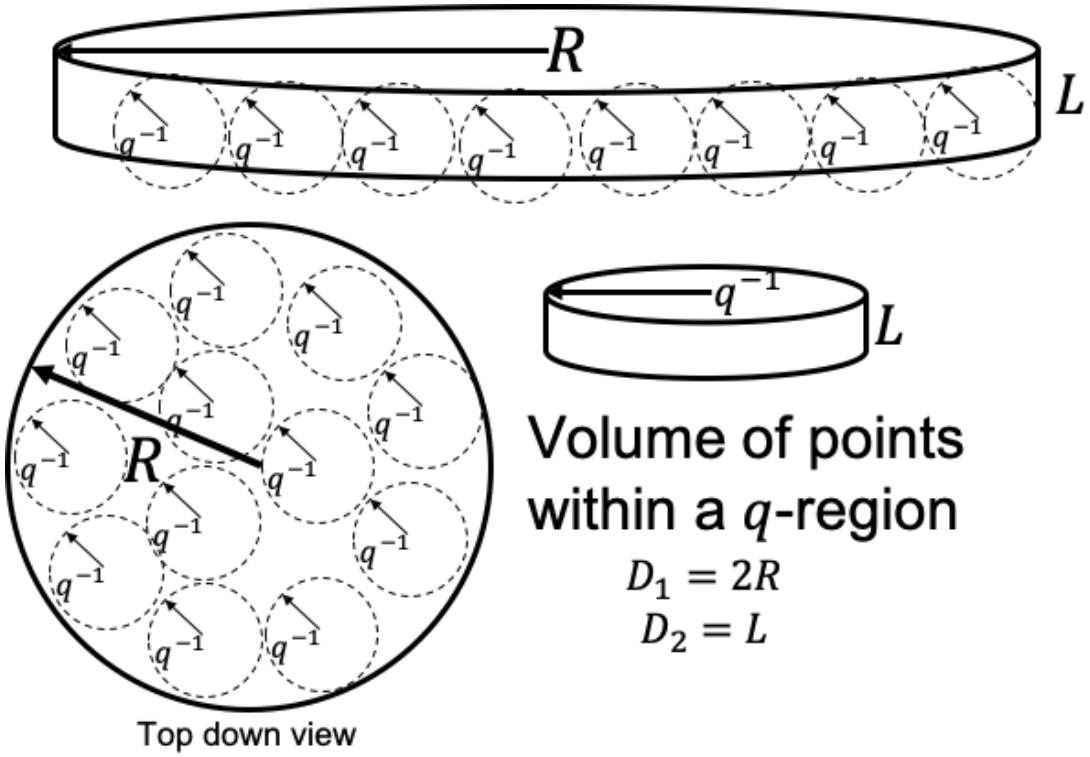

Fig. 2.11 A circular disk with $\varepsilon = L/2R = 0.1$. A finite number of q-regions fit within R, while all the q-regions overlap in L. The volume of a q-region can be approximated as smaller disks.

As the q-regions become smaller than D_1, and yet remain larger than D_2 so that $D_1/2 > q^{-1} > D_2/2$ i.e. $(R > q^{-1} > L/2)$ for a thin disk, the scattering will be in the first power law regime. In the first power law regime the q-regions will overlap the particle in the D_2 direction

i.e. L for a long cylinder and as shown in Fig. 2.11 there will be a finite number of q-regions that can fit within D_1 direction i.e. $2R$ for a thin disk . The number of q-regions will be determined by the finite number that can fit within the D_1 direction i.e. $2R$ for a thin disk, and will be given by the ratio of the cross section of the disk C_{D_1} i.e. πR^2 for a thin disk, and the cross section of a q-region [33]

$$n_q = \frac{C_{D_1}}{\pi q^{-2}} \quad \varepsilon \ll 1 \quad \frac{D_1}{2} > q^{-1} > \frac{D_2}{2}. \tag{2.52}$$

The number of points in a q-region will be determined by D_2 i.e. L for a cylinder. The volume of a q-region in this regime can be estimated to be that of a cylinder with length D_2 i.e. L for a thin disk, and cross section πq^{-2}, as shown in Fig. 2.11. The product of the number density of points within the particle and the volume of a q-region will determine the number of points within a q-region. Putting together Eq. (2.41), Eq. (2.52) and Eq. (2.53) the structure factor in the first power law region will be given by

$$S(q) = \pi \frac{N^2}{V^2} C_{D_1} D_2^2 q^{-2} \quad \varepsilon \ll 1 \qquad \frac{D_1}{2} > q^{-1} > \frac{D_2}{2}. \tag{2.53}$$

Again, if plotting vs the unitless qR_{veq} Eq. (2.53) can be multiplied and divided by R_{veq}^2 leading to

$$S(q) = \pi \frac{N^2}{V^2} C_{D_1} D_2^2 R_{veq}^2 \left(qR_{veq}\right)^{-2} \quad \varepsilon \ll 1 \qquad \frac{D_1}{2} > q^{-1} > \frac{D_2}{2}. \tag{2.54}$$

It can be seen in Eq. (2.54) that the scattering follows a power law of -2 in the first power law regime. As q continues to increase through the first power law regime, the size of the q-regions will become comparable to D_2 i.e. L for a thin disk, and the scattering will cross through the second Guinier regime and enter the second power law regime. In the second power law regime the q-regions will be smaller than either dimension, only the surface will contribute to the

scattering, and the scattering will be given by Eq. (2.45). Finally, once the q-regions become comparable to the size of the individual scatterer the scattering will be given by Eq. (2.46).

Fig. 2.12 shows Eq. (2.42), Eq. (2.54), Eq. (2.46), and Eq. (2.47) plotted vs qR_{veq} in their respective q range, compared to the numerical calculations of Eq. (2.7) for several shapes with aspect ratios of $\varepsilon = 0.1$, including spheroids, cylinders, rectangular prisms, and hexagonal prisms. As in Fig. 2.6 and Fig. 2.9, the scattering by all of the particles follow the same quantitative features despite being different shapes.

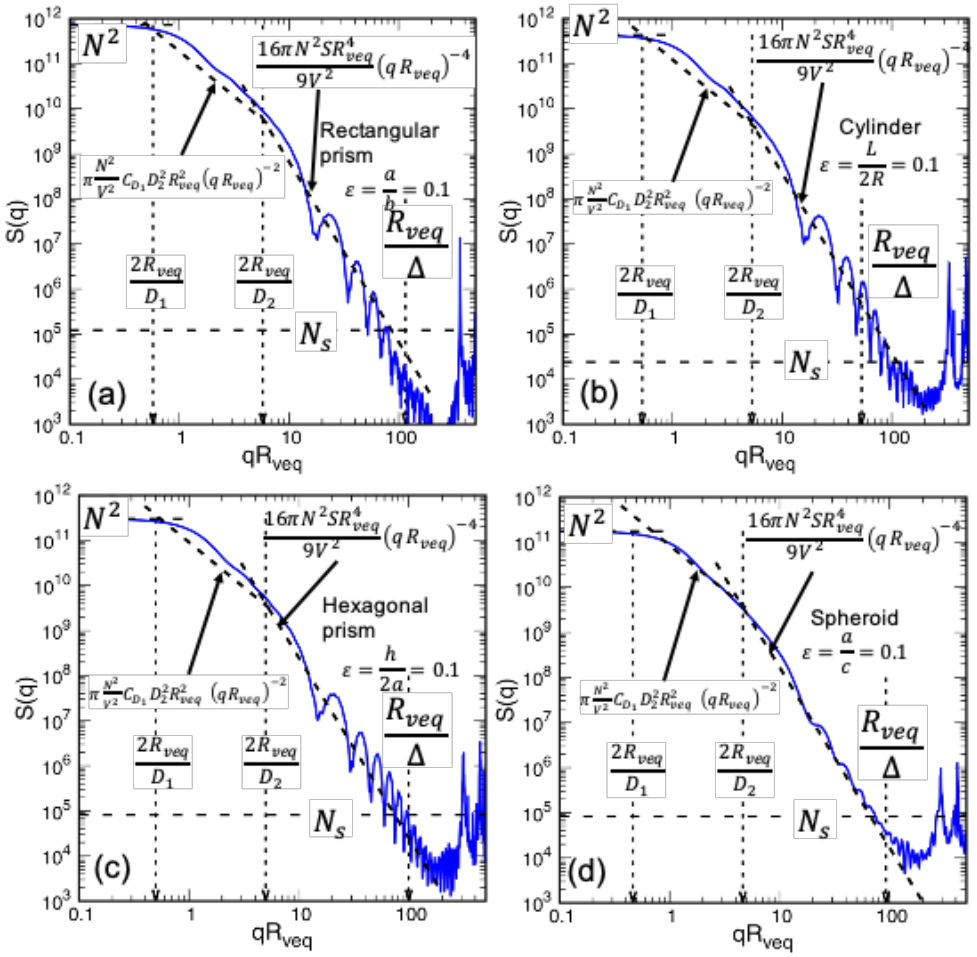

Fig. 2.12 The structure factor for a rectangular prism (a), cylinder (b), hexagonal prism (c), spheroid (d) all with $\varepsilon = 0.1$. The solid blue curve shows the Fourier transform numerically calculated using Eq. (2.40). The dashed lines are computed using the scaling approach.

There is the forward scattering lobe that goes as N^2, followed by the first Guinier regime when $q^{-1} = D_1/2$. At the first Guinier regime, the scattering transitions into the first power law regime that follows Eq. (2.54), with a power law of -2. The second Guinier regime is seen when $q^{-1} = D_2/2$, and is followed by the second power law regime that follows Eq. (2.46), with a slope of -4. Finally, when q^{-1} crosses through Δ, the scattering begins to transition to go as Eq. (2.47) $S/\pi\Delta^2$. In Fig. 2.13 the scattering quantities in Fig. 2.12 have been expressed in terms of the aspect ratio ε [33].

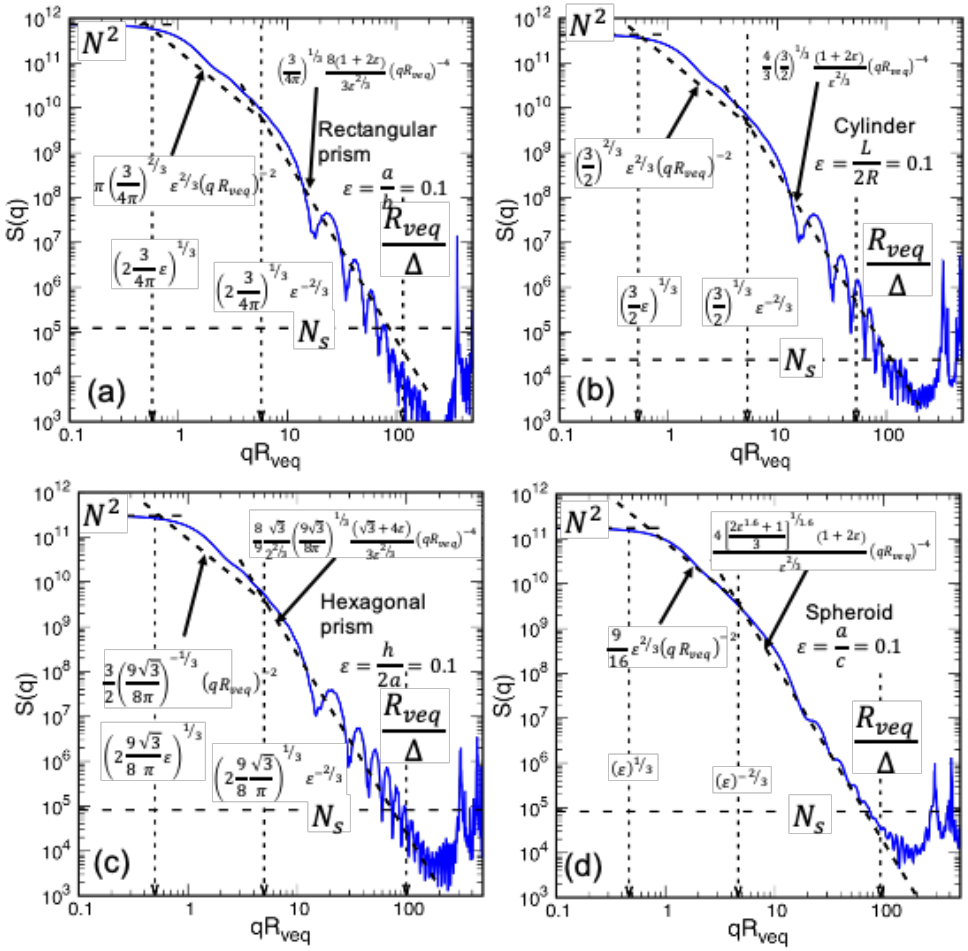

Fig. 2.13 The structure factor for a rectangular prism (a), cylinder (b), hexagonal prism (c), spheroid (d) all with $\varepsilon = 0.1$. The solid blue curve shows the Fourier transform numerically calculated using Eq. (2.40). The dashed lines are computed using the scaling approach. The coefficients to the scattering in the power law regime, and the Guinier regime cross over points are described in terms of the aspect ratio ε.

2.7 Volume fluctuations

Considering once again a sphere of radius R, only this time after discretizing the sphere into N scattering elements, each of the N scattering elements has been randomly perturbed by

$$\delta x = r\gamma\Delta, \tag{2.55}$$

$$\delta y = r\gamma\Delta, \tag{2.56}$$

$$\delta z = r\gamma\Delta, \tag{2.57}$$

where r is a random number between -1 and 1 as was previously done for the two-dimensional case in [32]. The average displacement of the scattering elements is given by $\gamma\Delta$, where γ is a positive number. Fig. 2.14 shows a two-dimensional representation of a sphere i.e. (a circle of radius R), on the left side the scattering elements are unperturbed, while on the right they have been randomly perturbed by Eq. (2.55) and Eq. (2.56) with a $\gamma = 0.5$. In the bottom center of Fig. 2.14 an enlarged red square shows three different lengths $\gamma,\ \Delta,$ and $\gamma\Delta$.

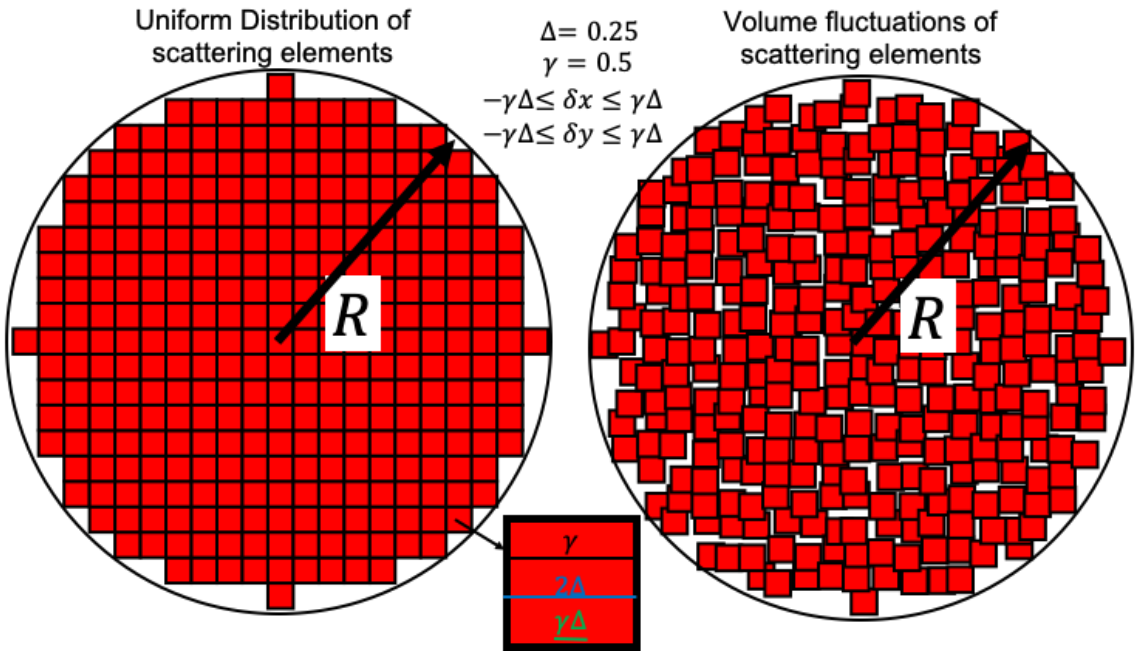

Fig. 2.14 On the left the uniform distribution of scattering elements, on the right the scattering elements have been randomly perturbed.

On the right of Fig. 2.14 it can be seen that due to the random perturbation of several scattering elements structures have formed within the circle. These structures can be seen as gaps between the scattering elements of various sizes but all ~2γ, thus when $q^{-1} = \gamma$ the scattering will cross a length scale. The lattice spacing itself is equal to 2Δ, and so when $q^{-1} = \Delta$ another length scale will be crossed. Finally, the smallest of the length scales will be crossed when $q^{-1} = \gamma\Delta/2$. The size of γ, Δ, and γΔ relative to each other is dependent of the values of γ and Δ, for example if $\Delta = 0.25\mu m$, and $\gamma = 0.05$, then $\Delta > \gamma > \gamma\Delta/2$. On the other hand, if $\gamma = 5$ then $\gamma > \gamma\Delta/2 > \Delta$ and the scattering will reflect the differences in relative size as will be demonstrated.

When q is small and thus q^{-1} is large, the fluctuations within the sphere will not affect the scattering as the length scales of the scattering are larger than that of the fluctuations. Eq. (2.42) and Eq. (2.43) will still apply in their respective q ranges. When q becomes large enough that q^{-1} becomes comparable to the size of γ, Δ, or $\gamma\Delta/2$, then scattering becomes effected by the fluctuations. Once $q^{-1} = \gamma\Delta/2$ is reached whether it is smaller or larger than γ, or Δ the entire volume of the sphere will have fluctuations in density that are of the same order as the scattering. All of the N scattering element will now contribute to the scattering, instead of just the elements on the surface. N scattering elements summing up with random phases will lead to the scattering going as N.

To investigate how the relative sizes of γ, Δ, or $\gamma\Delta/2$ can affect the scattering, Fig. 2.15 shows the structure factor numerically calculated for $\gamma = 0, 0.05$, with $\Delta = 0.25\mu m$. When $\gamma = 0.05$, $\gamma\Delta/2 = 0.00625\ \mu m$ and so $\Delta > \gamma > \gamma\Delta/2$. Fig. 2.15 has been plotted vs Δ , so when $q^{-1} = \Delta$, $q\Delta = 1$, when $q^{-1} = \gamma$, $q\Delta = \Delta/\gamma$, and $q^{-1} = \gamma\Delta/2$, $q\Delta = 2/\gamma$. It can be seen in Fig. 2.15 that when $\gamma = 0$ the scattering follows the same behavior as seen in Fig. 2.6(f), there is

a forward scattering lobe that goes as Eq. (2.42), followed by a power law regime that follows Eq. (2.46) with the replacement of R_{veq} with Δ as the structure factor is being plotted vs $q\Delta$.

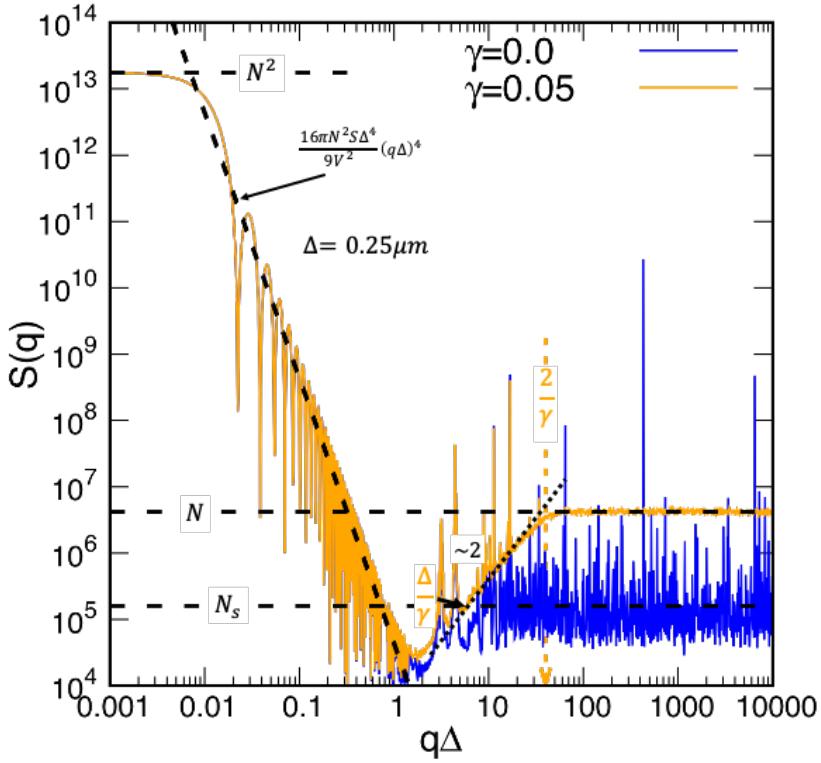

Fig. 2.15 Structure factor of a sphere with uniformly distributed volume elements (blue), and with the volume elements randomly perturbed, with $\gamma = 0.05$ (orange).

Once $q^{-1} = \Delta$, the scattering transitions and starts to increase going as $\sim q^2$ until the scattering is equal to N_s, which it continues to follow as there are not any other length scales to cross. When $\gamma = 0.05$, however, the scattering goes at N_s until $q^{-1} = \gamma$, $q\Delta = \Delta/\gamma$, here the larger structures created by the perturbations become comparable to the scattering length scale and the scattering begins to increase toward N. The increase toward N again goes as $\sim q^2$. This can be understood by considering that there are now regions that have internal surface area, and so the total surface area S_t will be the sum of the outer surface area S and the internal surface area. The number of

scatterers in a q-region will be unity, and number of q-regions n_q would be the ratio of S_t and the cross section of a q-region given by πq^{-2}, leading to the structure factor going as

$$S(q) = N^2 n_q = \frac{S_t}{\pi q^{-2}} = \frac{S_t q^2}{\pi}. \tag{2.58}$$

It can be seen in Eq. (2.57) the scattering will still go as ~q^2. Finally, when $q^{-1} = \gamma\Delta/2$, $q\Delta = 2/\gamma$ the scattering has reached N, and continues to follow N.

Fig. 2.16 shows the case when $\gamma = 0, 0.5$. The behavior for $\gamma = 0$ has already been discussed, as for $\gamma = 0.5$, with $\Delta = 0.25\mu m$ then $\gamma\Delta/2 = 0.0625\ \mu m$ and so now $\gamma > \Delta > \gamma\Delta/2$. Fig. 2.16 has been plotted vs Δ , so when $q^{-1} = \gamma$, $q\Delta = \Delta/\gamma$, when $q^{-1} = \Delta$, $q\Delta = 1$, and when $q^{-1} = \gamma\Delta/2$, $q\Delta = 2/\gamma$. In this situation $q^{-1} = \gamma$ is reached first and the scattering length scales become comparable to the larger structure created by the perturbations.

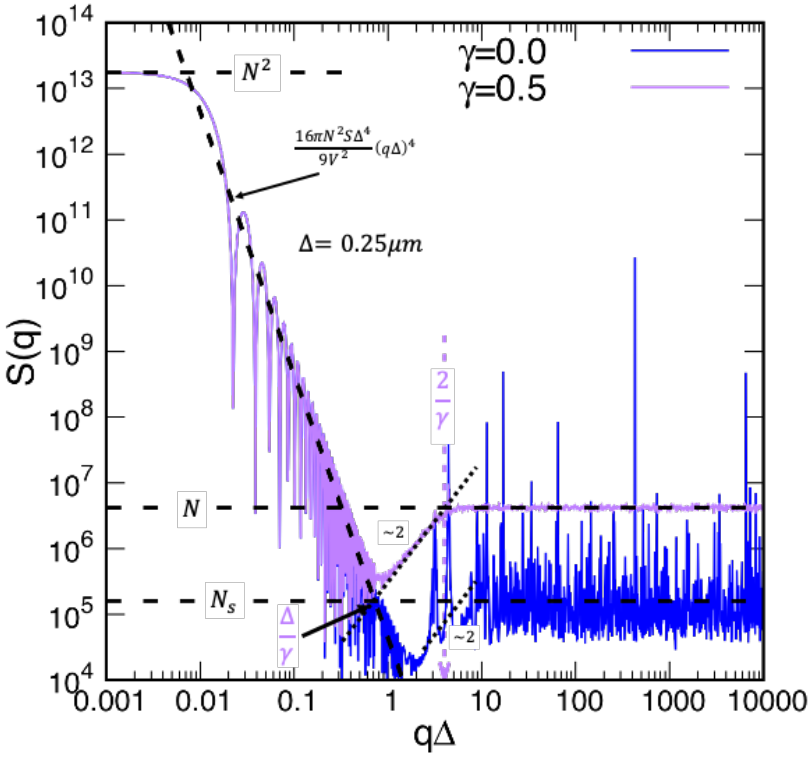

Fig. 2.16 Structure factor of a sphere with uniformly distributed volume elements (blue), and with the volume elements randomly perturbed, with $\gamma = 0.5$ (purple).

When $q^{-1} = \Delta$, the scattering is already going as ~q^2, and the internal fluctuations are adding to the surface area, so the scattering is unaffected and continues to go as ~q^2. Finally, as before when $q^{-1} = \gamma\Delta/2$, $q\Delta = 2/\gamma$ the scattering has reached N, and continues to follow N. In Fig. 2.17 $\gamma = 0, 5$ and so when $q\Delta = \Delta/\gamma = 0.05$ the scattering is still in the power law regime, and so once $q^{-1} = \gamma\Delta/2$, $q\Delta = 2/\gamma$ the scattering transitions straight into going as N, and continues to follow N.

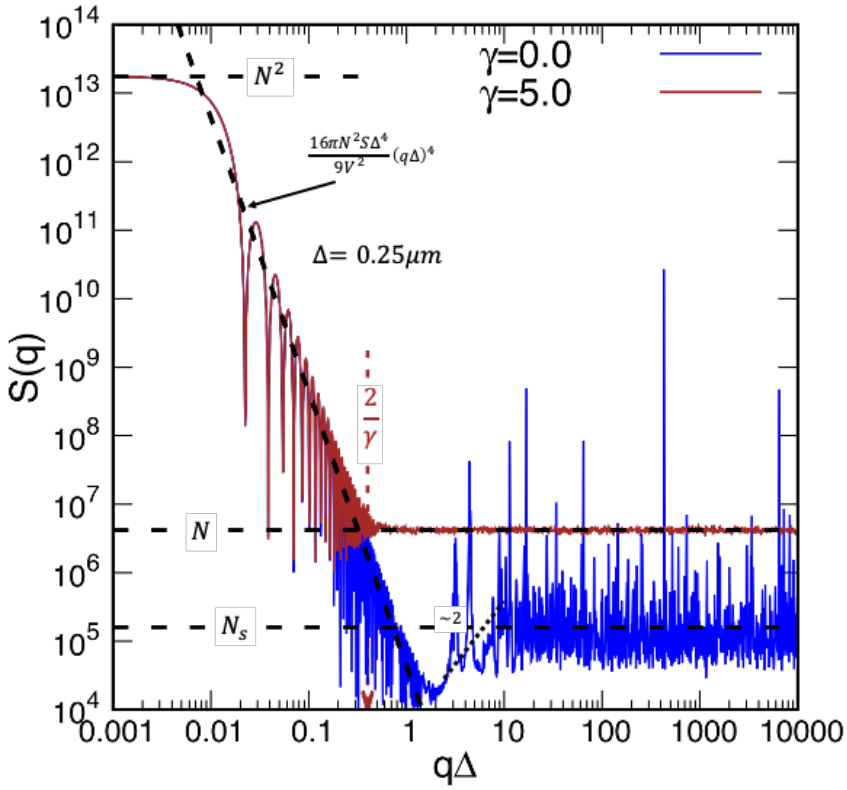

Fig. 2.17 Structure factor of a sphere with uniformly distributed volume elements (blue), and with the volume elements randomly perturbed, with $\gamma = 5$ (brown).

Fig. 2.18 shows a combined graph with $\gamma = 0, 0.0005, 0.005, 0.05, 0.5, 5$ to demonstrate how the scattering responds to the changing relative length scales.

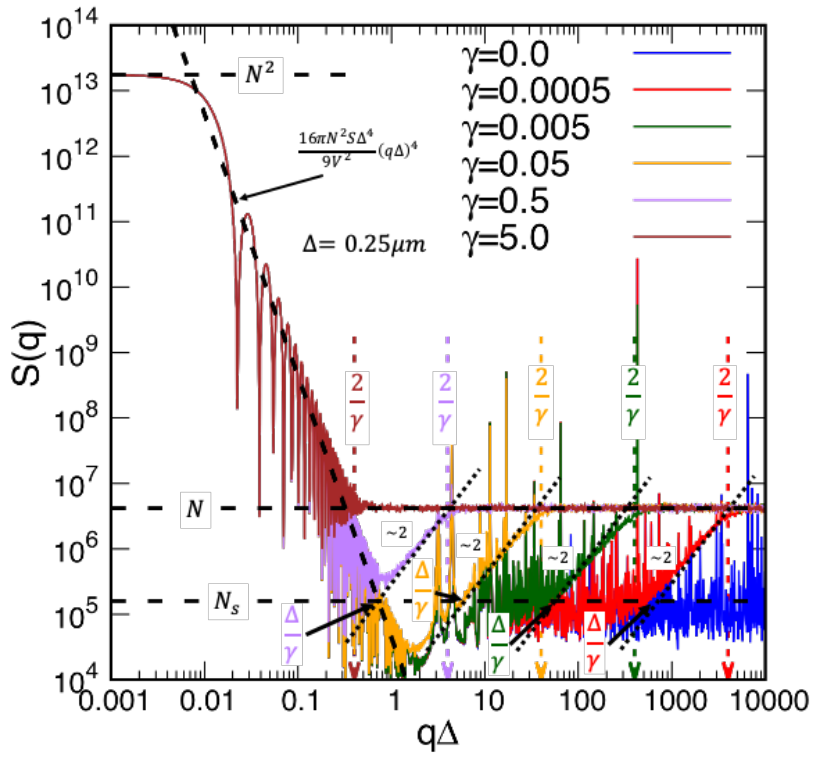

Fig. 2.18 Structure factor of a sphere with uniformly distributed volume elements (blue), and with the volume elements randomly perturbed.

2.8 Multiple spheres

Instead of a single particle let us now consider how the scaling approach can be applied to a scattering volume consisting of multiple particles. Consider taking an imaginary three-dimensional volume of radius R_V, and filling it in randomly with spherical monomers of radius a. The spherical monomers will all be discretized onto a cubic lattice with lattice spacing 2Δ just as before. N will be denoted as the total number of scattering elements in scattering volume, N_m as the number of scattering elements in a monomer, and N_v as the total number of monomers in the scattering volume, such that $N = N_V N_m$. Going back to Eq. (2.7) the scattering element positions can be described relative to the centers of the individual monomers as $\vec{r}_i = \vec{r}_v + \vec{r}_m$ leading to [36]

$$S(q) = \sum_v^{N_V} \sum_w^{N_V} \sum_m^{N_m} \sum_n^{N_m} e^{i\vec{q}\cdot((\vec{r}_v+\vec{r}_m)-(\vec{r}_w+\vec{r}_n))}$$
$$= \sum_v^{N_V} \sum_m^{N_V} e^{i\vec{q}\cdot(\vec{r}_v-\vec{r}_w)} \sum_m^{N_m} \sum_n^{N_m} e^{i\vec{q}\cdot(\vec{r}_m-\vec{r}_n)}, \quad (2.59)$$

which can be expressed as

$$S(q) = S_V(q)S_m(q), \quad (2.60)$$

where $S_V(q)$ is the structure factor of the scattering volume treating the monomers as points, located at their centers, and $S_m(q)$ is the structure factor of a single monomer.

Fig. 2.19 shows the calculation of four structure factors for a spherical volume of $R_V = 1\mu m$ that has been randomly filled with spherical monomers. The first S_m is that of a single monomer of radius $a = 0.02\mu m$. The next S_V is the numerical structure factor of the scattering volume, which is calculated by treating the monomers as points located at the center of the monomers.

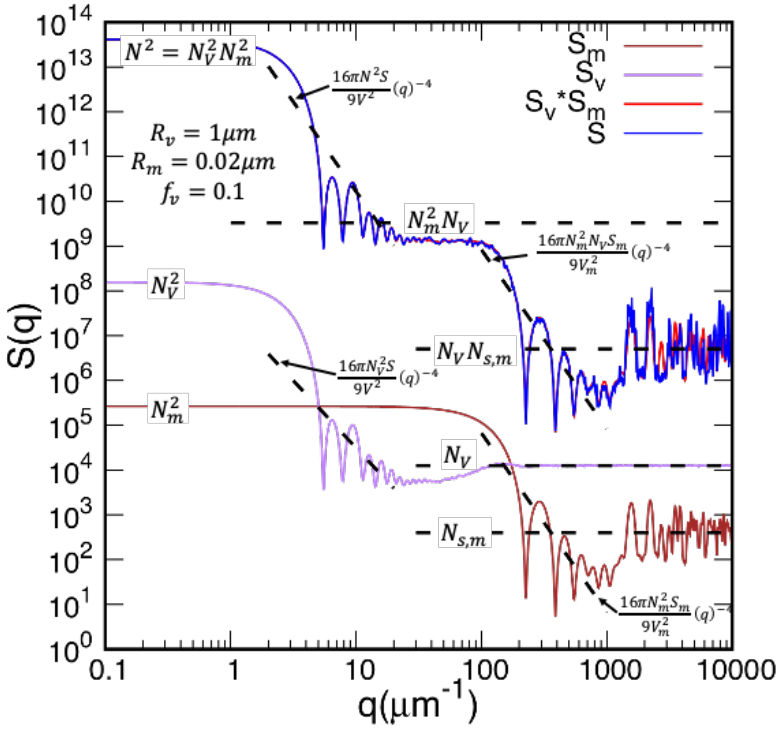

Fig. 2.19 The structure factor of a spherical volume randomly filled with monomers. The total structure factor is equal to the product of the volume and monomer structure factors. The blue curve for S almost entirely covers the red for $S_v S_m$.

Eq. (2.60) is also plotted along with the structure factor calculated using the entire system S. The first note of Fig. 2.19 is that the product of S_m and S_V does match well with S, only a small amount of the red curve for the product S_m and S_V can be seen, giving validity to Eq. (2.60).

In Fig. 2.19 it can be seen that the S_m behaves just as the previous uniform spheres that have been studied see Fig. 2.6(f), it has a forward scattering lobe that goes as N_m^2. There is a Guinier regime when $q^{-1} = a$ that marks the transition from the forward scattering lobe to a power law regime. In the power law regime, the scattering follows Eq. (2.44) with the number of scattering elements, surface area and volume being that of the monomer, N_m, S_m, and V_m respectively. Once $q^{-1} = \Delta$, the scattering turns up and increases until each reaches the number of scattering elements on the surface of a monomer $N_{s,m}$.

S_V in Fig. 2.19 follows the same behavior as a uniform sphere, a forward scattering lobe that goes as the number of monomers squared N_V^2. When q^{-1} is equal to the radius of the scattering volume R_v there is a Guinier regime, which is followed by a power law regime in which the scattering follows Eq. (2.44) with the number of scattering elements, surface area and volume being that of the scattering volume, N_V, S, and V, respectively. The scattering follows the power law until $q{\sim}20\mu m^{-1}$ or $q^{-1}{\sim}0.05\mu m$, at which time it levels off and then begins increasing toward the number of monomers N_V. To understand this behavior, refer to spheres with internal fluctuations. There were two length scales introduced with internal fluctuations. One of the length scales comes from larger structures due to the random shifting of several volume elements away from a uniform system, which is reached first, and the second is the average random displacement away from a uniform system. When the length scale of the larger

structures is reached, the scattering begins to increase as there are more scatterers contributing to the scattering, until N_V is reached which is the most that it could possibly contribute.

When the product of S_m and S_V is considered as shown in Fig. 2.19 some of the individual behaviors remain while some are lost. This puts an emphasis on how looking at the individual structure factors leads to insights that may not be readily apparent from the total structure factor. The total structure factor has two scattering lobes, two Guinier regimes and two power law regimes. There is a scattering lobe that goes as the square of the total number of scattering elements N^2, then at the first Guinier regimes when $q^{-1} = R_V$. The first Guinier regime is followed by a power law regime that follows Eq. (2.44), and then transitions into a second scattering lobe for the monomer. Just before the monomer Guinier regime, S_V begins to increase at around $q = 40(\mu m^{-1})$, but at the same time S_m starts to decrease and so the product remains the same as can be seen in S. The monomer scattering lobe lies below $N_m^2 N_V$ because just as S_m reaches its Guinier regime, S_V has just reached N_V, so there is never the exact product of N_m^2 and N_V. This again demonstrates the insight that can be gained by looking at the individual structure factors along with the total. The monomer Guinier regime leads into the monomer power law regime which goes as Eq. (2.44) with the monomer parameters N_m, S_m, and V_m, times the total number of monomers in the volume N_V. Finally, the scattering at large q goes as the number of scattering elements on the surface of a monomer times the number of monomers in the volume $N_V N_{s,m}$.

2.9 Fractals Aggregates

So far, the scaling approach has been applied to three-dimensional single particles with more regular shape descriptions. Taking a more arbitrary approach to the description of the shape

can be taken by using a general mass, and surface scaling dimension D_m and D_s, respectively. As always when the q-region is larger than any dimension describing the particle, the structure factor will go as N^2. In the power law regime for an arbitrary case, the number of scatterers in a q-region is found by taking the product of the density of scatterers and the volume of a q-region just as before but using arbitrary expression for the volumes. As the volumes are being treated as arbitrary, the number of scatterers in a q-region will be expressed as a proportionality rather than an equality and is given by [32]

$$N_q \propto N\left(\frac{q^{-1}}{D/2}\right)^{D_m} \tag{2.61}$$

where D is the dimension describing the system of scatters, i.e. $2R$ for a sphere discretized onto a cubic lattice. Similarly, the number of q-regions that are on the surface can be expressed as a ratio of the total generalized surface area of the arbitrary system and the generalized cross section of a q-region. As with N_q because we are dealing with an arbitrary system the number of q-regions will be expressed as a proportionality and is given by

$$n_q \propto \left(\frac{D/2}{q^{-1}}\right)^{D_s}. \tag{2.62}$$

Putting together Eq. (2.41), Eq. (2.61) and Eq. (2.62) the structure factor can be expressed as being proportional to

$$S(q) \propto N^2(q\,D/2)^{-2D_m+D_s} \qquad {}^{D}/_{2} > q^{-1} > \Delta. \tag{2.63}$$

The proportionality in Eq. (2.63) can be expressed as an equality by inserting a constant, so that the structure factor is equal to

$$S(q) = CN^2(q\,D/2)^{-2D_m+D_s} \qquad {}^{D}/_{2} > q^{-1} > \Delta \tag{2.64}$$

where C is a unitless constant that is dependent on the specifics of the scattering particle(s). As an example, consider a sphere of radius R, in this case $D/2 = R$, $D_m = 3, D_s = 2$ and the coefficient $C = 4$, and the structure factor in the power law regime will go as

$$S(q) = 4N^2(qR)^{-4} \qquad R > q^{-1} > \Delta. \tag{2.65}$$

Eq. (2.64) can be also expressed in terms of the size of a single scatterer Δ, and the number of scatterers that are on the surface by defining [32]

$$N = k_m \left({}^{D}/_{2}/_{\Delta}\right)^{D_m}, \tag{2.66}$$

$$N_s = k_s \left({}^{D}/_{2}/_{\Delta}\right)^{D_s}, \tag{2.67}$$

where N_s is the number of scatterers on the surface and k_m and k_s are constants of the order unity, that depend on how the lattice is used to discretize the particle(s). Combing Eq. (2.64), Eq. (2.66), and Eq. (2.67) leads to

$$S(q) = Ck_0N_s(q\Delta)^{-2D_m+D_s}, \qquad {}^{D}/_{2} > q^{-1} > \Delta \tag{2.68}$$

where $k_0 = k_m^2/k_s$. When $q^{-1} \leq \Delta$ as before the q-regions will only encompass a single scattering element and only the scattering elements where there is non-uniformity in the density will contribute to the scattering. For a homogenous particle this means on the surface, elements scatter, and the scattering will go as N_s.

A fractal is a geometric system that is scale invariant. Some common occurrences of scale invariance in nature are fern fronds, of which a single frond is formed of smaller duplicates of the larger frond. This attribute of the smaller parts being identical to the whole is also referred to as being self-similar. Another excellent example is presented by Richardson [37], and illuminated further by Mandelbrot [38] in which they use the measuring of coast lines on increasing smaller scales to describe fractals. A fractal aggregate is an aggregation of monomers that has a self-similar structure. Ideal fractals are considered to be made up of identical spherical

monomers, or radius a, in point contact with each other. Fractal aggregates can be described by a relatively simple yet important relationship [24]

$$N_A = k_o \left({}^{R_g}/_{a} \right)^{D_f}, \tag{2.69}$$

where N_A is the number of monomers in the aggregate, R_g is the root mean square radius, referred to as the radius of gyration, $D_f = D_m = D_s$ is the fractal dimension, k_o is the scaling prefactor and is the same k_o in Eq. (2.68). In nature, fractal aggregates can be found in aerosols and colloids, and form by clusters hitting and sticking together. They commonly yield diffusion limited cluster-cluster aggregation (DLCA) [39]. We will use values of $k_o = 1.35$ and $D_f = 1.8$ in this work, which is around the values found for DLCA simulations in [40–43].

Just as was done with a spherical volume filled with monomers, a fractal aggregate can be treated as a product of two systems, see Fig. 2.20. In the first system for the aggregate itself, all of the monomers are treated as points. The second system is a monomer that has been discretized onto a cubic lattice. The total structure factor for the fractal aggregate and its monomers will then be given by

$$S(q) = S_A(q) S_m(q). \tag{2.70}$$

The structure factor of the spherical monomers will exhibit the exact same behavior as the monomers presented in the previous section on multiple spheres as seen in Fig. 2.20.

The fractal aggregate structure factor will have a forward scattering lobe as all particles do, that will go as the number of monomers in the aggregate squared N_A^2. There will then be a Guinier regime when the characteristic length scale of the aggregate $D/2 = R_g$ is comparable to q^{-1}. The scattering will transition into the power law regime, in which the scattering will follow Eq. (2.64) using the number of monomers in the aggregate $N \rightarrow N_A$, the dimension describing

the aggregate is $D/2 = R_g$, and the mass and surface scaling dimensions are given by the fractal dimension $-2D_m + D_s = -2D_f + D_f = -D_f$ leading to

$$S_A(q) = CN_A^2(qR_g)^{-D_f}. \tag{2.71}$$

The coefficient in Eq. (2.61) has been found empirically to be approximately unity [24], this can also be seen in Fig. 2.20. After the power law regime, the scattering transitions, and goes as N_A (the number of monomers that make up the aggregate).

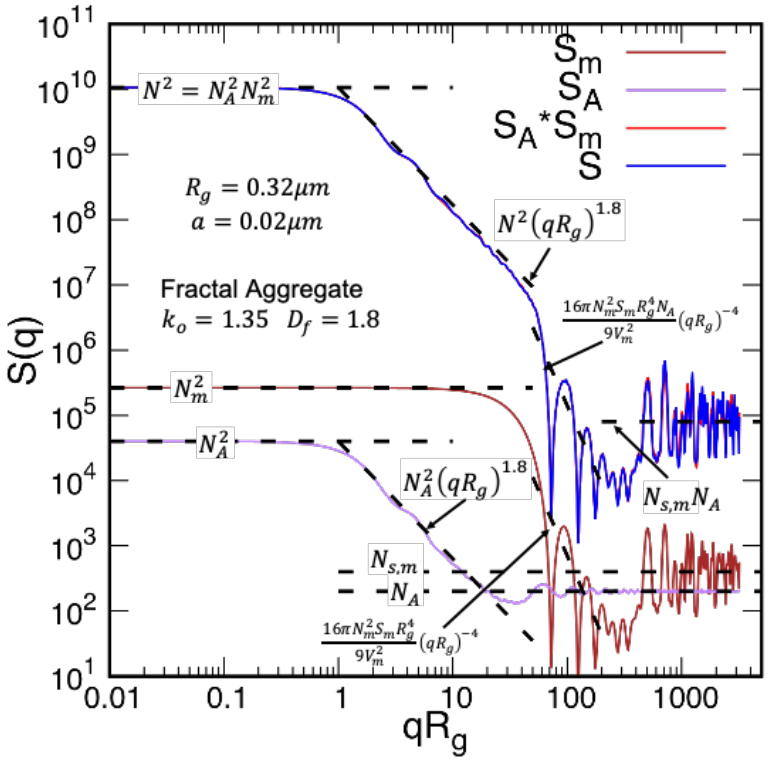

Fig. 2.20 The structure factor of a fractal aggregate. The total structure factor is equal to the product of the aggregate and monomer structure factors. The blue curve for S almost entirely covers the red for $S_A S_m$.

When looking at the total structure factor in Fig. 2.20, it can be seen that the forward scattering lobe goes as the total number of scattering elements N^2, and the first power law regime goes as $N^2(qR_g)^{-D_f}$. Following the first power law regime, there is a transition at the monomer Guinier regime into a second power law regime for the monomer. In the second power

law regime the scattering goes as Eq. (2.46) times $N_{A,}$ with the number of scattering elements, volume, and surface area being that of a monomer $N_{m,}$ V_m, and S_m and the equivalent radius R_g. After the second power law regime the scattering transitions up to go as the total number of scattering elements on the surface of all the monomers $N_{s,m}$, N_A.

The concept of looking at the total structure factor as a product of the structure factor of its parts is not limited to the two examples described here. Fractal aggregates can come together to form super-aggregates through cluster-cluster aggregation [44]. In this case, there would be the overall scattering volume, the super-aggregates, the individual aggregates, and the monomers each with a distinct structure factor. The product of the four individual parts would be the total structure factor of the system [36]. It is also important to note that in many scattering experiments only a specific range of the structure factor is retrieved. This is due to the fact that the range is limited by the wavelength of the scattering experiment. As an example, a scattering experiment that uses a wavelength of $\lambda = 532nm$, that can collect the data from $0.1° < \theta < 170°$, would be limited to a q range of $0.02\mu m^{-1} <$q$< 23.5\mu m^{-1}$. If instead x-ray scattering is used with a wavelength of $\lambda = 10nm$, the experiment would have a q range of $1.1\mu m^{-1} \lesssim q \lesssim 1251\mu m^{-1}$.

Chapter 3 - Q-space Analysis of the Light Scattered by Spheres

As the scattering begins to leave the 3d RDG diffraction limit, or in terms of the internal coupling parameter when $\rho' \gtrsim 1$, there is not a single analytical or numerical method that can be used for all shapes, sizes, and refractive indices. The natural starting point for shapes with $\rho' \gtrsim 1$ is spheres. The symmetry of spheres allows for an exact analytical solution for the light scattering and absorption by spheres of arbitrary size and refractive index [4]. Solutions for the scattering and absorption were developed independently in various forms by Debye, Lorenz, and Mie, but the most commonly used nomenclature and citation is Mie theory, and [2], respectively. In our modern era of computers, the analytical Mie theory can readily be calculated computationally in a relatively quick amount of time even for large spheres with extreme refractive indexes. The relatively quick calculation of scattering and absorption by spheres not only allows the understanding of how spheres scatter light but also provides a first order approximation to what may be expected from the scattering by other shapes.

3.1 Mie theory

The mathematical formulation of Mie theory has been covered by many sources, [3,4,45] are but three examples. The derivation of the Mie equations involves the expansion of a plane electromagnetic wave in vector spherical harmonics, and the matching of spherical boundary conditions. In this work the main result of the derivation will be presented as well as the calculation of the scattering quantities. The main quantities derived in Mie theory are the complex scattering coefficients [4,46]

$$a_n = \frac{m\psi_n(mkR)\psi_n'(kR) - \psi_n(kR)\psi_n'(mkR)}{m\psi_n(mkR)\xi_n'(kR) - \xi_n(xkR)\psi_n'(mkR)} \tag{3.1}$$

$$b_n = \frac{\psi_n(mkR)\psi_n'(kR) - m\psi_n(kR)\psi_n'(mkR)}{\psi_n(mkR)\xi_n'(kR) - m\xi_n(kR)\psi_n'(mkR)} \tag{3.2}$$

where ψ_n and ξ_n are the Riccati-Bessel functions [3,4]. ψ_n and ξ_n are related to the spherical Bessel function of the first and second kind, $j_n(x)$ and $y_n(x)$ respectively by [21]

$$\psi_n(x) = xj_n(x), \tag{3.3}$$

$$\xi_n(x) = xj_n(x) + ixy_n(x). \tag{3.4}$$

The complex scattering coefficients a_n and b_n are coefficients in four different infinite sums. These sums are used for calculating the two, scattering angle dependent, non-zero complex elements of the scattering amplitude matrix [4] and the total extinction and scattering cross sections, $S_1(\theta)$, $S_2(\theta)$, C_{ext}, and C_{sca} respectively. The amplitude matrix elements are given by

$$S_1(\theta) = \sum_n \frac{2n+1}{n(n+1)}\big(a_n\pi_n(\theta) + b_n\tau_n(\theta)\big), \tag{3.5}$$

$$S_2(\theta) = \sum_n \frac{2n+1}{n(n+1)}\big(a_n\tau_n(\theta) + b_n\pi_n(\theta)\big). \tag{3.6}$$

$\tau_n(\theta)$ and $\pi_n(\theta)$ in Eq. (3.5) and Eq. (3.6) are angle dependent functions defined as [3,4]

$$\pi_n(\theta) = \frac{P_n^1(\cos(\theta))}{\sin(\theta)}, \tag{3.7}$$

$$\tau_n(\theta) = \frac{dP_n^1(\cos(\theta))}{d\theta}, \tag{3.8}$$

where $P_n^m(\cos(\theta))$ is the associated Legendre polynomials [21]. The total extinction and scattering cross-sections are given by

$$C_{ext} = \frac{2\pi}{k^2}\sum_n (2n+1)\mathrm{Re}(a_n + b_n), \tag{3.9}$$

$$C_{sca} = \frac{2\pi}{k^2}\sum_n (2n+1)(|a_n|^2 + |b_n|^2). \tag{3.10}$$

Once the total extinction and scattering cross-sections are known, the total absorption cross-section can be found by taking the difference

$$C_{abs} = C_{ext} - C_{sca}. \tag{3.11}$$

The amplitude matrix is a 2x2 complex matrix that is very similar to the Mueller matrix except the amplitude matrix relates the incident and scattered fields instead of intensities. All 16 of the Mueller matrix elements can be related to the amplitude matrix elements, but as a sphere only has four independent Mueller matrix elements only the four following relationships are needed [4],

$$S_{11} = \frac{1}{2}(|S_2|^2 + |S_1|^2), \tag{3.12}$$

$$S_{12} = \frac{1}{2}(|S_2|^2 - |S_1|^2), \tag{3.13}$$

$$S_{33} = \frac{1}{2}(S_2^* S_1 + S_2 S_1^*), \tag{3.14}$$

$$S_{34} = \frac{i}{2}(S_1 S_2^* - S_2 S_2^*). \tag{3.15}$$

Once Muller matrix elements are known the differential cross sections can be calculated as outlined in chapter 1.

3.2 The Internal Coupling Parameter of a Sphere

So far reference has been made to the internal coupling parameter ρ' without any specifics given. The origin of ρ' is fairly straight forward and is found by considering the two limits of Mie scattering as was first presented in[11]. First consider a weakly refractive sphere of arbitrary size, the scattering by the sphere will be in the 3d RDG diffraction limit. In the forward direction the differential scattering cross section in the 3d RDG diffraction limit is given by Eq. (2.17) with $\theta = 0$

$$\frac{dC_{sca,RDG,3D}}{d\Omega}(0) = k^4R^6\left|\frac{m^2-1}{m^2+2}\right|^2. \tag{3.16}$$

Eq. (3.16) is valid for any polarization in the exact forward direction. Now, consider a strongly refractive sphere of arbitrary size with a sufficiently large refractive index (how large is sufficiently large will be addressed in the next section). In this limit the sphere will behave like a two-dimensional obstacle, and scattering from the sphere at $\theta = 0$ will be in the 2d RDG limit [11,47]. The differential scattering cross section when $\theta = 0$, in the 2d RDG limit can be found by combining Eq. (2.38) and Eq. (1.40)

$$\frac{dC_{sca,RDG,2D}}{d\Omega}(0) = \frac{k^2R^4}{4}. \tag{3.17}$$

The internal coupling parameter is then given by the square root of the ratio of Eq. (3.16) and Eq. (3.17) [11]

$$\rho' = \sqrt{k^4R^6\left|\frac{m^2-1}{m^2+2}\right|^2 \Big/ \frac{k^2R^4}{4}} = 2kR\left|\frac{m^2-1}{m^2+2}\right|. \tag{3.18}$$

Imagine dividing a particle into small scattering elements just as was done in chapter 2. When $\rho' < 1$ all of the scattering elements can be treated as being independent and only interacting with the incident field, and the formulations presented in chapter 2 apply. Even if the size parameter kR of the sphere becomes large, if m remains small enough that $\rho' < 1$, the scattering remains in the 3d RDG limit. Fig. 3.1 shows the Rayleigh normalized perpendicularly polarized Mie scattering of spheres with the same $\rho' = 0.1$ but different size parameters kR and indexes of refraction m plotted vs the scattering angle θ in Fig. 3.1(a) and vs qR in Fig. 3.1(b). In Fig. 3.1(a) all that can be discerned from the plot is that there is a series of ripples, the spheres

with larger size parameters have more ripples and the ripple spacing goes as $\delta\theta = \pi/kR = \lambda/2R$ [48]. Examining Fig. 3.1(a) would not intuitively lead to the idea that there is a similarity between the curves at all.

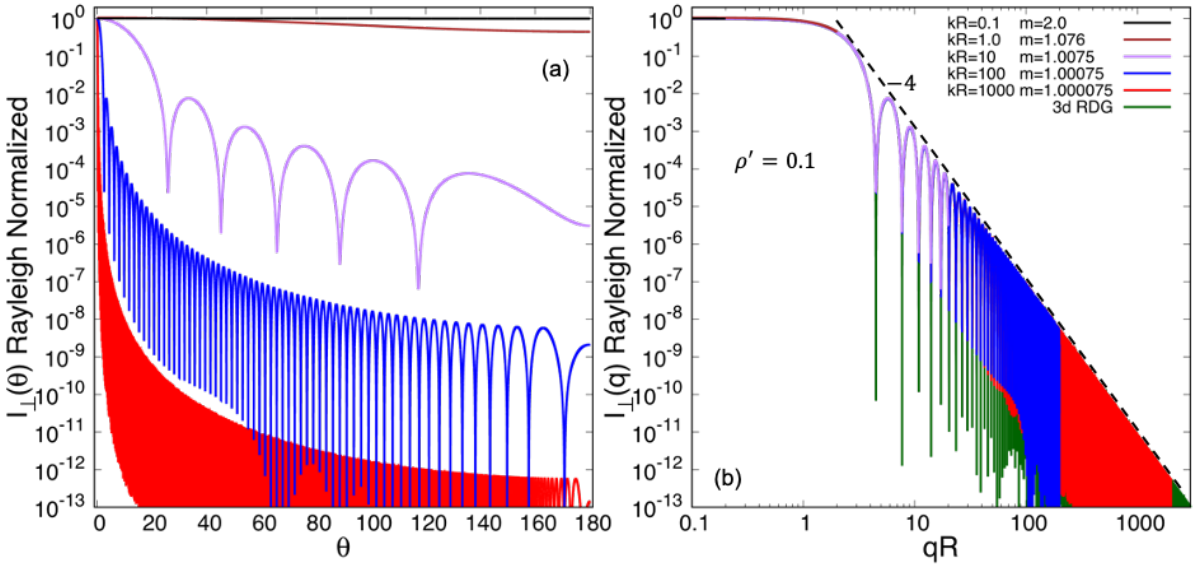

Fig. 3.1 Mie scattering for spheres with a $\rho' = 0.1$, plotted vs the scattering angle θ (a) , vs qR (b).

In Fig. 3.1(b), however, it can be seen that despite having different sizes all of the scattering from the spheres follows the Rayleigh normalized 3d RDG scattering given by combining Eq. (2.16) and Eq. (2.35), with the only distinction being the maximum $qR = 2kR$. The ripple spacing in qR of $\delta(qR) = \pi$ is the same for all of the curves despite being different sizes and having different indexes of refraction m [48]. When $kR = 0.1$ there is only the forward scattering lobe going as unity, in which the scattering is constant with qR, this is Rayleigh scattering. As the size parameters increase the scattering begins to follow 3d RDG scattering and exhibits the expected Guinier regime when $qR = 1$, followed by a power law regime which follows Porod's law with a slope of -4. Also seen Fig. 3.1(a) or Fig. 3.1(b) is that the Rayleigh normalization when $\rho' < 1$ causes the forward scattering to go as unity, which is as expected from a Rayleigh scatterer.

As ρ' approaches unity, the scattering elements begin to interact, and each scattering element begins to see not only the incident field but the scattered field from all of the other scattering elements, hence the name internal coupling parameter. As ρ' increases the scattering in the forward directions begin to develop away from the 3d RDG scattering toward the 2d RDG scattering (circular aperture diffraction). Fig. 3.2 shows the Mie scattering from two spheres, one with a $\rho' = 0.1$ and the other with a $\rho' = 1000$, representing the two limits of scattering. In Fig. 3.2 it can be seen that the curve with $\rho' = 0.1$ follows the 3d RDG as described above, when $\rho' = 1000$ the scattering has developed in the 2d RDG limit for the forward scattering, given by inserting Eq. (2.29) into Eq. (2.38) and taking the Rayleigh normalized perpendicular scattering. The $\rho' = 1000$ curve in Fig. 3.2 has a forward scattering lobe but instead of being at unity the Rayleigh normalized forward scattering goes as $1/\rho'^2$, which is to be expected as the ratio of Eq. (3.17) divided by Eq. (3.16) gives $1/\rho'^2$.

The forward scattering lobe leads into the Guinier regime at $qR = 1$, which is followed by a power law regime that has a power law of -3 up to about $qR \sim \rho'/10$, which is the 2d RDG component of the forward scattering. To see this in more detail, begin with the asymptotic behavior of the Bessel function given by [21,47]

$$J_1(x) \approx \sqrt{\frac{2}{\pi x}} \cos\left[x - \left(\frac{3\pi}{4}\right)\right] \tag{3.19}$$

combining Eq. (3.19), Eq. (2.29), and Eq. (2.38) and Rayleigh normalizing leads to

$$I_{\perp,RN}(q) \approx \frac{8}{\pi\rho'^2}(qR)^{-3} \quad 1 \lesssim qR \lesssim \frac{\rho'}{10}, \tag{3.20}$$

where the subscript RN denotes Rayleigh normalized. After the 2d RDG behavior in the forward directions, refraction effects as opposed to diffraction effects begin to dominate the scattering. The Mie scattering develops into a refraction "hump" that reaches over and meets up with the 3d

RDG scattering when qR is roughly equal to ρ'. The refraction "hump" turns down and begins to transition into other refractive effects such as the "generalized" rainbows and glories that collectively appear as a spike at large qR and are referred to as the enhanced backscattering [48,49]. The term "generalized" is used as rainbows are associated with water and the refractive index of $n = 1.33$ yet the refractive effect that leads to them is not limited to an index of $n = 1.33$.

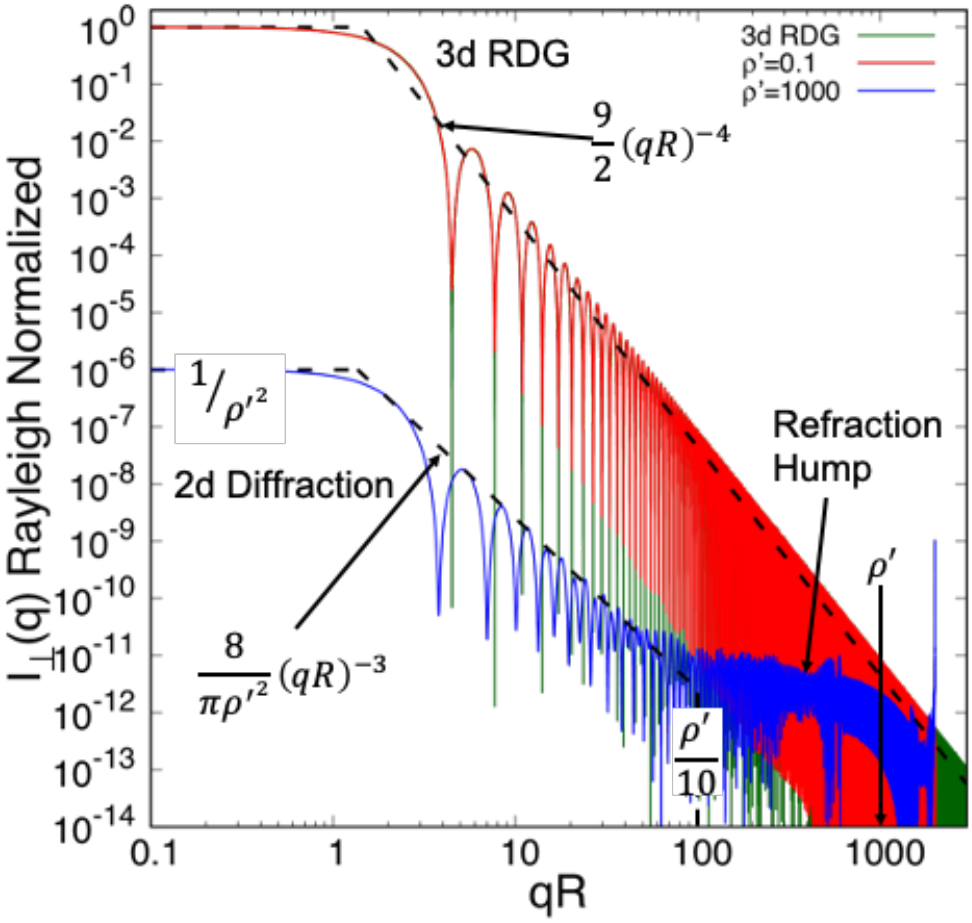

Fig. 3.2 RDG scattering curve for a sphere calculated using Eq. (2.35) (green). Rayleigh normalized Mie scattering for a sphere with a $\rho' = 0.1$ (red) and $\rho' = 1000$ (blue).

3.3 Q-space Analysis

As stated in the introduction, under the umbrella of what is referred to as q-space analysis is the systematic study of the light scattering plotted in q-space. The natural place to begin a systematic study of the light scattering from spheres is when $\rho' < 1$, which has already been covered in chapter 2. The $\rho' < 1$ results of the Rayleigh normalized light scattering by a sphere can be summarized as follows, the forward scattering lobe goes as

$$I_{\perp,RN}(0 \leq qR \lesssim 1) = 1. \tag{3.21}$$

The scattering then reaches the Guinier regime when $qR \approx 1$ and then transitions into the power law regime *w*here the average scattering in the power law regime goes as

$$I_{\perp,RN}(1 \lesssim qR) = \frac{9}{2}(qR)^{-4}. \tag{3.22}$$

To examine the behavior of the Rayleigh normalized Mie scattering as the scattering begins to leave the 3d RDG limit, Fig. 3.3 shows the scattering of spheres with an index of refraction $m = 1.3 + i0.0$, and size parameters kR such that $\rho' = 0.3, 1, 3, 10, 30$. The scattering has been calculated using a small log-normal size distribution with deviation of $\sigma = 1.05$ [45] to wash out the ripples but leave the overall behavior. When $\rho' = 0.3$ the Rayleigh normalized Mie scattering in the forward direction goes at slightly above unity, instead of at or below the 3d RDG limit, there is a Guinier regime around $qR \approx 1$ at which point the scattering has reached its maximum qR of $2kR$. When $\rho' = 1$, the forward scattering again goes at a value above the 3d RDG limit and then turns down at the Guinier regime and begins to follow the 3d RDG scattering.

As ρ' increases, the Rayleigh normalized forward scattering begins to decrease but does not go at exactly $1/\rho'^2$ yet. Fig. 3.3 shows that when $\rho' = 10$ the forward scattering has started to approach $1/\rho'^2$ and by $\rho' \sim 30$ it is almost equal to $1/\rho'^2$. Now we can answer the question

"how large is a sufficiently large refractive index," the answer being large enough that $\rho' \gtrsim 30$ [50]. When $\rho' = 3$ and 10 the power law regime begins to develop away from the 3d RDG limit with a slope of -4 and develops a region with a quasi-power law of over the refraction ripples ~-2. The slope of -2 was found when plotted vs the phase shift parameter ρ [51,52], which is closely related to ρ' and was used before the development of ρ' [11]. The quasi-power law of ~-2 is followed before the scattering meets up and begins to follow the 3d RDG slope of -4, finally at large qR it reaches the enhanced backscattering.

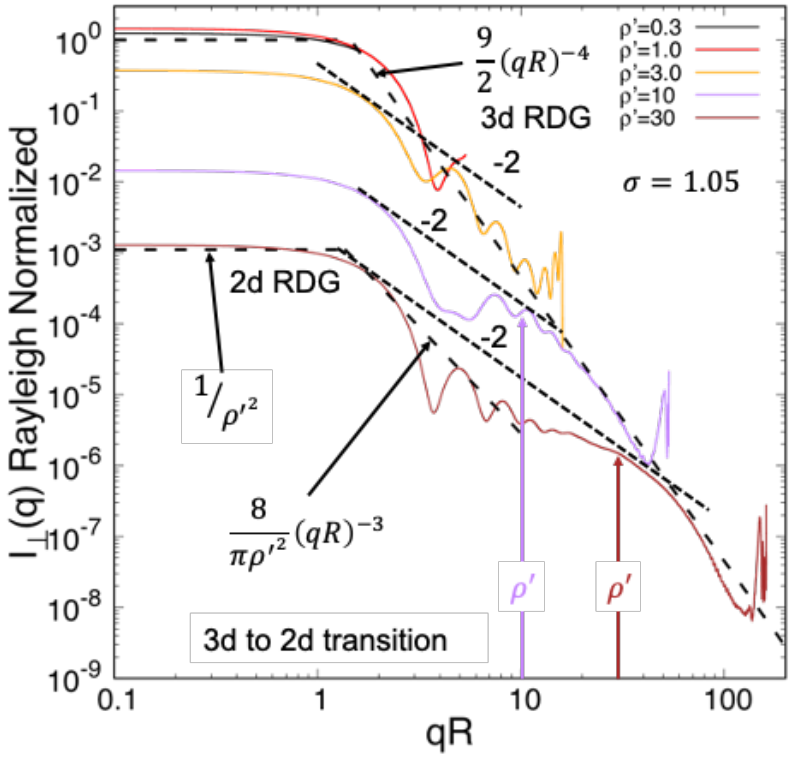

Fig. 3.3 Rayleigh normalized Mie scattering curves for spheres with a relative refractive index of $m = 1.3 + i0.0$, and $\rho' = 0.3, 1.0, 3.0, 10, 30$. The scattering is calculated with a small log-normal size distribution with $\sigma = 1.05$.

When $\rho' = 10$ the development of the refractive hump begins, with the center of the hump located at approximately $qR \sim \rho'$, which is just before the scattering meets back up with the 3d RDG slope of -4. Once $\rho' = 30$ the 2d RDG limit in the forward scattering has been reached,

and there is a power law regime that follows Eq. (3.22). The power law of ~-2 remains as a tangential line connecting the Guinier regime and the refraction "hump" at around $qR{\sim}\rho'$ [50], whether there is any physical significance to this has not yet been determined. The hump for $\rho' = 30$ if fully developed and is centered around ρ', after which there is the enhanced backscattering at large qR.

The region of scattering with $0.3 < \rho' < 30$ is a transitional region, developing from the 3d RDG limit to the 2d RDG limit, and as such has a transitioning description. Starting with the forward scattering lobe the Rayleigh normalized scattering goes as

$$I_{\perp,RN}(qR < 1) \geq 1\,, \qquad 0.3 < \rho' < 3. \tag{3.23}$$

When $3 < \rho' < 10$, it can be seen in Fig. 3.3 that the forward scattering does not go at exactly $1/\rho'^2$ yet, but is approaching $1/\rho'^2$ as ρ' increases. By $\rho' = 10$, the Rayleigh normalized forward scattering is approximately going as $1/\rho'^2$ leading to

$$I_{\perp,RN}(qR < 1){\sim}\, 1/\rho'^2\,, \qquad 10 < \rho' < 30. \tag{3.24}$$

The scattering then reaches the Guinier regime when $qR \approx 1$ and then transitions into the power law regime *w*here the average scattering in the power law regime goes as

$$I_{\perp,RN}(qR > 1) \approx \frac{9}{2}(qR)^{-4}\,, \qquad 0.3 < \rho' < 3 \tag{3.25}$$

$$I_{\perp,RN}(\rho' > qR > 1) \propto (qR)^{-2}, \qquad 3 < \rho' < 30 \tag{3.26}$$

$$I_{\perp,RN}(qR > \rho') \propto (qR)^{-4}. \qquad 3 < \rho' < 30 \tag{3.27}$$

At large qR, the Rayleigh normalized scattering transitions into the enhanced backscattering.

To examine the large ρ' behavior Fig. 3.4 shows the scattering of spheres with an index of refraction $m = 1.3 + i0.0$, and size parameters kR such that $\rho' = 30, 100, 300, 1000$. The scattering has been calculated using a small log-normal size distribution with deviation of $\sigma = 1.05$ [45] to wash out the ripples but leave the overall behavior. In Fig. 3.4 there are four different shaded regions. The first is a green region that represents the 3d RDG scattering which

is described by Eq. (3.21) and Eq. (3.22). The second region in Fig. 3.4 is the 3d RDG to 2d RDG transition region, this is the region shown in Fig. 3.3 and described by Eq. (3.23)-Eq. (3.27). The third region is light blue, within this region the scattering is dominated by 2d diffraction. The fourth region is a light tan area in which the scattering is dominated by refraction effects, such as the refraction hump, generalized rainbows, and glories. The latter two are part of what is referred to as the enhanced back scattering.

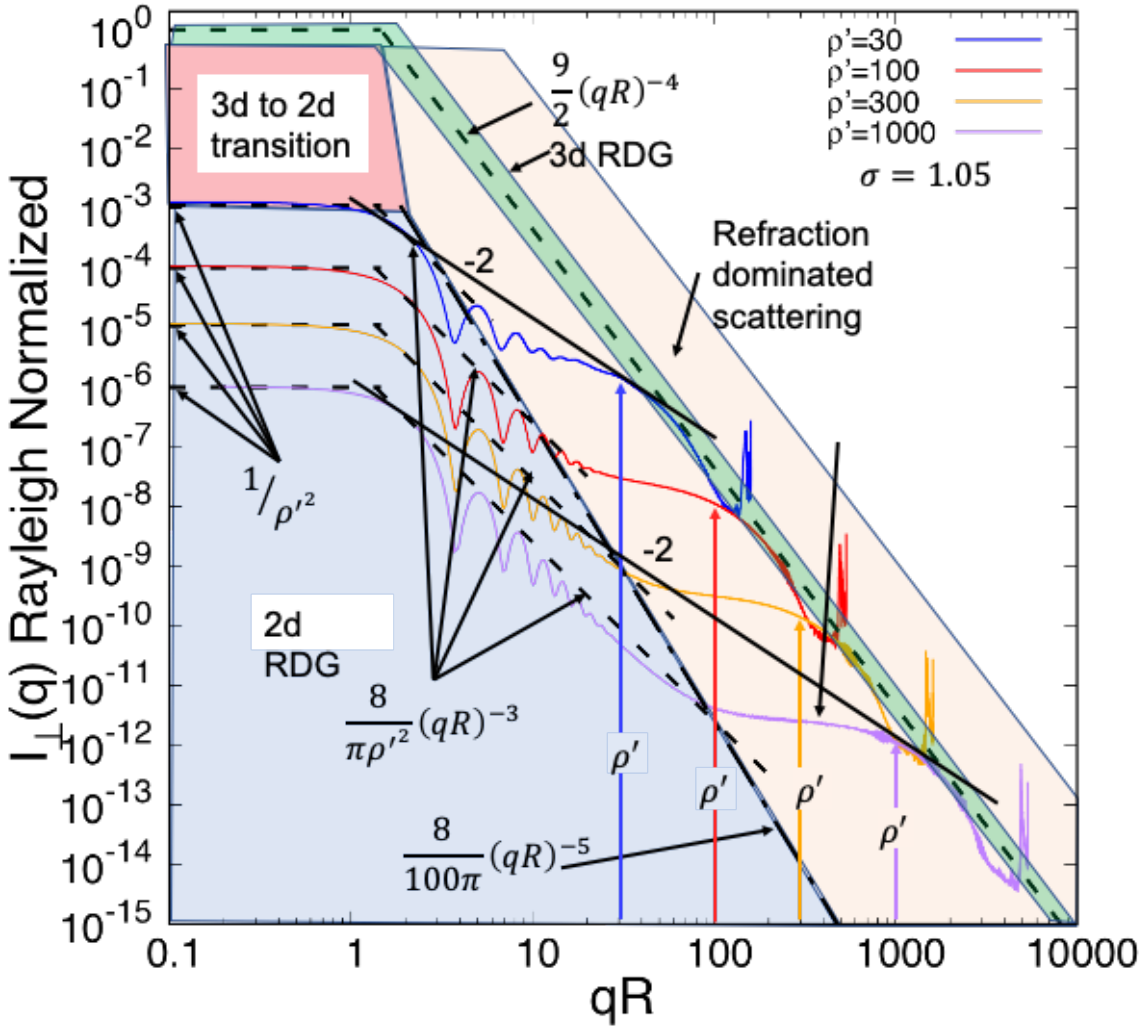

Fig. 3.4 Rayleigh normalized Mie scattering curves for spheres with a relative refractive index of $m = 1.3 + i0.0$, and $\rho' = 30, 100, 300, 1000$ plotted vs qR. The scattering is calculated with a small log-normal size distribution with $\sigma = 1.05$.

In the 2d RDG region the Rayleigh normalized forward scattering goes as

$$I_{\perp,RN}(qR < 1) = 1/\rho'^2, \qquad 30 \leq \rho'. \tag{3.28}$$

There is a Guinier regime when $qR \approx 1$ that marks the transition into the power law regime. In the power law regime, the scattering follows

$$I_{\perp,RN}\left(1 \lesssim qR \lesssim \frac{\rho'}{10}\right) \approx \frac{8}{\pi\rho'^2}(qR)^{-3}, \qquad 30 \leq \rho'. \tag{3.29}$$

After the scattering follows Eq. (3.29), it transitions into the refraction dominated region. The dividing line of these two regions is given by $\approx (8/100\pi)(qR)^{-5}$. Once the scattering enters the refraction dominated region, the scattering develops into the refraction hump that is centered around $qR \approx \rho'$. The tangential line with a slope of -2 between the Guinier regime and the center of the refraction hump remains. After $qR \approx \rho'$ the scattering turns down as it touches up with the 3d RDG line and finally at larger qR develops into the enhanced back scattering.

We have seen through Fig. 3.3 and Fig. 3.4 that the Rayleigh normalized scattering from spheres appears to show a quasi-universality with the internal coupling parameter ρ'. So far only a single refractive index has been used, for the prescribed behavior of the Rayleigh normalized scattering to truly be quasi-universal with ρ' any combination of size and index that lead to a specific ρ' should have approximately the same description. To investigate this further Fig. 3.5(a) shows the Rayleigh normalized forward scattering vs ρ' for the real part of the index of refraction $n = 1.3, 1.5, 2.0, 2.5$ and thus have different sizes when they have the same ρ'. In Fig. 3.5(a) it can be seen that the Rayleigh normalized scattering in the forward direction goes as unity when $\rho' \lesssim 0.3$ for all of the distinct refractive indexes, as was demonstrated in [11,50].

As the Rayleigh normalized forward scattering approaches unity, it begins to increase and there is a distinct separation with index. This region is the transitional region between the 3d

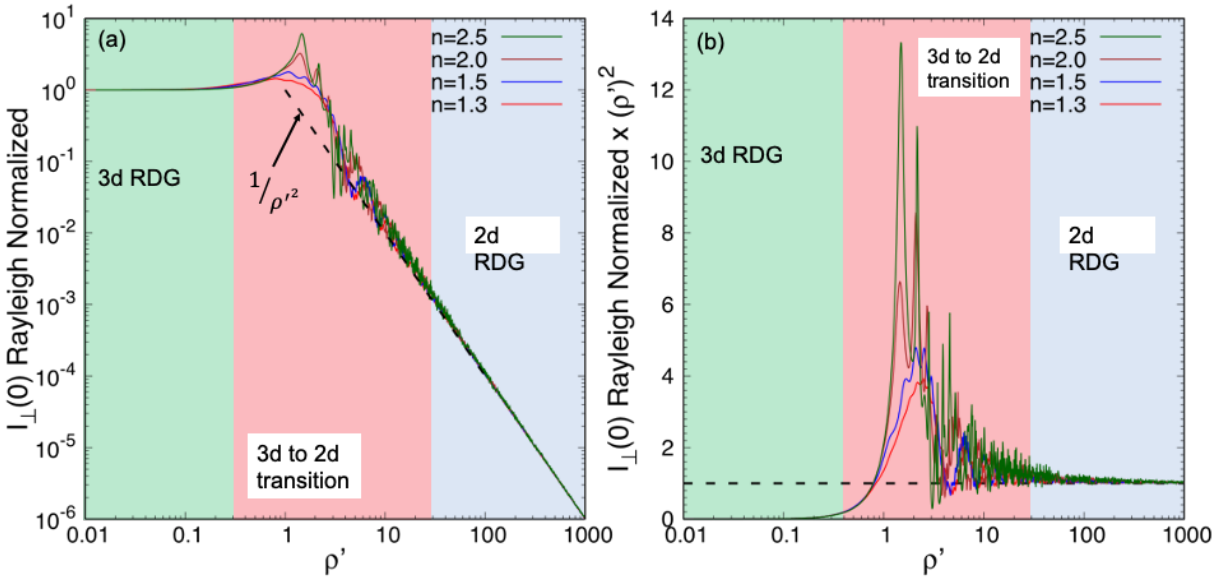

Fig. 3.5 Rayleigh normalized forward scattering vs ρ' (a). Rayleigh normalized forward scattering times ρ'^2 (b).

RDG and the 2d RDG. The quasi-universality breaks down some in this region, why this occurs is not clear and would be a worthy subject for further investigation in the future. Nevertheless, ρ' still describes the range in which the 3d to 2d transition takes place, and as the forward scattering approaches $\rho' \sim 10$ all of the curves for different indexes have begun to settle down and approach $1/\rho'^2$. Fig. 3.5(a) shows that at approximately $\rho' \sim 30$ the scattering goes at or just slightly above $1/\rho'^2$ and only improves as ρ' increases. Fig. 3.5(b) displays the same data as Fig. 3.5(a) only it has been multiplied by ρ'^2 [11,50]. Finally, Fig. 3.6 shows the Rayleigh normalized scattering from spheres with real parts of the refractive index of $n = 1.3, 1.5, 2.0, 2.5$, and for each index a $\rho' = 3, 10, 30, 100, 300,$ and 1000. It can be seen that even though there are a range of indexes and sizes, the curves of the Rayleigh normalized scattering with the same ρ' follow the same overall behavior that has been previously described. Fig. 3.6 demonstrates the quasi-universal nature of the Rayleigh normalized light scattering by a sphere of arbitrary index and size, with the parameter ρ'.

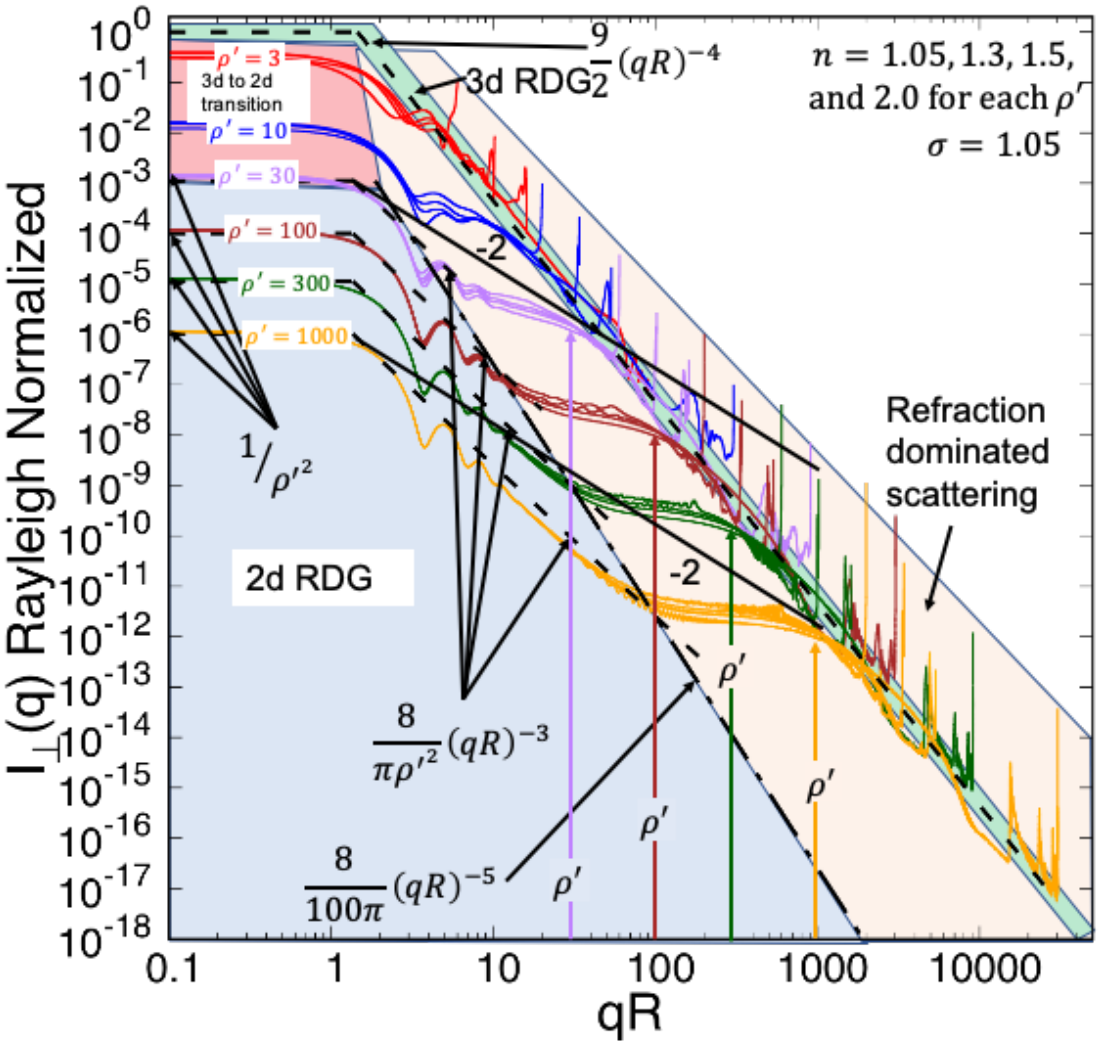

Fig. 3.6 Rayleigh normalized Mie scattering curves for spheres with real part of the relative refractive index of n= 1.05, 1.3, 1.5 and for each index a R such that $\rho' = 3, 10, 30, 100, 300, 1000$ plotted vs qR. The scattering is calculated with a small log-normal size distribution with $\sigma = 1.05$.

3.4 Effects of Absorption

While the main focus of this work is on scattering, absorption effects the scattering and thus cannot be ignored. Much like ρ' is a quasi-universal parameter to describe the scattered light, the product of the imaginary part of refractive index κ and the size parameter kR provides a universal parameter κkR to describe the effects on the scattering due to absorption [49,50,53,54]. Specifically, κkR describes the effects of absorption on the refraction components

of the scattering, as diffraction is unaffected by absorption and reflection is only significantly affected when $\kappa \gtrsim 1$ [54]. Most of what follows in this section has been presented in whole or part in (Maughan and Sorensen) [49].

To understand κkR consider a plane mono-chromatic electromagnetic wave that is incident upon a homogenous sphere of radius R. When the sphere has a non-zero imaginary part of the refractive index, the electromagnetic wave will be attenuated as it travels through the sphere. The distance that the wave has penetrated into the sphere when the amplitude of the wave has been attenuated by a factor of $1/e$ is known as the skin depth and is given by [25]

$$\delta = \frac{\lambda}{2\pi\kappa}. \tag{3.30}$$

The relative skin depth can then be expressed as a ratio of Eq. (3.30) and the radius of the sphere

$$\frac{\delta}{R} = \frac{\lambda}{2\pi\kappa R} = \frac{1}{\kappa kR}. \tag{3.31}$$

Eq. (3.31) tells us that the when $\kappa kR \ll 1$ the skin depth will be much larger than the radius of the sphere R and the refraction aspects of the scattering will show only a slight (if any) effect. As κkR increases, the relative skin depth will become smaller, and when κkR approaches unity the skin depth will become comparable to the size of the sphere and the refraction effects will start to become significantly reduced. When $\kappa kR \gtrsim 1$ the refractive effects of the scattering will be almost completely diminished and only the diffraction and reflection components of the scattering will be left [49,53]. Once $\kappa kR = 10$ the relative skin depth will only be one tenth of the radius and only a "cap" of the sphere on the side that the wave is incident upon will be illuminated.

Fig. 3.7 shows the Rayleigh normalized scattered intensity vs q for two spheres with a real part of the refractive index $n = 1.33$, and size parameters of $kR = 300$, and 1000, giving $\rho' \approx 122,408$. The imaginary part of the refractive index has been set so that the absorption

parameter of the spheres is given by $\kappa kR = 0.0, 0.1, 0.3, 1.0, 3.0, 10.0$. In Fig. 3.7 it can be seen that the changing of κkR does not affect the 2d RDG region of the scattering, as this is a diffraction dominated region and by the formulation presented in chapter 2 is independent of κ. Also shown in Fig. 3.7 are the orange and brown dashed lines that are the diffraction and reflection components of the scattering, respectively, and the solid black curve that is the sum of the diffraction and reflection components of the scattering calculated based on [55]. In the refraction dominated region shown in Fig. 3.7 there is a clear impact on the refraction hump and the enhanced backscattering.

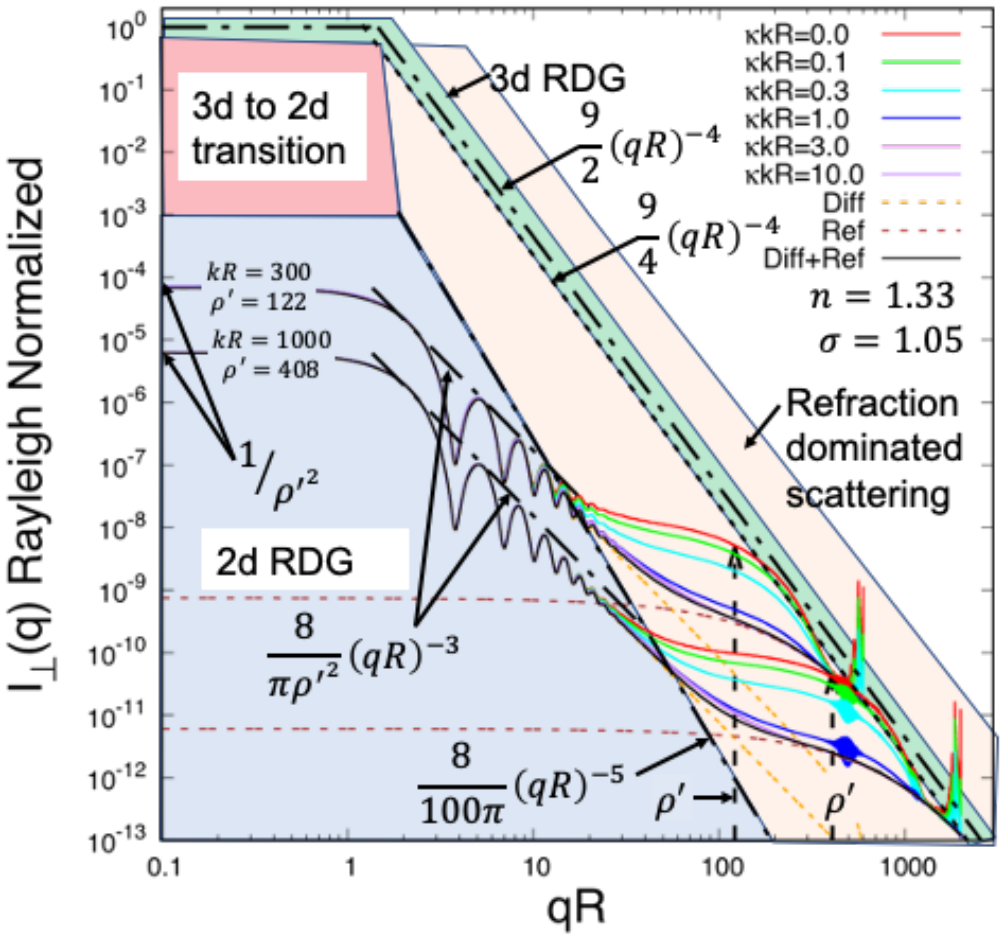

Fig. 3.7 Rayleigh normalized Mie scattering curves for spheres with real part of the relative refractive index of n= 1.33 and $kR = 300, 1000$ plotted vs qR. The imaginary part of the refractive index κ has been chosen so that $\kappa kR = 0.0, 0.1, 0.3, 1.0, 3.0, 10.0$. The scattering is calculated with a small log-normal size distribution with $\sigma = 1.05$.

When $\kappa kR = 0.1$, the skin depth is ten times the radius of the sphere, and there is only a minimal reduction in the refraction hump and enhanced backscattering as seen in Fig. 3.7. The reduction in these refraction effects continues as κkR passes through 0.3, when $\kappa kR = 1$ the skin depth is equal to the radius of the spheres and the refraction hump and enhanced backscattering are almost completely gone. Finally, once $\kappa kR = 10$ the refraction effects are nearly gone and the scattering in the refraction dominated region in Fig. 3.7 has been reduced till only the reflection component is left. The tail of the scattering, when $qR = 2kR$ and κkR is large enough that the refraction effects have been totally diminished, reaches out and touches the power law of $9/4\,(qR)^{-4}$ as found in [53].

Although the focus of this work is on the q-space analysis of the light scattered by particles, it is important not to ignore θ space. Plotting the scattering vs q on a log-log plot uncovers many quantifiable behaviors in q-space, but θ space is no less important and scattering phenomenon can in some cases be more readily apparent in θ space. Fig. 3.6 shows the same data plotted in Fig. 3.7, forward normalized and plotted vs θ on a log-normal plot, with the addition of radii of $R = 300\mu m,$ and $1000\mu m$. In θ space the reduction of the refraction effects with increasing κkR is more readily visible as can be seen in Fig. 3.8. In Fig. 3.8(a-d) various refraction effects can be seen. First for $\lambda/2R < \theta < 90°$ there is the refraction hump, that is followed by spikes in scattering at around $130°$ and $137.5°$; these are the secondary and primary rainbow peaks, respectively. Between the secondary and primary rainbows is a dark region known as "Alexanders band"[56]. Finally, in the back direction as θ approaches $180°$ there is the "Glory"[56]. In Fig. 3.8the reduction in these refraction effects as κkR increases can be seen more clearly than in Fig. 3.7, also when comparing the reduction in the refractive effects of each

radius there is a striking similarity in the reduction in the refraction effects with similar κkR [56]. It is important to take a moment and stress that κkR does not describe the refraction effects themselves but the reduction in them, the similarity in the reduction suggests that κkR is a universal parameter.

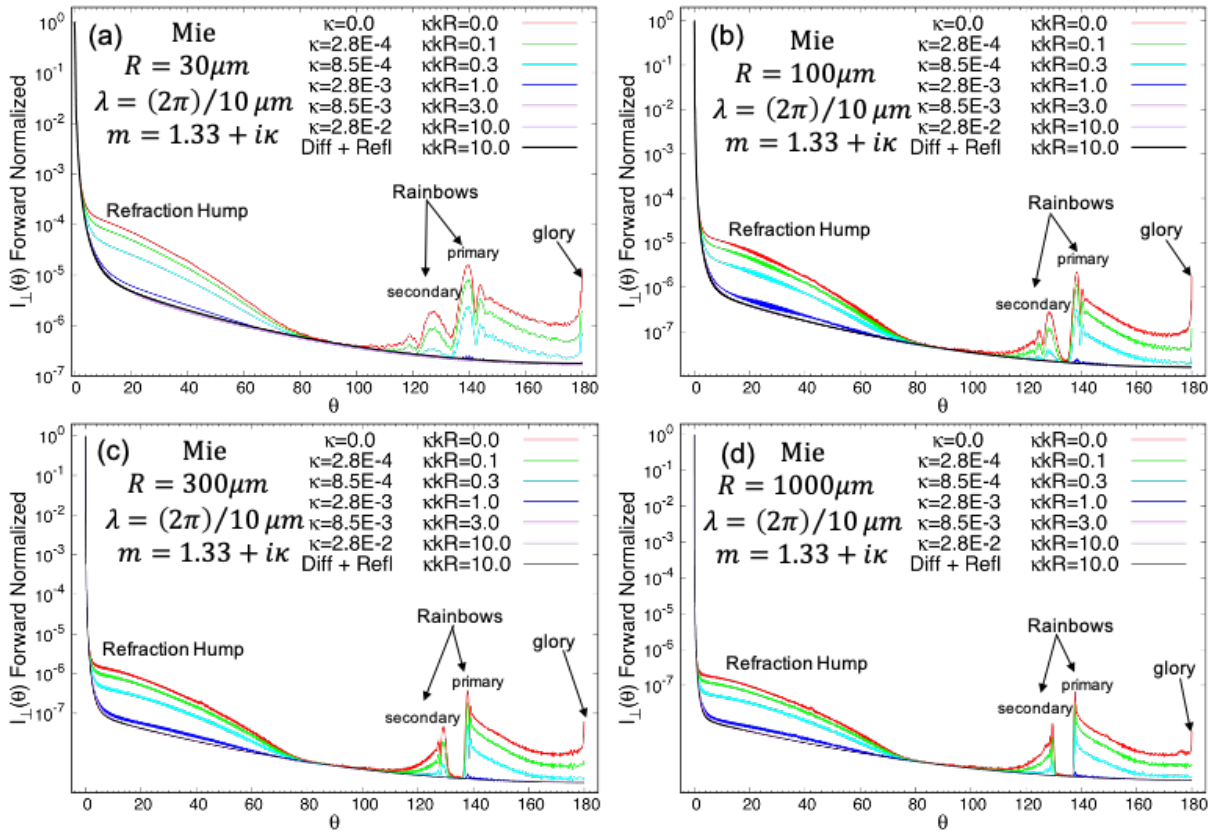

Fig. 3.8 Forward normalized scatted intensity versus the scattering angle (a). The Mie scattering for a sphere with a radius of $30\mu m$, and index of $m = 1.33 + i\kappa$. κ is varied so that $\kappa kR = 0.0, 0.1, 0.3, 1.0, 3.0, 10.0$ (b), (c), and (d) are the same as (a) but with radii of $100\mu m$, $300\mu m$, $100\mu m$, respectively.

To demonstrate the universality of κkR the scattering intensities from spheres with the same radii considered in Fig. 3.8 have been plotted together in Fig. 3.9 and Fig. 3.10. The full range of angles is shown in Fig. 3.9 and smaller ranges showing the individual refraction effects are shown in Fig. 3.10. As with Fig. 3.8, the imaginary part of the refractive index has been chosen such that there is a $\kappa kR = 0.0, 0.1, 0.3, 1.0, 3.0$ for each radius. The different radii have

different ρ' values and so plotting the Rayleigh normalized scattering would cause a separation in the curves. Forward normalizing the data would also cause a separation in the curves as the forward scattering is in the 2d RDG regime and which is solely dependent on the size parameter kR and is independent from κ. Instead, for a common point of reference the curves have been normalized by the Mie scattering of a sphere at 90°, with the same size parameter kR and real part of refractive index and an imaginary part of the refractive index such that $\kappa kR = 10$ [49].

Fig. 3.10 (a) shows the normalized scattering vs θ on a log-log plot up to a scattering angle of 30°, the curves in Fig. 3.10(a) are separated according to kR, demonstrating the kR dependance of the forward scattering. The first minimums are given by $\sim \lambda/2R$, following the first minimums the curves of equal kR can be seen to separate and regroup as curves of similar κkR. Fig. 3.10(b) shows the refraction hump when $\lambda/2R < \theta < 90°$, it can be seen that the reduction from the maximum when $\kappa kR = 0$ to when $\kappa kR = 3$ is described well by κkR despite having different κ and kR. In Fig. 3.10(c) the refraction rainbows are systematically reduced with κkR, and Fig. 3.10(d) shows a similar reduction in the glories with κkR. However, the larger scattering shows a more sensitive reduction in scattering effect with κkR than the forward angles, in the refraction hump a distinction can be made between $\kappa kR = 1$ and $\kappa kR = 3$, but in the backward directions $170° \leq \theta \leq 178.5°$ there is no distinction. As the scattering approaches 180° there is some separation in the curves of similar κkR, as the back directions are extremely sensitive to kR, and the real n and imaginary κ refractive indexes [57], yet κkR still does an excellent job of describing the reduction in the refractive effects, demonstrating its universal nature [49].

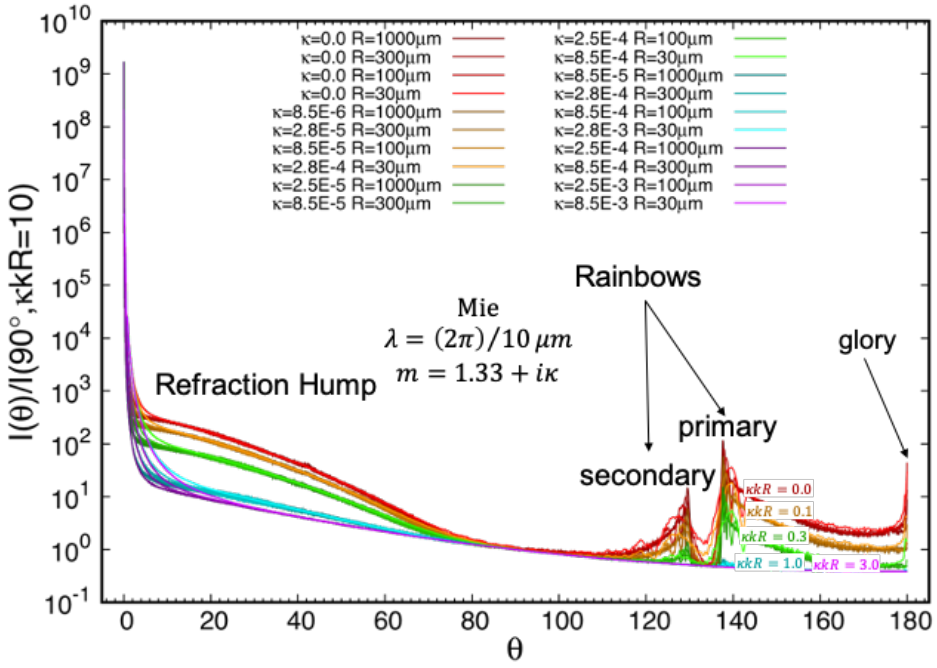

Fig. 3.9 Mie scattered intensity for spheres with radii of $30\mu m, 100\mu m, 300\mu m, 1000\mu m$ and index of $m = 1.33 + i\kappa$. κ is varied so that $\kappa kR = 0.0, 0.1, 0.3, 1.0, 3.0$ all are normalized by the scattered intensity of a sphere of the same size and with $\kappa kR = 10$, at $\theta = 90°$, with the entire scattering angle range shown.

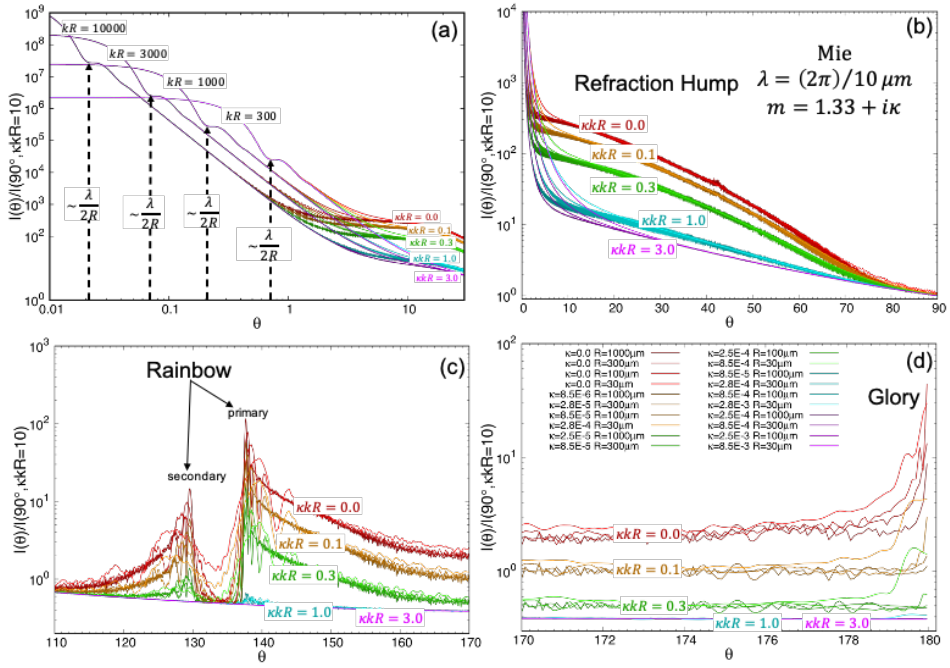

Fig. 3.10 Forward normalized scatted intensity versus the scattering angle θ (a). The Mie scattering for a sphere with a radius of $30\mu m$, and index of $m = 1.33 + i\kappa$. κ is varied so that $\kappa kR = 0.0, 0.1, 0.3, 1.0, 3.0, 10.0$ (b), (c), and (d) are the same as (a) but with radii of $100\mu m, 300\mu m, 100\mu m$ respectively.

Similar behavior that was demonstrated in Fig. 3.9 and Fig. 3.10, is shown using the same size spheres but with real parts of the refractive index given by $n = 1.5$ in Fig. 3.11 and Fig. 3.12 and $n = 2.0$ in Fig. 3.13 and Fig. 3.14. Fig. 3.12(a) and Fig. 3.14(a) both show the dependence of the scattering in the forward directions on kR, Fig. 3.12(b) and Fig. 3.14(b) shows the systematic reduction in the refraction hump from the maximum when $\kappa kR = 0$ to no hump when $\kappa kR = 3$. Fig. 3.12(c) shows a similar reduction in the generalized rainbows with κkR, one can see that the primary rainbow has pushed toward higher angles while the secondary has shifted toward smaller angles. While not obvious, Fig. 3.14(c) also shows the generalized rainbows due to the fact that the primary rainbow has shifted to the same angles as the glory, still the systematic reduction with κkR can be seen.

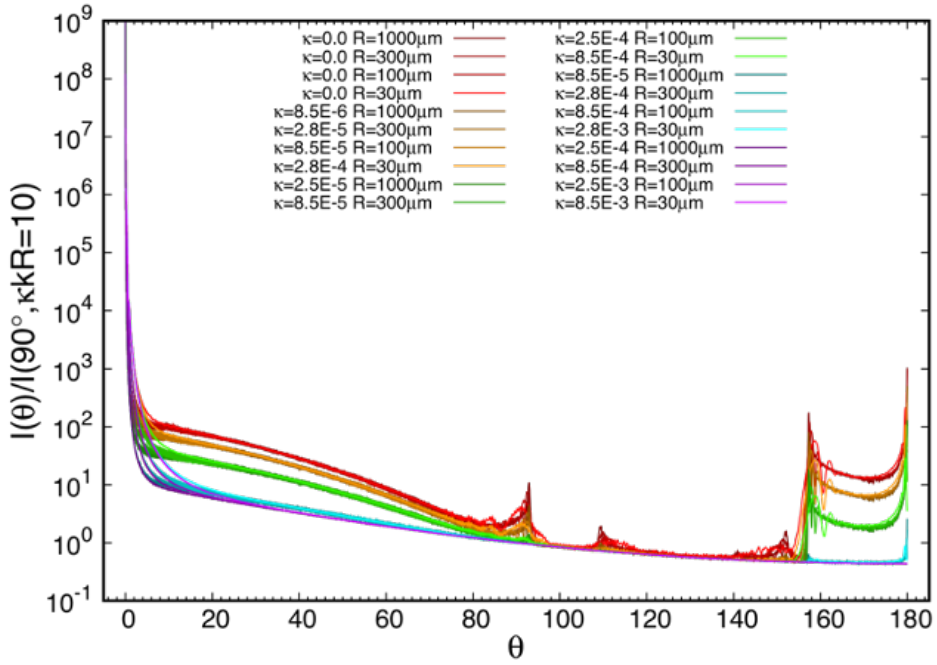

Fig. 3.11 Mie scattered intensity for spheres with radii of $30\mu m, 100\mu m, 300\mu m, 1000\mu m$ and index of $m = 1.5 + i\kappa$. κ is varied so that $\kappa kR = 0.0, 0.1, 0.3, 1.0, 3.0$ all are normalized by the scattered intensity of a sphere of the same size and with $\kappa kR = 10$, at $\theta = 90°$, with the entire scattering angle range shown.

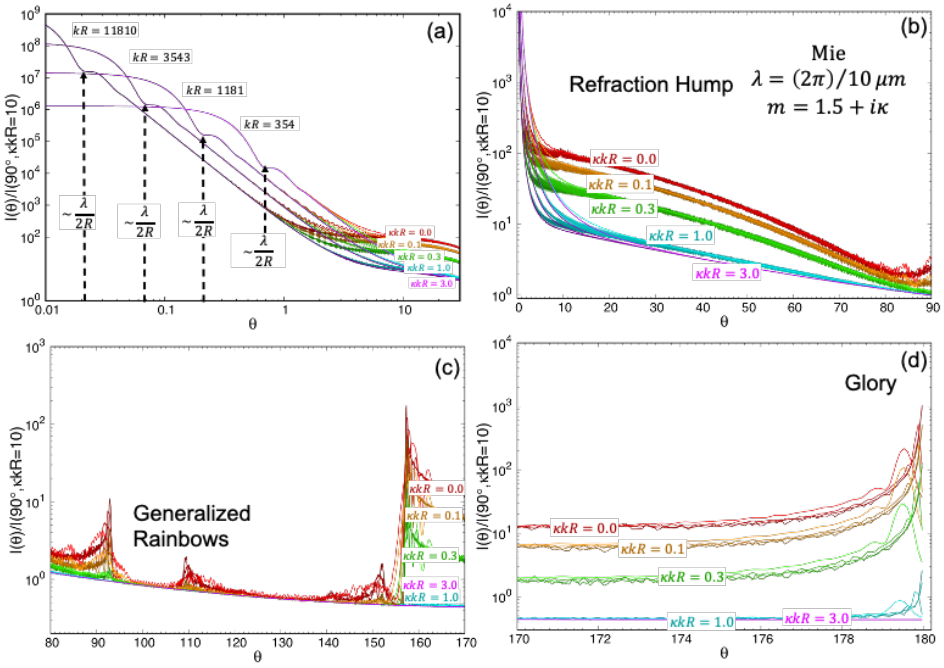

Fig. 3.12 Mie scattered intensity for spheres with radii of $30\mu m, 100\mu m, 300\mu m, 1000\mu m$ and index of $m = 1.5 + i\kappa$. κ is varied so that $\kappa kR = 0.0, 0.1, 0.3, 1.0, 3.0$ all are normalized by the scattered intensity of a sphere of the same size and with $\kappa kR = 10$, at $\theta = 90°$, in four regions: (a) the forward scattering which is dependent on kR, (b) the refraction hump, (c) the rainbows, and (d) the glory.

In Fig. 3.12(d) and Fig. 3.14(d) the glories are shown once again with systematic reduction with κkR, however there can be seen a separation between curves of $\kappa kR = 1$ and $\kappa kR = 3$ during the last $\sim 2.0°$ of scattering, that was not seen for $n = 1.33$ [49]. The distinction in the last $\sim 2.0°$ of scattering comes from the fact that there are distinct refractive effects leading to the glories when the index is $n = 1.33$, as opposed to when the index is $n = 1.5$ and $n = 2.0$. Details on the distinctions will be discussed in the following section. Although the refractive mechanics for the glories seen in Fig. 3.10(d) differ from those of Fig. 3.12(d), and Fig. 3.14(d) the absorption parameter κkR still describes the systematic reduction in these refraction effects [49].

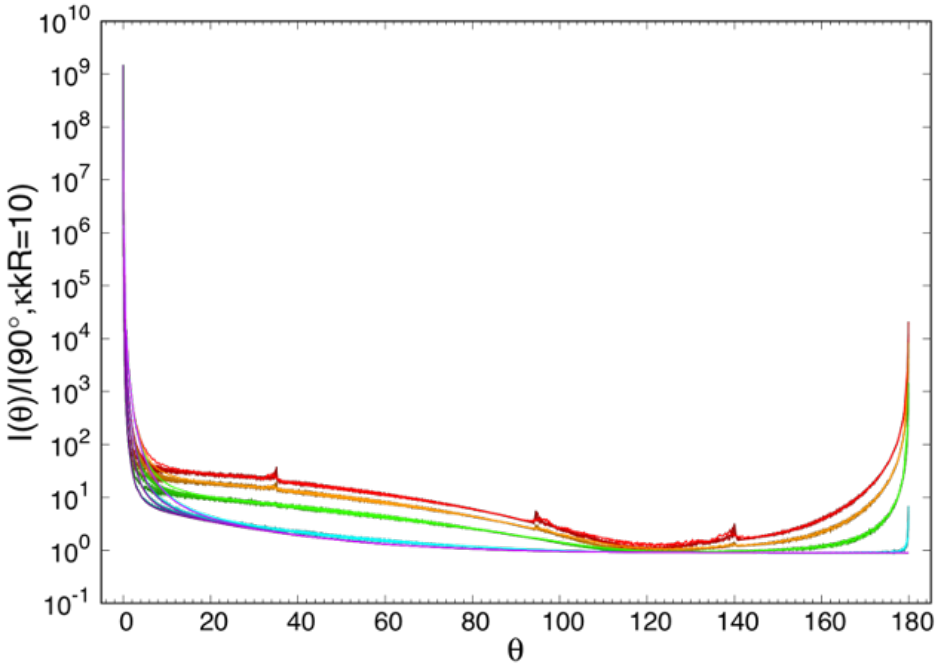

Fig. 3.13 Mie scattered intensity for spheres with radii of $30\mu m, 100\mu m, 300\mu m, 1000\mu m$ and index of $m = 2.0 + i\kappa$. κ is varied so that $\kappa kR = 0.0, 0.1, 0.3, 1.0, 3.0$ all are normalized by the scattered intensity of a sphere of the same size and with $\kappa kR = 10$, at $\theta = 90°$, with the entire scattering angle range shown.

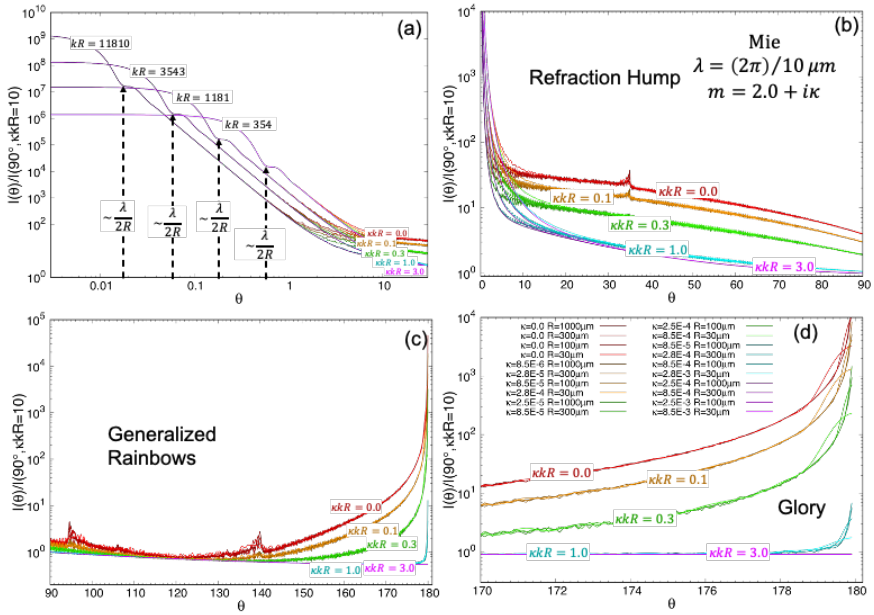

Fig. 3.14 Mie scattered intensity for spheres with radii of $30\mu m, 100\mu m, 300\mu m, 1000\mu m$ and index of $m = 2.0 + i\kappa$. κ is varied so that $\kappa kR = 0.0, 0.1, 0.3, 1.0, 3.0$ all are normalized by the scattered intensity of a sphere of the same size and with $\kappa kR = 10$, at $\theta = 90°$, in four regions: (a) the forward scattering which is dependent on kR, (b) the refraction hump, (c) the rainbows, and (d) the glory.

Fig. 3.15 thru Fig. 3.19 show the magnitude of the internal fields and the field near the surface of the spheres, relative to the magnitude of the incident field. The four radii that have been studied so far are shown in each figure. The figures show a two-dimensional slice through the sphere in the scattering plane ($x = 0$), with the x and y axis scaled by the radius of the spheres R. There is a white dashed line in each plot that represents the radius of the sphere in the plane, the incident field propagation direction is given by $\vec{k}_{inc}$, which lies along the positive z direction. Fig. 3.15 shows the case where $\kappa kR = 0$, it can be seen that the relative fields are fairly similar to each other despite the spheres being different sizes. There are bright areas both within and outside the sphere in the forward directions along the z/R axis, on either side of these bright areas are dark regions where the relative fields are less than 0.1. The remainder of the sphere is close to or below the incident field [49].

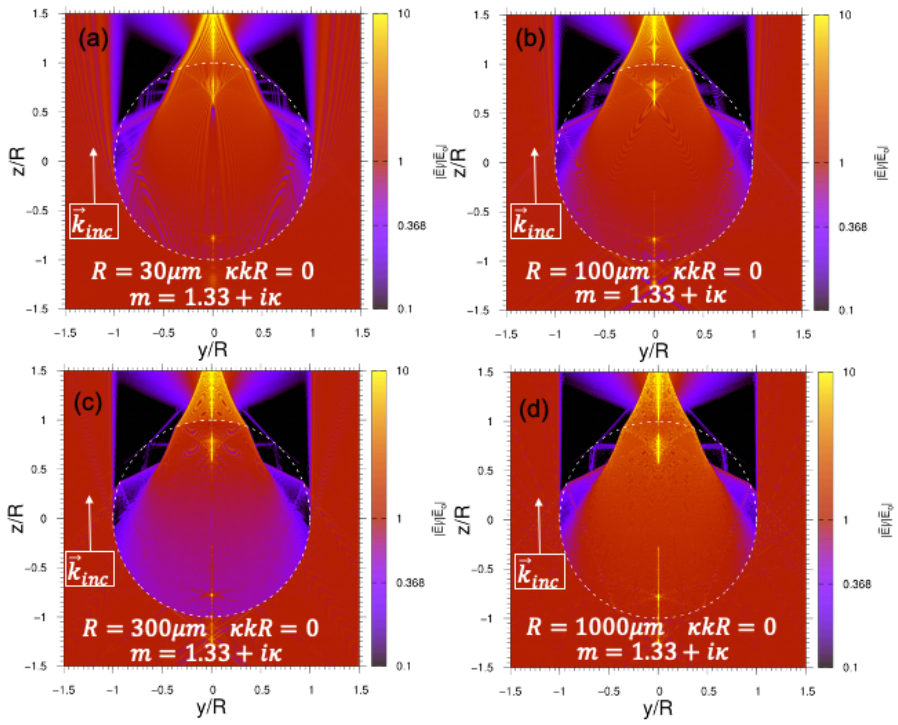

Fig. 3.15 (a) The relative internal and near field amplitudes for a slice of the sphere at $x = 0$ and with a radius of $30\mu m$ and index of $m = 1.33 + i0.0$ with a $\kappa kR = 0.0$. (b), (c), and (d) are the same as (a) but with radii of $100\mu m, 300\mu m, 1000\mu m$ respectively.

In Fig. 3.16 $\kappa kR = 0.3$, the skin depth is still larger than the entire sphere, but the absorption is starting to affect the internal fields. There is a very slight dimming in all of the internal fields, the bright spots along the z/R axis are not as bright and some of the faint purple lines across the dark areas to the left and right of the bright spots have gone. What is most important to note though is the similarity of the change from Fig. 3.15 to Fig. 3.16 even though the spheres are different sizes.

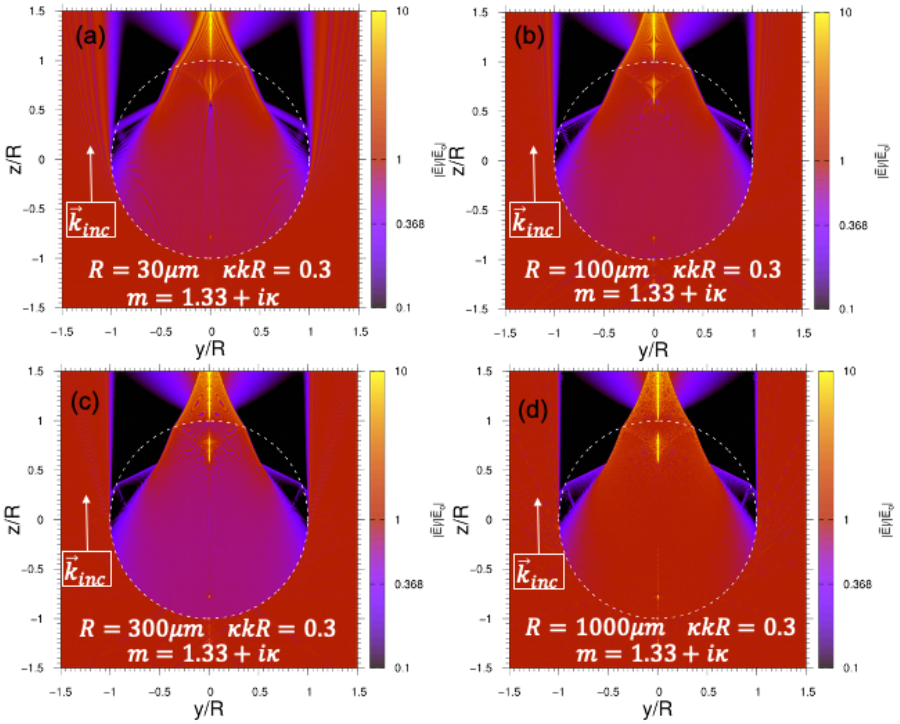

Fig. 3.16 (a) The relative internal and near field amplitudes for a slice of the sphere at $x = 0$ and with a radius of $30\mu m$ and index of $m = 1.33 + i0.0$ with a $\kappa kR = 0.3$. (b), (c), and (d) are the same as (a) but with radii of $100\mu m, 300\mu m, 1000\mu m$ respectively.

In Fig. 3.17 $\kappa kR = 1$, and now the relative skin depth is equal to unity, which is displayed as a white line in the figure. As before there is a continued overall dimming of the fields and only a small sliver of the bright spots remains. Again, the change in the relative internal fields when $\kappa kR = 0.3$ compared to $\kappa kR = 1$ is similar for all four radii.

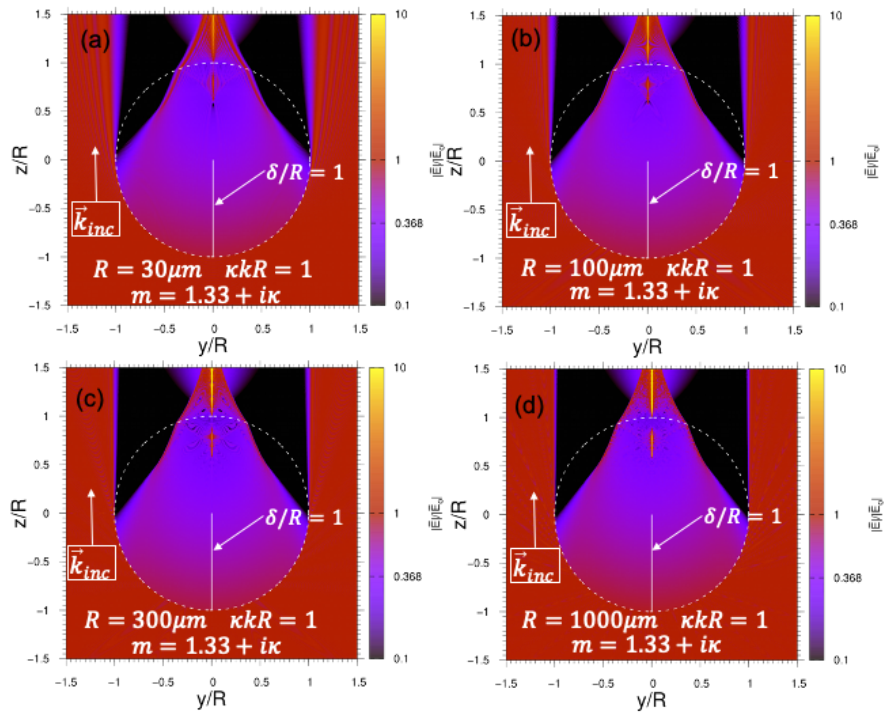

Fig. 3.17 (a) The relative internal and near field amplitudes for a slice of the sphere at $x = 0$ and with a radius of $30\mu m$ and index of $m = 1.33 + i0.0$ with a $\kappa kR = 1.0$. (b), (c), and (d) are the same as (a) but with radii of $100\mu m, 300\mu m, 1000\mu m$ respectively.

In Fig. 3.18 $\kappa kR = 3$ and the relative skin depth $\delta/R = 1/3$, and now it can be seen that there is significant darkening of the relative internal fields within the spheres. The bright spots have been totally eliminated; it can be seen that the relative skin depth describes well the $1/e \approx 0.368$ point. Again, the change from Fig. 3.17 to Fig. 3.18 is strikingly similar despite the sizes of the spheres being different. Finally, in Fig. 3.19 $\kappa kR = 10$ and only a small "cap" on the incident side of the sphere remains. The striking similarity in the reduction of the relative internal fields with increasing κkR serves to demonstrate the universality of κkR.

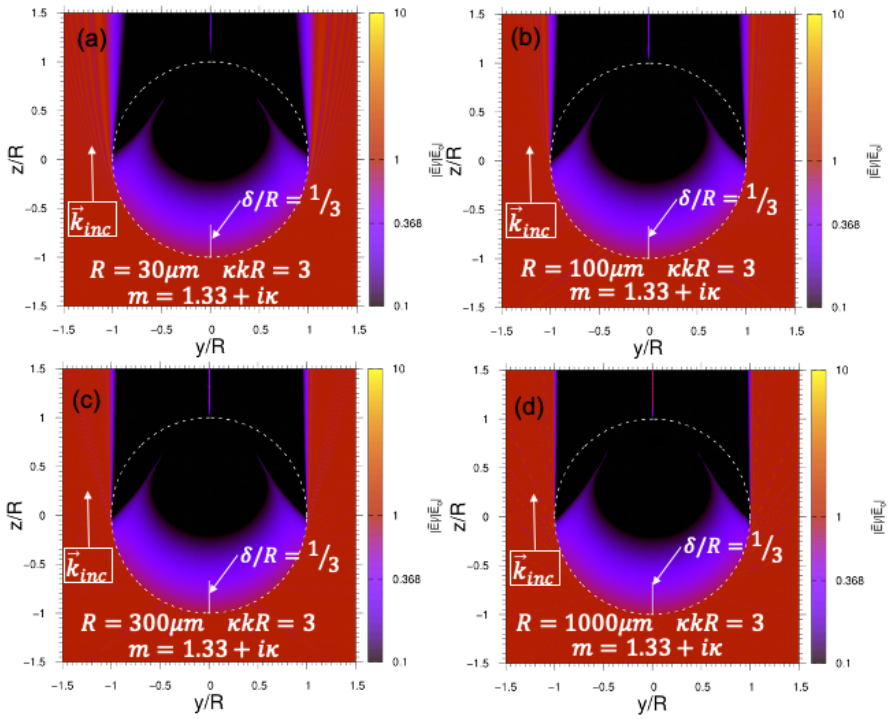

Fig. 3.18 (a) The relative internal and near field amplitudes for a slice of the sphere at $x = 0$ and with a radius of $30\mu m$ and index of $m = 1.33 + i0.0$ with a $\kappa kR = 3.0$. (b), (c), and (d) are the same as (a) but with radii of $100\mu m, 300\mu m, 1000\mu m$ respectively.

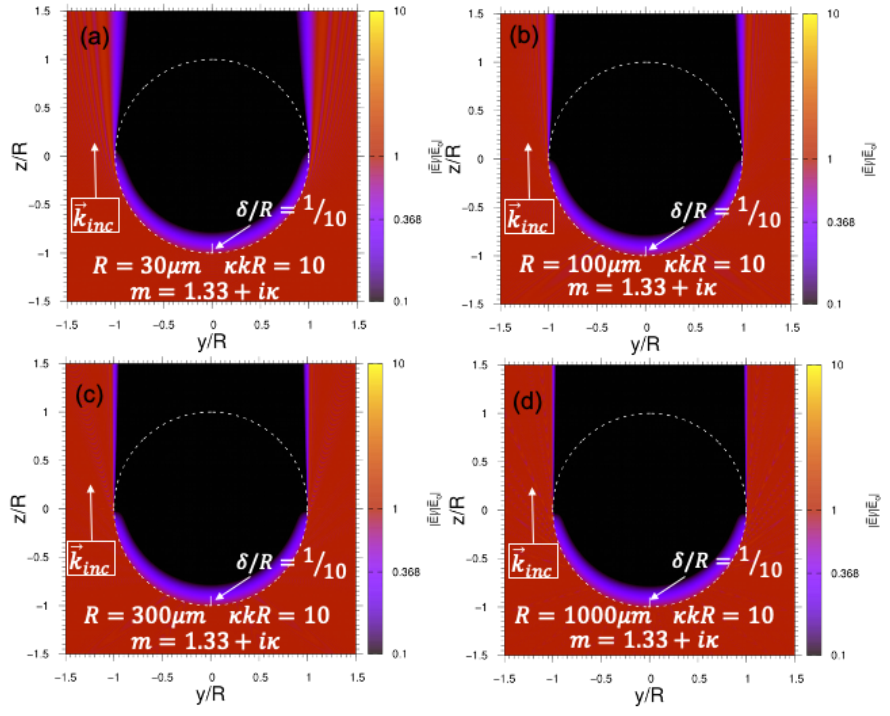

Fig. 3.19 (a) The relative internal and near field amplitudes for a slice of the sphere at $x = 0$ and with a radius of $30\mu m$ and index of $m = 1.33 + i0.0$ with a $\kappa kR = 10$. (b), (c), and (d) are the same as (a) but with radii of $100\mu m, 300\mu m, 1000\mu m$ respectively.

3.5 Generalized Rainbows and Glories

In this section I will briefly touch on generalized rainbows and glories. While generalized rainbows are a fairly straightforward topic, glories are not. Glories are caused by different refractive effects depending on the refractive index and size of the sphere. Indeed, an entire PhD project could probably be found within the complexity of the glories, and so I will only touch on them enough to describe why there is a distinction in the last 2° of Fig. 3.9, when compared to Fig. 3.11 and Fig. 3.13. The Debye series [56] can be used to gain some physical insight into generalized rainbows and glories. The physical insight is gained as parts of the series can be expressed independently, each part representing a ray that has experienced a distinct number or internal reflections within the sphere.

Generalized rainbows are predominately caused by the $p = 2$ (primary rainbow) term of the Debye series and $p = 3$ (secondary rainbow) term of the Debye series, where $p - 1$ is the number of enter reflections that the ray has experienced. The ray tracing scattering angle θ can be related to the incident angle θ_i by [58]

$$\theta - (p-1)180° + 2\theta_i - 2p\sin^{-1}\left({}^{\sin(\theta_i)}/_{n}\right), \tag{3.32}$$

and incident angle can be related to the impact parameter b by

$$b = \sin(\theta_i). \tag{3.33}$$

Fig. 3.20 shows the scattering angle θ vs the impact parameter b for the $p = 2$ and $p = 3$ rays at indexes of refraction $= 1.33, \sqrt{2}, 1.5, 1.7, 2.0$. In Fig. 3.20 when the curves pass through a region of zero slope there will be a range of impact parameters that all scatter at the same scattering angle. The grouping of a range of impact parameters into a single scattering angle causes an intensity spike in the scattering, these spikes are the generalized rainbows. In Fig. 3.20 it can be seen that as n increases from $n = 1.33$, the location of the primary rainbows caused by

the $p = 2$ rays (solid lines) shifts to larger angles, reaching 180° by $n = 2$. The secondary rainbows are caused by the $p = 3$ rays (dashed lines) and their location moves to smaller angles as the refractive index increases. Comparing Fig. 3.9, Fig. 3.11 and Fig. 3.13, it can be seen that the generalized primary and secondary rainbow locations move away from each other with increasing n.There are additional spikes in the scattering that appear, which are most likely caused by higher order terms in the Debye series.

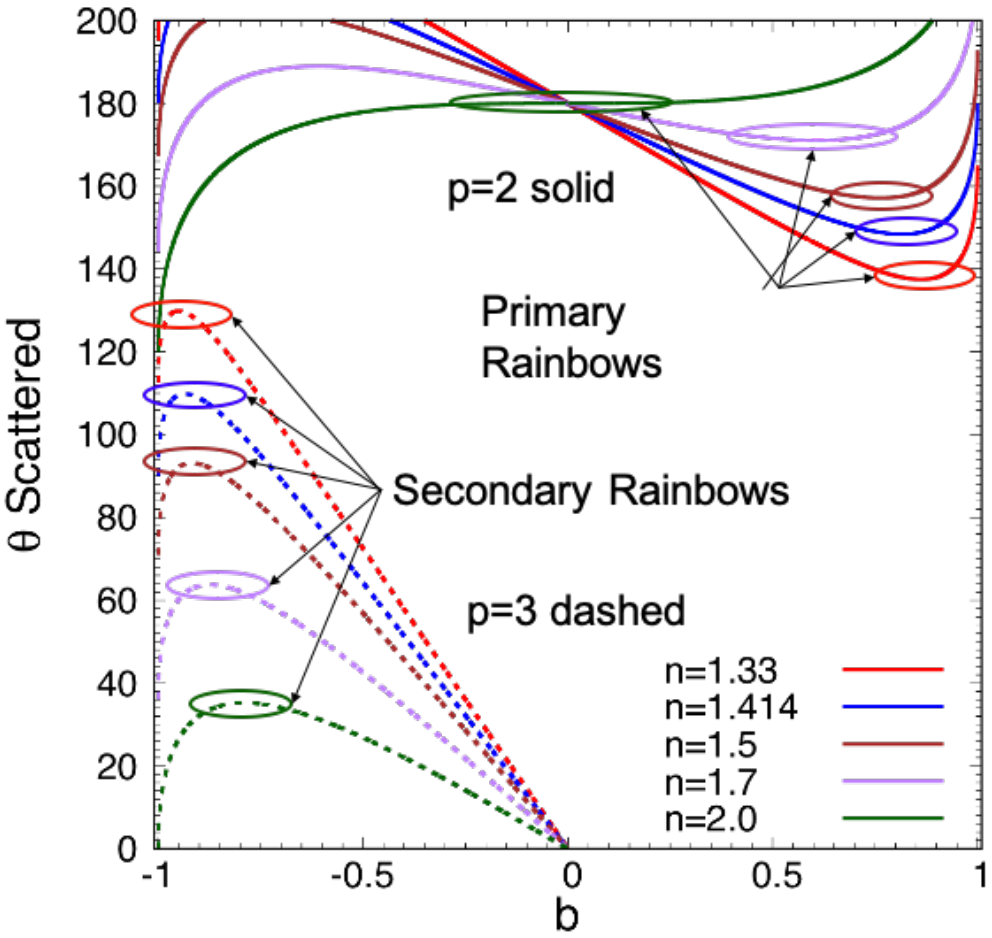

Fig. 3.20 Shows the scattering angles vs the impact parameter b for $p = 2$ rays (solid lines) which have one internal reflection, and $p = 3$ rays (dashed lines) which have two internal reflections. The curves shown are for a real part of the refractive index $n = 1.33, 1.414, 1.5, 1.7, 2.0$. The regions that have a slope of zero are circled.

When the real part of the index or refraction is $n = 1.33$, the glories are primarily the result of the $p = 2$ term in the Debye series when the size parameter $kR \lesssim 100$ [58] . Looking at Fig. 3.21, however, the only $p = 2$ rays that can scatter in the backward direction are those for very small impact parameters. All of the p terms in the Debye series will have rays that scatter in the backward direction for very small impact parameters, so there must be another phenomenon that causes the $p = 2$ rays to be the driving force in the glories for $n = 1.33$. The phenomenon that causes the p=2 rays to play a dominant role in the formation of the glories is the interference of surface waves that are produced by the $p = 2$ rays. These surface waves travel along the circumference of the sphere continuously shedding light, this allows for the constructive interference of the scattering surface wave in the backward directions [58]. Another consequence of the surface waves continuously shedding light is that as the size of their sphere increases, there is more circumference to travel and so less of the field is able to reach the backward directions leading to the $p = 2$ term becoming less dominant[58]. When the sphere size parameter becomes larger $kR > 100$, it is not the $p = 2$ but the $p = 11$ term in the Debye series that dominates [59–61].

Once $n \approx \sqrt{2} \approx 1.414$ there are $p = 2$ rays other than those for when b is small that can constructively interfere in the backward directions without surface waves. For example, when $n = \sqrt{2}$ the rays that have an impact parameter of -1 and 1 both scatter at $\theta = 180°$, and will constructively interfere. When n=2 there is an entire range of impact parameters from $b \sim -0.25$ to $b \sim 0.25$ that will scatter at $180°$. Not only will all of the rays scatter at $180°$, but the rays with equal but opposite impact parameters will constructively interfere. Indeed, upon examination of Fig. 3.13 there is a dramatic increase in the scattering at $180°$. It is the

distinction in the refractive mechanisms that cause the glories that lead to the difference in the behavior of the last 2° when comparing Fig. 3.9 to Fig. 3.11 and Fig. 3.13.

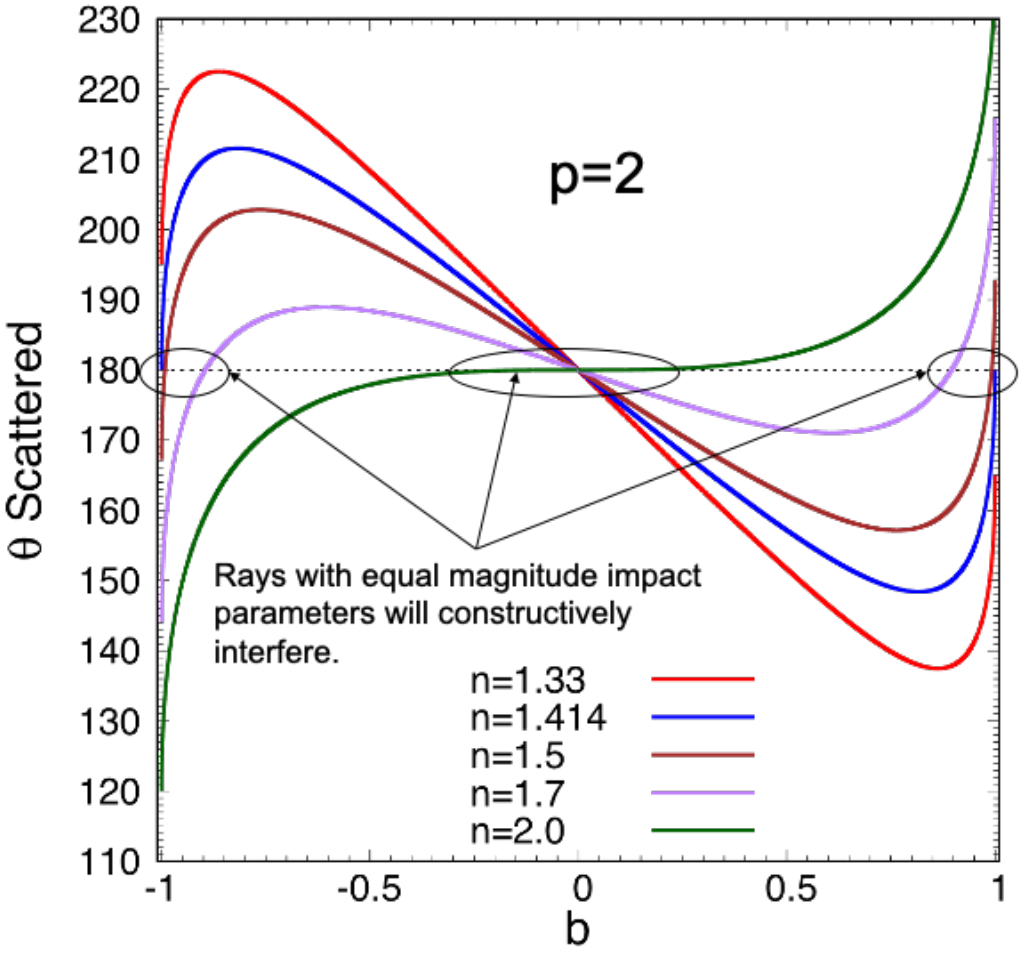

Fig. 3.21 Shows the scattering angles vs the impact parameter b for $p = 2$ rays. The curves shown are for a real part of the refractive index $n = 1.33, 1.414, 1.5, 1.7, 2.0$. When $n = 1.33$ the only impact parameters that scatter in the backward direction are those with small b, so surface waves are necessary for substantial scattering in backward directions. When n=1.414, 1.5, 1.7, 2.0 there are at least two impact parameters that will constructively interfere and lead to substantial scattering in the backward directions without surface waves.

Chapter 4 - Q-space Analysis of the Light Scattered by Non-Spherical Particles

Now that Q-space analysis has been applied to the light scattered by spheres, the same analysis can be applied to the light scattered by non-spherical particles as well. Undoubtedly there will be a great amount of variation in the scattering from particles of different shapes, sizes, aspect ratios and relative indexes of refraction. As mentioned before, however, the goal of this work is to take a big picture approach and look at the similarities in the scattered light. It will be demonstrated in the following, that just like with spheres, the internal coupling parameter ρ' provides a single parameter for classifying the regime the scattering is in. Also, as with spheres, it will be shown that the refraction dominated region of the scattering is where most of the variations in the scattered light are found, but even in this region some general quantitative descriptions can be made. Furthermore, it is in the refraction dominated region that the absorption parameter κkR provides a single parameter to describe the reduction in the variety of refraction effects to the base line of reflection. So, to study the scattered light from non-spherical particles we not only will need to be able to calculate the scattering by non-spherical shapes, but also the internal coupling parameter and the proper Rayleigh normalization for them.

There are a several different methods for calculating the light scattering by non-spherical particles. Different methods are deployed for different shapes, sizes, and refractive indexes. In this work to calculate the light scattering from various non-spherical shapes, four distinct computational programs and methods will be used. For fractal aggregates and spherical scattering volumes filled randomly with monomers the Multiple Sphere T Matrix (MSTM) program developed by Mackowski [62] will be used for all sizes and refractive indexes presented. The Invariant Imbedded T Matrix (IITM) developed by Ping Yang [63–66] is used

for cylinders, spheroids, rectangular prisms, hexagonal prisms, Gaussian random spheres (GRS), and droxtals for ρ' values up to $\rho' = 30$, when the real part of the refractive index $n \geq 2.0$, and up to $\rho' = 10$, when $n < 2.0$. The Physical Geometric Optics Method (PGOM) also developed by the Yang group [67] has been utilized for hexagonal prisms, rectangular prisms, and droxtals when $\rho' \geq 100$ when $n \geq 2.0$, and $\rho' \geq 30$ when $n < 2.0$. A ray optics program developed by Muinonen et al [35] named SIRIS was used for the calculation of the scattering by GRS with $\rho' \geq 100$ when $n \geq 2.0$, and $\rho' \geq 30$ when $n < 2.0$. Unfortunately, $\rho' > 30$ for spheroids and cylinders were not able to be reached in this current work.

4.1 The Non-Spherical Internal Coupling Parameter

Just as with a sphere the internal coupling parameter for an arbitrary shape can be derived by looking at the two limits of scattering. First consider a weakly refractive particle of arbitrary size, the scattering from the particle will be in the 3d RDG diffraction limit and the scattering in the exact forward direction $\theta = 0$ will be given by

$$\frac{dC_{sca,RDG,3D}}{d\Omega}(0) = k^4 V^2 |\alpha(m)|^2. \tag{4.1}$$

Now, considering a strongly refractive particle or arbitrary size with a sufficiently large refractive index. The scattering will be in the 2d RDG limit in the forward direction, and in this limit the scattering in the forward direction will be given by given by [30]

$$\frac{dC_{sca,RDG,2D}}{d\Omega}(0) = \frac{k^2 A^2}{4\pi^2}, \tag{4.2}$$

where A is the average projected area in the direction of the incident field. As with spheres we take the square root of the ratio of Eq. (4.1) and Eq. (4.2) which leads to

$$\rho' = 2\pi k \frac{V}{A} |\alpha(m)|. \tag{4.3}$$

Eq. (4.3) holds for any shape and reduces to Eq. (3.18) when the average volume polarizability of a sphere is used.

The question now is how one calculates the average volume polarizability for non-spherical particles, not only to calculate the proper ρ', but also so that the proper Rayleigh normalization given by Eq. (4.1) can be found. For spheroids there is an analytical solution the details of which can be found in [3,4] and is given by

$$|\alpha(m)|^2_{spheroids} = \frac{3}{4\pi}\left[2\left|\frac{(m^2-1)}{3+3L_a(m^2-1)}\right|^2 + \left|\frac{(m^2-1)}{3+3L_c(m^2-1)}\right|^2\right]. \tag{4.4}$$

L_a and L_c are geometric parameters given by the integrals

$$L_x = \frac{a^2 c}{2}\int_0^\infty \frac{dq}{(q+x^2)(q+a^2)\sqrt{(q+c^2)}}, \tag{4.5}$$

with x being either a or c, where a and c are the semi principle axes of the spheroid, two of which are described by c (see the appendix for examples). The geometric parameters L_a and L_c are restricted so that $2L_a + L_c = 1$ [4]. Other than Eq. (4.4) there are no other analytical solutions to the average volume polarizability for different shapes.

Although analytical solutions don't exist, computational calculations can be used to get a numerical value for $|\alpha(m)|$. Numerical programs such as IITM can be used to calculate the scattering properties of particles using a large wavelength and small size such that the particle in within the Rayleigh regime. The total scattering cross section in this regime is given by van de Hulst [3] as

$$C_{sca,Ray} = \frac{8}{3}\pi k^4 V^2 |\alpha(m)|^2. \tag{4.6}$$

Once the total scattering cross section in the Rayleigh regime has been solved for numerically, the average volume polarizability can be solved for as k and V are predetermined when running the scattering calculations. The average volume polarizability is a complex number and although

the magnitude is all that is required in this work theoretically it would also be possible to use the total absorption cross section to retrieve the imaginary component of polarizability. van de Hulst gives the total absorption cross section in the Rayleigh regime as

$$C_{abs,Ray} = 4\pi kVRe\big(i\alpha(m)\big), \tag{4.7}$$

again, k and V are known quantities and so the imaginary part of $\alpha(m)$ can at least be estimated. Once the magnitude and imaginary part of $\alpha(m)$ are known, the real part could also be determined. Only the retrieval of the magnitude numerically has been studied and was presented in Maughan et al. [68].

4.2 Q-space Analysis

Fig. 4.1(a) – Fig. 4.4(a) show the Rayleigh normalized scattering from cylinders, spheroids, hexagonal prisms and rectangular prisms, with aspect ratios $\varepsilon = 1/3\,, 1/2\,, 1, 2, 3,$ and real parts of refractive index of $n = 1.3, 1.5, 2.0, 2.5, 3.0$. The only exception is for spheroids with $\varepsilon = 1$, which are spheres and have already been covered. The sizes of the particles in Fig. 4.1 – Fig. 4.4 are such that $\rho' = 5, 10, 30$ for cylinders and spheres, while hexagonal, and rectangular particles have $\rho' = 5, 10, 30, 100, 300, 1000$. Fig. 4.1(b) – Fig. 4.4(b) show the Rayleigh normalized forward scattering vs ρ' for the same shapes, aspect ratios, and indexes as Fig. 4.1(a) – Fig. 4.4(a), with the addition of $\rho' = 0.1, 0.2, 0.5, 1, 2$. Fig. 4.5(a) shows the Rayleigh normalized scattering from GRS with relative standard deviations away from the mean radius $\sigma = 0.05, 0.1, 0.2$, power law indexes of ν=2, 3, 4, and real parts of the relative refractive indexes of $m = 1.3, 1.5, 2.0, 2.5, 3.0$, and mean radii a such that they have ρ'=5, 10, 30, 100, 300, 1000. Fig. 4.5(b) shows the Rayleigh normalized forward scattering vs ρ' for the same variations found in Fig. 4.5(a), with the addition of $\rho' = 0.1, 0.2, 0.5, 1, 2$. Fig. 4.6(a)

shows the Rayleigh normalized scattering from droxtals with $\theta_1 = 35.35°,\ \theta_2 = 71.81°$, and $\theta_1 = 1.5°,\ \theta_2 = 85°$, each with a real part of the refractive index of $m = 1.3, 1.5, 2.0, 2.5, 3.0$, and a circumscribing sphere radius R such that they have ρ'=5, 10, 30, 100, 300, 1000. Fig. 4.6(b) shows the Rayleigh normalized forward scattering vs ρ' for the same variations found in Fig. 4.6(a), with the addition of $\rho' = 0.1, 0.2, 0.5, 1, 2$.

In Fig. 4.1(b)-Fig. 4.6 (b) when $\rho' \lesssim 0.3$ no matter what the shape, aspect ratio, or refractive index the light scattering is in the 3d RDG region and the Rayleigh normalized scattering in the forward direction will go as unity

$$I_{\perp,RN}\left(0 \leq qR_{veq} \lesssim 1\right) = 1. \tag{4.8}$$

In the 3d RDG region the formulations of chapter 2 apply, as qR_{veq} increases away from the forward scattering directions the scattering passes through the Guinier regime and enters the power law regime. The scattering in the power law regime when the scattering is in the 3d RDG region, according to Eq. (2.46) will go as

$$I_{\perp,RN}\left(1 \lesssim qR_{veq}\right) = \frac{16\pi S R_{veq}^4}{9V^2}\left(qR_{veq}\right)^{-4}. \tag{4.9}$$

It can also be seen in Fig. 4.1(b)-Fig. 4.6(b) that for all of the shape and index variations, as ρ' approaches unity, the Rayleigh normalized scattering in the forward direction begins to increase above unity. This is the 3d to 2d transition region, and there is some dispersion with shape and refractive index, but for all cases the Rayleigh normalized forward scattering goes as

$$I_{\perp,RN}\left(qR_{veq} < 1\right) \geq 1\,. \qquad 0.3 < \rho' < 3 \tag{4.10}$$

When $3 < \rho' < 10$ it can be seen in Fig. 4.1(a)-Fig. 4.6 (a) and Fig. 4.1(b)-Fig. 4.6 (b) that the forward scattering does not go at exactly $1/\rho'^2$ yet, and there is still a large amount of dispersion due to both shape and refractive index. The Rayleigh normalized forward scattering, however,

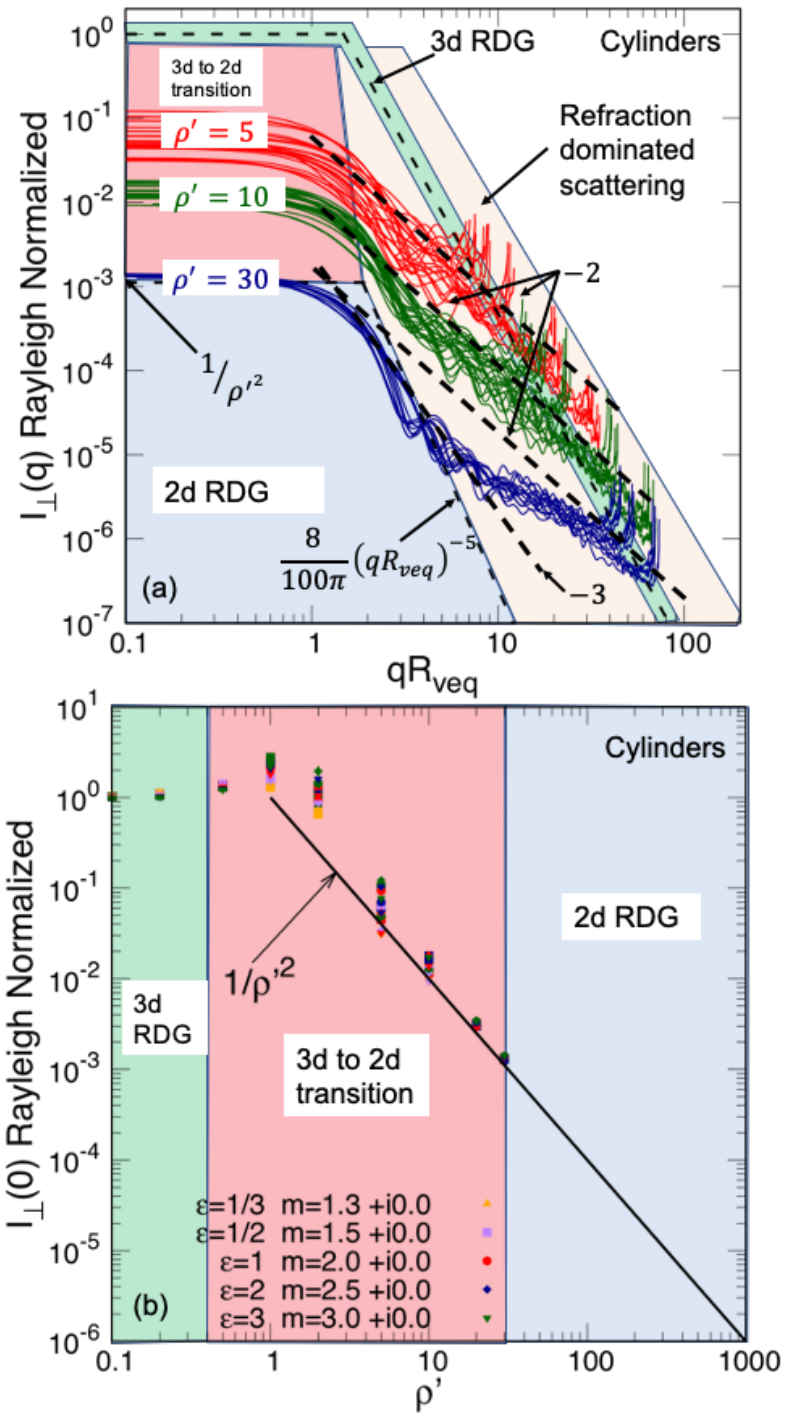

Fig. 4.1 (a) The Rayleigh normalized light scattered by cylinders with aspect ratios $\varepsilon = 1/3, 1/2, 1, 2, 3$, and real parts of refractive index of $n = 1.3, 1.5, 2.0, 2.5, 3.0$, and sizes such that $\rho' = 5, 10, 30$ in every possible combination of $\varepsilon, n,$ and ρ'. (b) The Rayleigh normalized scattering by cylinders in the forward direction for all curves shown in (a), and with the addition of $\rho' = 0.1, 0.2, 0.5, 1, 2$. In (b) the color of the point represents the relative refractive index and the point shape represents the aspect ratio.

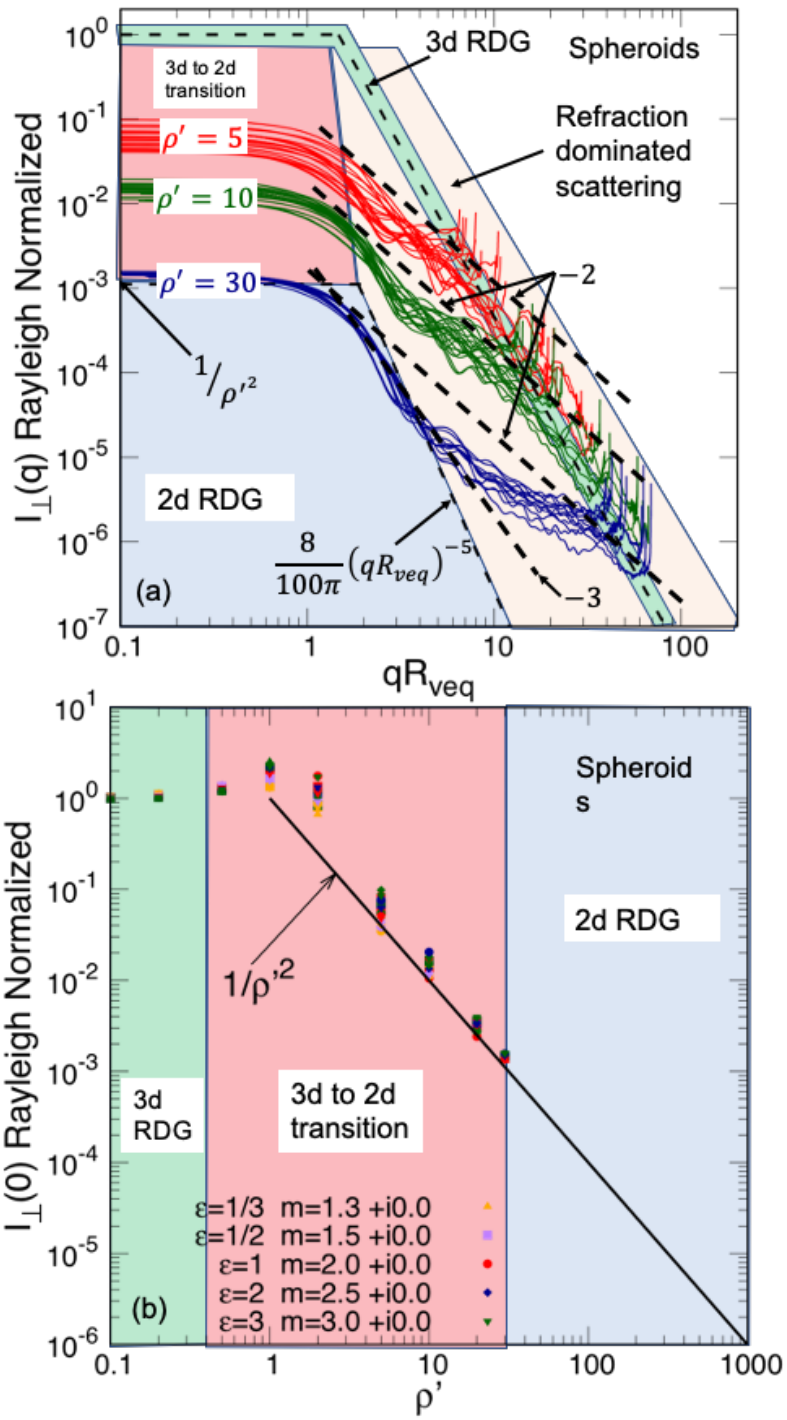

Fig. 4.2 (a) The Rayleigh normalized light scattered by spheroids with aspect ratios $\varepsilon = 1/3, 1/2, 2, 3$, and real parts of refractive index of $n = 1.3, 1.5, 2.0, 2.5, 3.0$, and sizes such that $\rho' = 5, 10, 30$ in every possible combination of $\varepsilon, n,$ and ρ'. (b) The Rayleigh normalized scattering by spheroids in the forward direction for all curves shown in (a), and with the addition of $\rho' = 0.1, 0.2, 0.5, 1, 2$. In (b) the color of the point represents the relative refractive index and the point shape represents the aspect ratio.

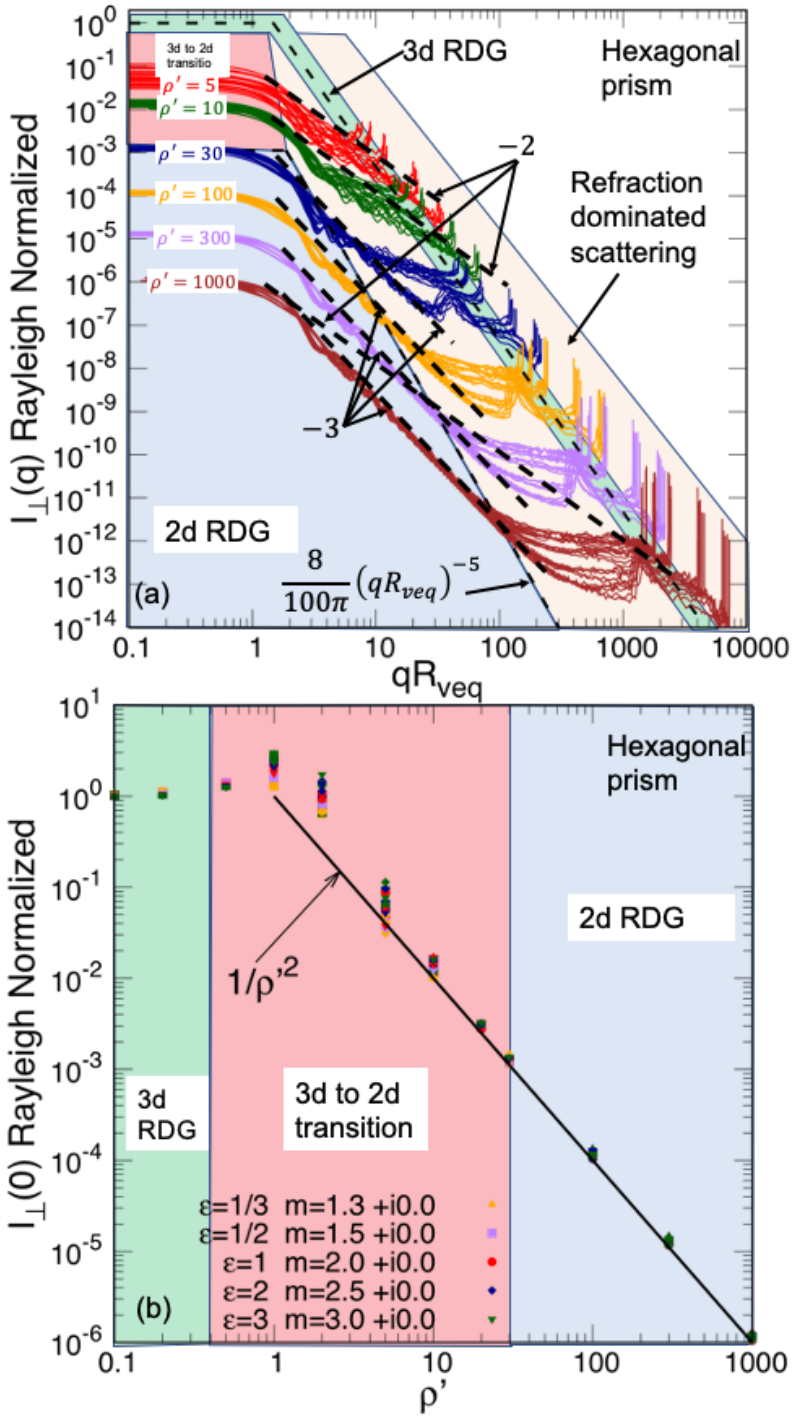

Fig. 4.3 (a) The Rayleigh normalized light scattered by hexagonal prisms with aspect ratios $\varepsilon = 1/3, 1/2, 1, 2, 3$, and real parts of refractive index of $n = 1.3, 1.5, 2.0, 2.5, 3.0$, and sizes such that $\rho' = 5, 10, 30, 100, 300, 1000$ in every possible combination of $\varepsilon, n,$ and ρ'. (b) The Rayleigh normalized scattering by hexagonal prisms in the forward direction for all curves shown in (a), and with the addition of $\rho' = 0.1, 0.2, 0.5, 1, 2$. In (b) the color of the point represents the relative refractive index and the point shape represents the aspect ratio.

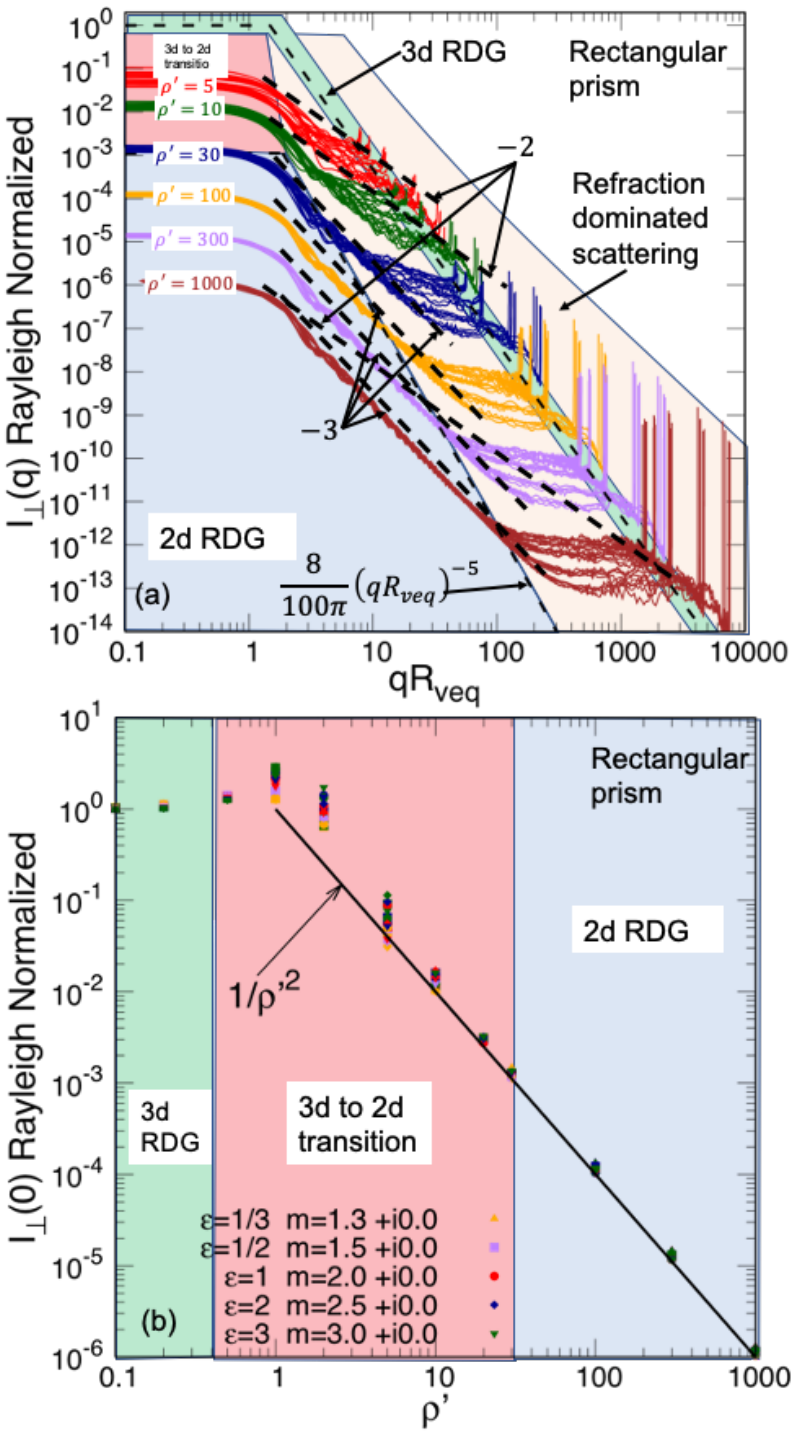

Fig. 4.4 (a) The Rayleigh normalized light scattered by rectangular prisms with $\varepsilon = 1/3, 1/2, 1, 2, 3$, and real parts of refractive index of $n = 1.3, 1.5, 2.0, 2.5, 3.0$, and sizes such that $\rho' = 5, 10, 30, 100, 300, 1000$ in every possible combination of $\varepsilon, n,$ and ρ'. (b) The Rayleigh normalized scattering by rectangular prisms in the forward direction for all curves shown in (a), and with the addition of $\rho' = 0.1, 0.2, 0.5, 1, 2$. In (b) the color of the point represents the relative refractive index and the point shape represents the aspect ratio.

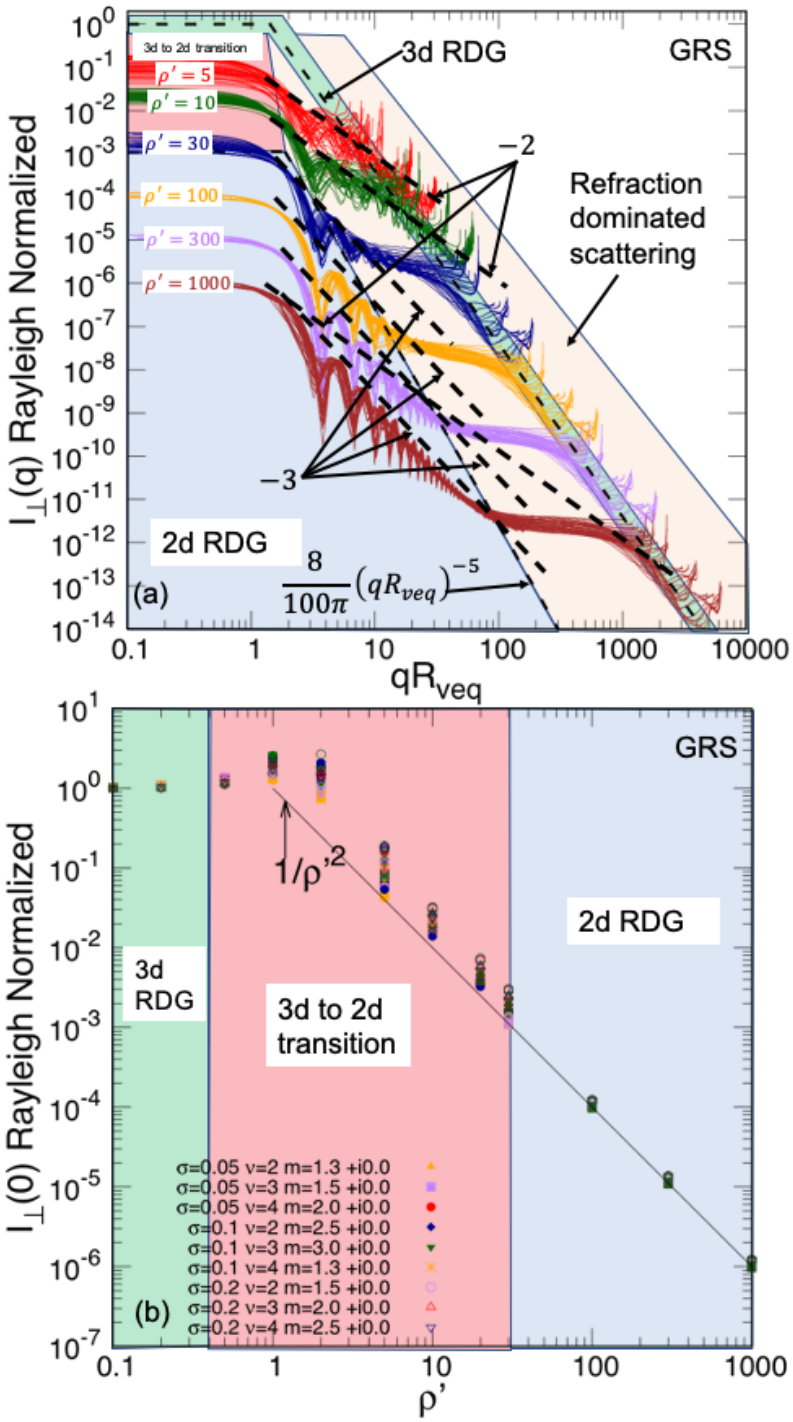

Fig. 4.5 (a) The Rayleigh normalized light scattered by GRS with $\sigma = 0.05, 0.1, 0.2$, $\nu = 2, 3, 4$, and real parts of refractive index of $n = 1.3, 1.5, 2.0, 2.5, 3.0$, and sizes such that $\rho' = 5, 10, 30, 100, 300, 1000$ in every possible combination of $\sigma,\ \nu,\ n,$ and ρ'. (b) The Rayleigh normalized scattering by GRS in the forward direction for all curves shown in (a), and with the addition of $\rho' = 0.1, 0.2, 0.5, 1, 2$. In (b) the color of the point represents the relative refractive index and the point shape represents the different combination of σ, and ν.

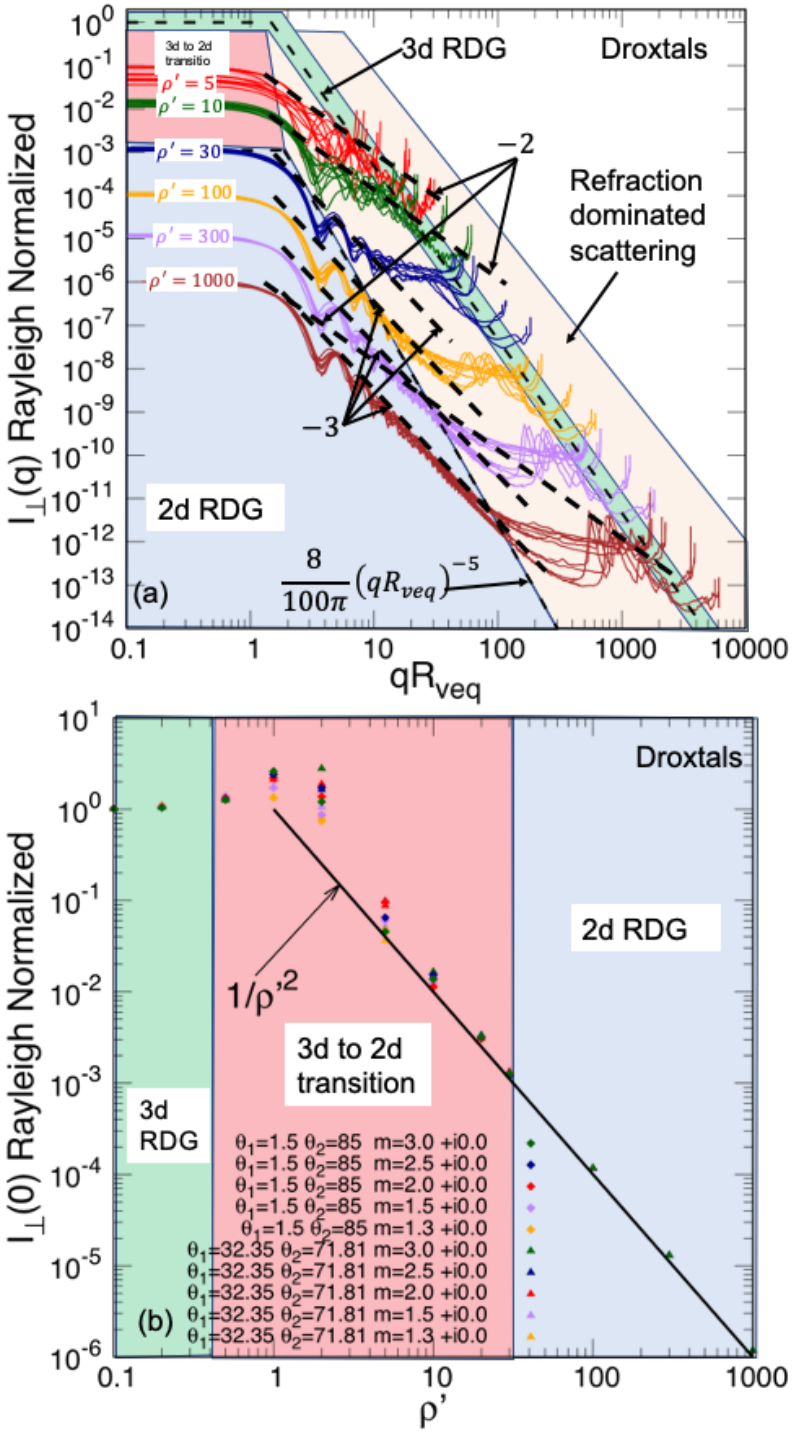

Fig. 4.6 The Rayleigh normalized light scattered by droxtals with $\theta_1 = 32.35°$,$\theta_2 = 71.81°$ and $\theta_1 = 1.5°$,$\theta_2 = 85°$ and real parts of refractive index of $n = 1.3, 1.5, 2.0, 2.5, 3.0$, and sizes such that $\rho' = 5, 10, 30, 100, 300, 1000$ in every possible combination of n, and ρ' with the two pairs of angles. (b) The Rayleigh normalized scattering by the same droxtals in the forward direction for all curves shown in (a), and with the addition of $\rho' = 0.1, 0.2, 0.5, 1, 2$.

has fallen below unity and is approaching $1/\rho'^2$ as ρ' increases. By $\rho' = 10$ the Rayleigh normalized forward scattering is approximately going as $1/\rho'^2$, with in a factor of about 2 and

$$I_{\perp,RN}(qR_{veq} < 1) \sim 1/\rho'^2. \qquad 10 < \rho' < 30 \tag{4.11}$$

As qR_{veq} increases away from the forward scattering directions, the scattering passes through the Guinier regime and enters the power law regime. The power law regime when the forward scattering is in the 2d to 3d region is dominated by refractive effects and there are a lot of bumps and wiggles with no clear description yet. This is similar to what was seen with spheres, a rough quasi power-law of -2 remains over the group of curves, after which there is the enhanced backscattering in the back directions.

Once $30 \leq \rho'$, the Rayleigh normalized scattering in the forward direction has primarily settled down and started to go as $1/\rho'^2$ for all of the many variations being considered. This can be seen in both Fig. 4.1(a)-Fig. 4.6 (a), and Fig. 4.1(b)-Fig. 4.6 (b), though it should be noted that the GRS seems to take a bit longer than the other shapes. The Rayleigh normalized scattering has entered the 2d RDG region, and when $qR_{veq} < 1$,

$$I_{\perp,RN}(qR_{veq} < 1) = 1/\rho'^2. \qquad 30 \lesssim \rho' \tag{4.12}$$

As qR_{veq} increases away from the forward scattering directions the scattering passes through the Guinier regime and enters the power law regime. In the power law regime, the scattering follows a power law of -3, this is caused by the 2d diffraction of the 2d projection of the particle. The scattering follows the power law of -3 up until $qR_{veq} \sim \frac{\rho'}{10}$, and so

$$I_{\perp,RN}\left(1 \lesssim qR \lesssim \frac{\rho'}{10}\right) \propto (qR)^{-3}. \qquad 30 \leq \rho' \tag{4.13}$$

After $qR_{veq} \sim \frac{\rho'}{10}$, the scattering enters the refraction dominated region, which is separated from the 2d RDG region along the line denoted by $8/100\pi(qR_{veq})^{-5}$. As might be expected, it is in

this region that most of the uniqueness in the scattering is found. There is not a clear refraction hump as was seen with spheres for all of the shapes, and variations being considered in Fig. 4.1-Fig. 4.6, but there remains a tangential quasi power law of -2 between the Guinier regime and where the scattering meets back up with the 3d RDG line. The refraction dominated region ends as qR_{veq} approaches $2kR_{veq}$, and almost all of the scattering from the shapes and variations being considered show enhanced backscattering. Though most of the scattering shows enhanced backscattering there is a wide range in the magnitude of the enhancement.

Although the focus of this work is on the similarities in the scattering and putting together an overall picture of how particles scatter light in general, it would be negligent not to make comments on some of the uniqueness in the light scattering. The differences in the scattering in the refraction dominated region come from two main sources. First, a lack of symmetry. Consider a sphere, for example. Each orientation of a sphere is exactly the same as any other and so the behavior of the scattering is very similar for all spheres. On the other hand, if we consider a cube, although there are many symmetries in a cube not every orientation is identical, and each distinct orientation will lead to distinct refractive behavior in the scattering. The second source is the variation in the real part of the index of refraction, this can be understood by considering spheres, which have distinct refractive effects such as the rainbows and glories that are directly affected by the real part of the refractive index, even though there is only a single orientation. Varying the real part of the refractive index gives rise to even more distinction in the scattering within the refraction dominated region. The combination of a changing refractive index and the many unique orientations of non-spherical shapes lead to the uniqueness seen in the light scattering in the refraction dominated regions.

One of the most notable of the unique refraction effects can be seen in the light scattered by hexagonal columns with a real part of the refractive index $n = 1.3$, shown in Fig. 4.3(a). It can be seen in Fig. 4.7 that some of the curves with $\rho' = 30, 100, 300, and\ 1000$ have a triangular spike in the scattering around $qR_{veq} \sim \rho'$. Less noticeable is a second triangular peak shortly after the first, these are referred to as "sun dogs" [69,70] and are formed by ice crystals at a scattering angle of $\theta \sim 20°$ away from the sun, this is when $q \sim 3.5(\mu m^{-1})$.

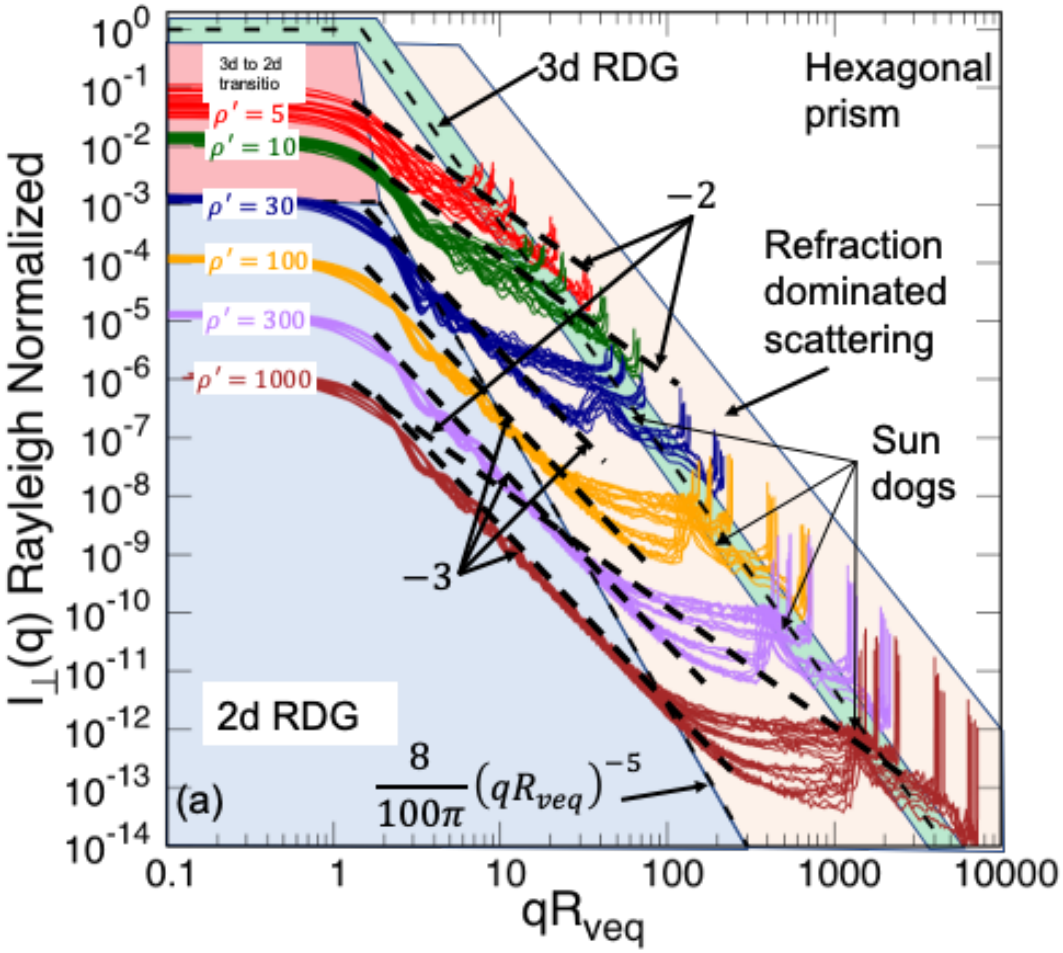

Fig. 4.7 Same as Fig. 4.3(a) expect with the triangular "Sun dogs" indicated.

There are similar formations that can be seen in the light scattered by droxtals in Fig. 4.6. The GRS demonstrate a wide variety of behavior in the refraction dominated region, when they are

nearly spherical, they have a strong refraction hump, and a large enhanced backscattering peak. As the GRS become less spherical, there are no symmetries left and each orientation is unique, this washes out much of the refraction effects, and the refraction hump as well as the enhanced backscattering are diminished.

4.4 Effects of absorption

Just as with spheres when there is a non-zero imaginary part of the refractive index, and $\kappa kR_{veq} \gtrsim 0.1$ the scattering will be affected. Fig. 4.8(a) shows the scattering by a hexagonal column with $\rho' = 1000$, an aspect ratio $\varepsilon = 1$, size parameter $kR_{veq} \approx 3160$ and relative index of refraction $m = 1.3 + i\kappa$, with κ values such that $\kappa kR_{veq} = 0.0, 0.1, 0.3, 1.0, 3.0$. It can be seen in Fig. 4.8(a) that just as with spheres as κkR_{veq} increases there is systematic reduction in the refractive effects, most notably the disappearance of the sun dogs by $\kappa kR_{veq} = 3$, and the reduction in the enhanced backscattering. Fig. 4.8(b) is similar to Fig. 4.8(a) but with rectangular columns, and a size parameter of $kR_{veq} \approx 3300$, again the systematic reduction in refraction effects can be seen.

Fig. 4.9(a) shows GRS with $\sigma = 2, \nu = 4$, with a $\rho' = 1000$, size parameter $kR_{veq} \approx 1060$ and relative index of refraction $m = 2.0 + i\kappa$, with κ values such that $\kappa kR_{veq} = 0.0, 0.1, 0.3, 1.0, 3.0$. Fig. 4.9(b) shows the light scattered by cylinders with a $\rho' = 30$, a size parameter $kR_{veq} \approx 33.7$ and relative index of refraction $m = 2.0 + i\kappa$, with κ values such that $\kappa kR_{veq} = 0.0, 0.1, 0.3, 1.0, 3.0$. In Fig. 4.9(a) and Fig. 4.9(b) it can be seen that as κkR_{veq} increases the refraction effects in the refraction dominated region are systematically reduced with κkR_{veq}. Finally, Fig. 4.10 shows the light scattered by droxtals with a $\rho' = 1000$, a size parameter $kR_{veq} \approx 3300$ and relative index of refraction $m = 1.3 + i\kappa$, with κ values such that

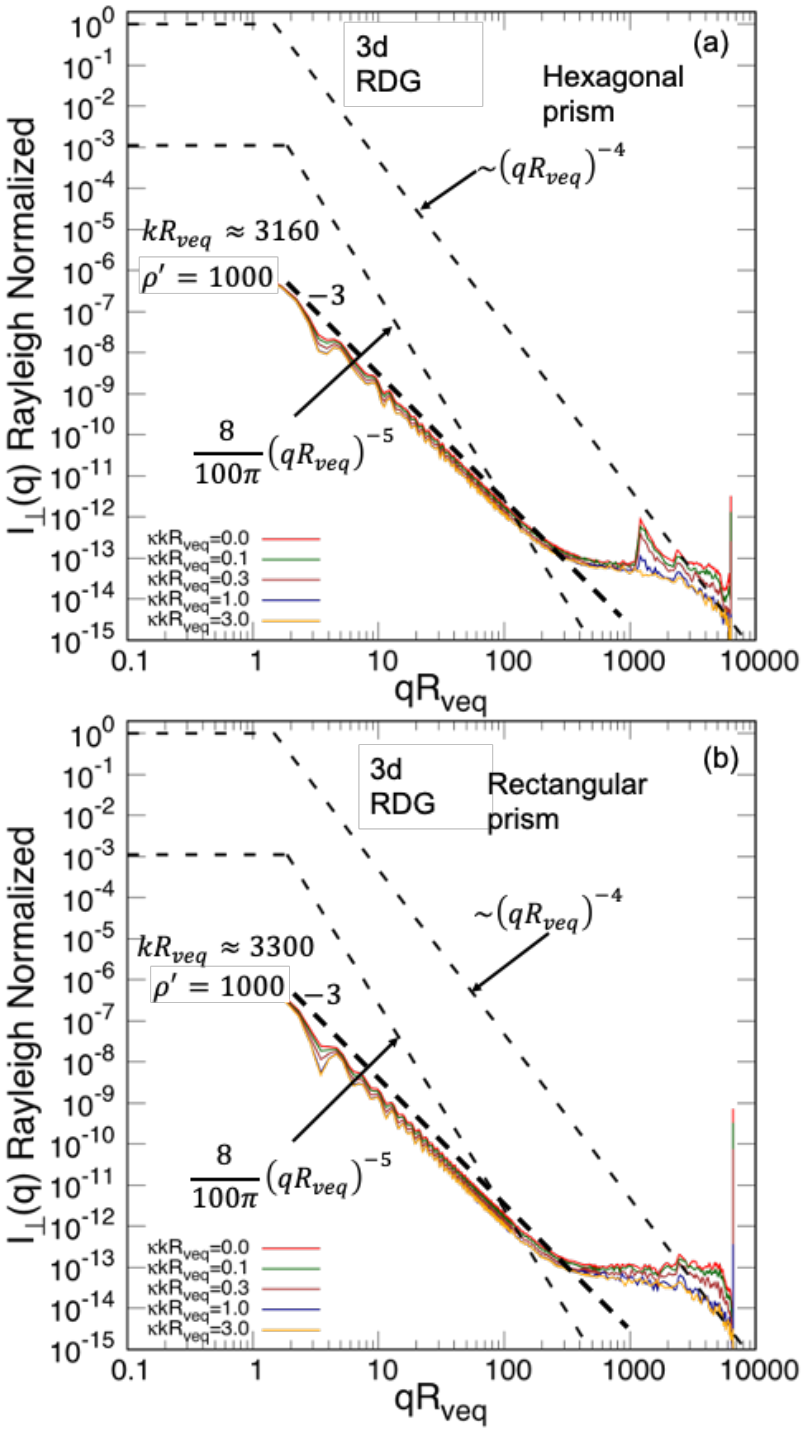

Fig. 4.8 (a) The Rayleigh normalized light scattered by hexagonal prisms with a size parameter $kR_{veq} \approx 3160$, and a relative refractive index of $m = 1.3 + i\kappa$. The imaginary part of the refractive index is set such that $\kappa kR_{veq} = 0.0, 0.1, 0.3, 1.0, 3.0$. (b) The Rayleigh normalized light scattered by hexagonal prisms with a size parameter $kR_{veq} \approx 3300$, and a relative refractive index of $m = 1.3 + i\kappa$. The imaginary part of the refractive index is set such that $\kappa kR_{veq} = 0.0, 0.1, 0.3, 1.0, 3.0$.

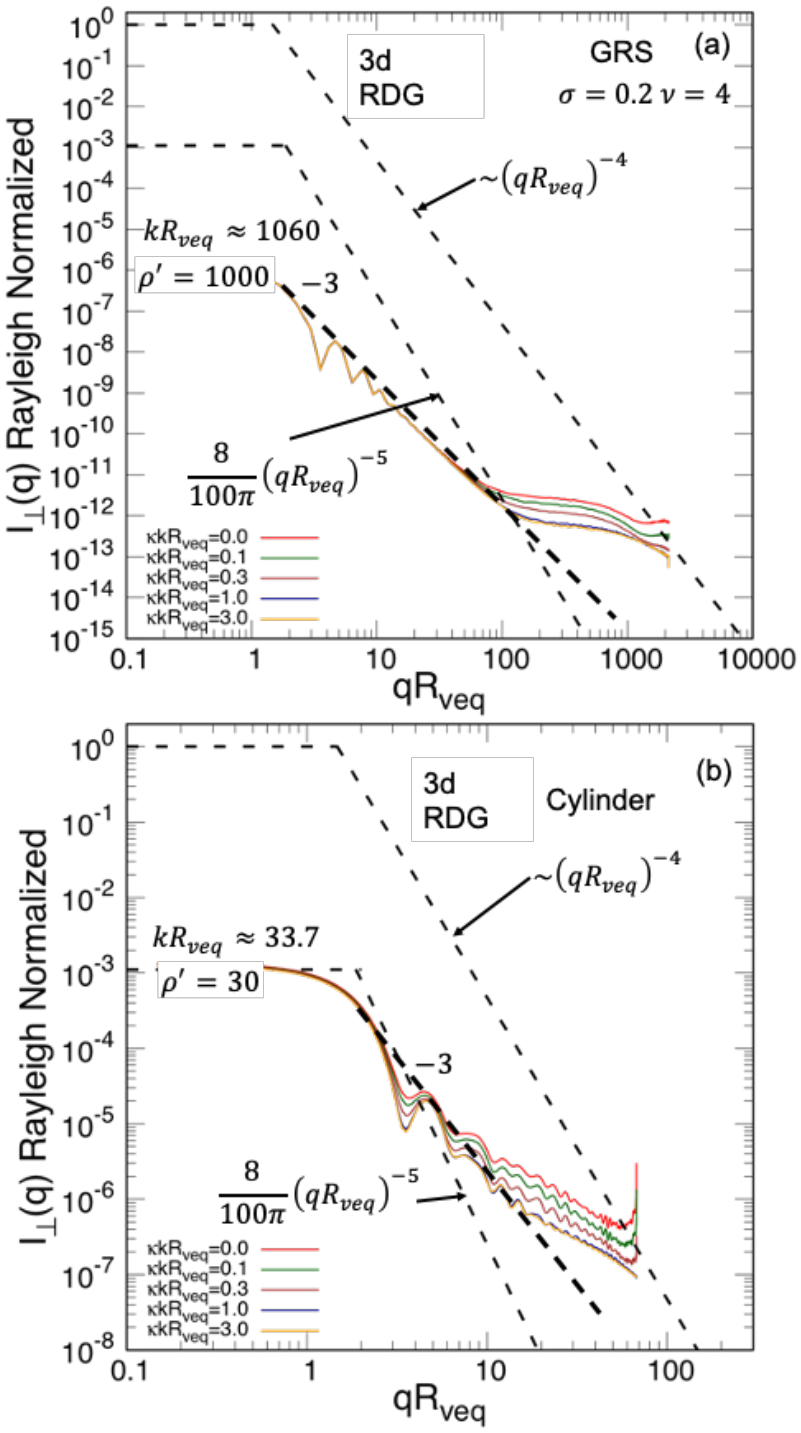

Fig. 4.9 The Rayleigh normalized light scattered by GRS with a size parameter $kR_{veq} \approx 1060$, and a relative refractive index of $m = 2.0 + i\kappa$. The imaginary part of the refractive index is set such that $\kappa kR_{veq} = 0.0, 0.1, 0.3, 1.0, 3.0$. (b) The Rayleigh normalized light scattered by cylinders with a size parameter $kR_{veq} \approx 33.7$, and a relative refractive index of $m = 1.3 + i\kappa$. The imaginary part of the refractive index is set such that $\kappa kR_{veq} = 0.0, 0.1, 0.3, 1.0, 3.0$.

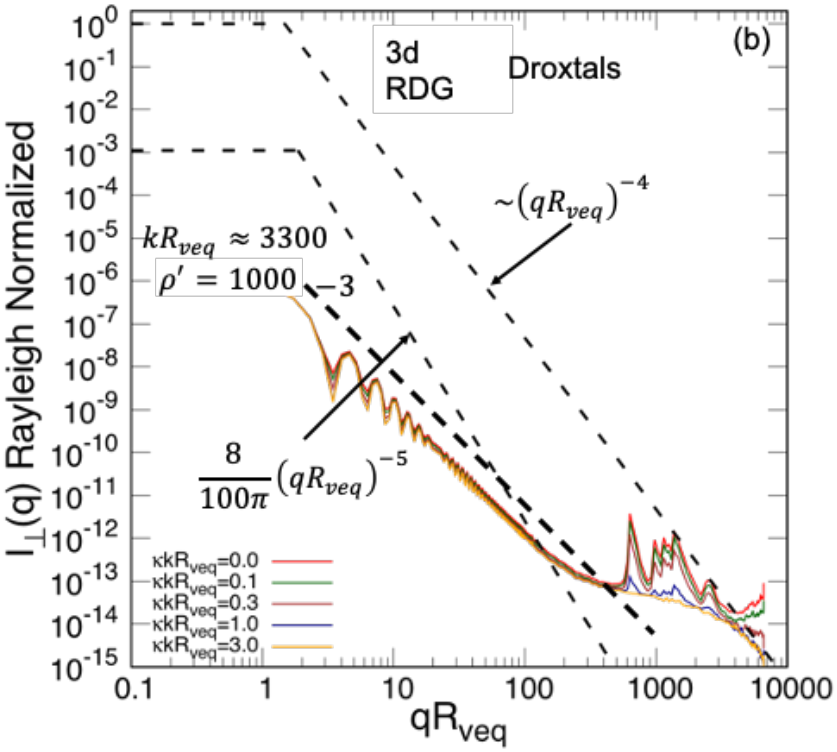

Fig. 4.10 The Rayleigh normalized light scattered by droxtals with a size parameter $kR_{veq} \approx 3300$, and a relative refractive index of $m = 1.3 + i\kappa$. The imaginary part of the refractive index is set such that $\kappa kR_{veq} = 0.0, 0.1, 0.3, 1.0, 3.0$.

$\kappa kR_{veq} = 0.0, 0.1, 0.3, 1.0, 3.0$. As with all the previous shapes, κkR_{veq} describes the reduction in the refraction effects. As should be expected, absorption effects the refraction effects of the scattered light while leaving the diffraction and reflection components, and κkR_{veq} provides a single parameter to describe how much the refraction effects have been reduced.

4.5 Aggregates

As a final demonstration of the quasi-universality of ρ', and particularly how ρ' describes which region the light scattered by a particle is in, we will compare fractal and 3d aggregates. The light scattered by fractal aggregates has been described in the past by what is called the Rayleigh-Debye-Gans fractal aggregate (RDGFA) theory, which was reviewed in [24] and more

recently in [71]. One of the most predominate uses of fractal aggregates is to model the light scattered by soot; [24,71] list extensive references to some of the large body of work with fractals aggregates being used in this manner. Typically, the refractive index of the monomers is such the condition for RDG scattering is not met i.e. $|m-1|$ is close to unity. However, the monomers are usually much smaller than the wavelength of light and thus the condition, so they are Rayleigh scatterers. As more monomers are added to the aggregate eventually the aggregate as a whole will no longer be a Rayleigh scatterer, and yet RDGFA theory has still been found to be applicable [71]. It will be demonstrated in the following that due to the fractal nature of the aggregates, the internal coupling parameter of the aggregate describes the aggregate as being within 3d RDG regime as a monomer and remaining within the 3d RDG regime as more monomers are added.

We must now discus what happens to ρ' as more monomers are added to the aggregate. Consider the ratio of the volume to the projected area in the definition of ρ' given by Eq. (4.3). Each time a monomer is added to the aggregate the volume will increase by the volume of a monomer, but how the projected area increases depends on the dimension of the aggregate. For DLCA fractal aggregates the projected area has been found through transmission electron microscopy (TEM) and mobility considerations to be given by [72–76]

$$A = N^{0.92} A_{mon}, \tag{4.14}$$

where $A_{mon} = \pi a^2$ is the projected area of a single monomer. Because the projected area A of the fractal aggregate grows nearly proportional to N, and the volume V grows at a rate directly proportional to N the ratio of the volume and the projected area V/A changes very little. Eq. (4.14) can be used to approximate the internal coupling parameter for a fractal aggregate ρ'_{frac}, in terms of the internal coupling parameter for a single monomer ρ'_{mon}

$$\rho'_{frac} = N^{0.08}\rho'_{mon}. \tag{4.15}$$

Eq. (4.15) tells us that as each monomer is added there is very little change in ρ'_{frac}, and so if the monomers are Rayleigh scatterers the aggregate will be as well.

On the other hand, consider a 3d aggregate made up of monomers placed on a cubic lattice. The first monomer is placed at the origin and then one of the six nearest neighbor sites is randomly selected and filled. After that, another one of the nearest neighbor sites of all of the monomers is randomly selected and filled, this continues until a desired number of monomers has been added. In this case there will be a large amount of shadowing of monomers by other monomers as the aggregate grows. The shadowing of monomers by other monomers will cause V to grow at a greater rate than A and so the ratio V/A will grow much faster than it does for fractal aggregates. The "shading" of particles by other particles, and the effects this has on the scattering in the forward direction, is discussed in terms of multiple-scattering by Mishchenko et al [77], and as will be shown is inherently built into the definition of the internal coupling parameter.

Fig. 4.11 shows ρ'_{frac} vs N for fractal aggregates with $k_o = 1.35$, $D_f = 1.8$, and $a = 20nm$. ρ'_{frac} has been calculated using Eq. (4.3), and also using Eq. (4.15). Also, in Fig. 4.11 ρ'_{3d} vs N for 3d aggregates calculated by the techniques of section 4.1 is shown. In Fig. 4.11 it can be seen that the calculated values of ρ'_{frac} compares well with Eq. (4.15). Also, in Fig. 4.11 it can be seen that the ρ'_{frac} with a refractive index of $m = 1.6 + i0.6$ has only increased to $\rho'_{frac} \approx 0.34$ by N=1000, while the 3d aggregate has reached $\rho'_{3d} \approx 0.95$. The non-absorbing case $m = 1.5 + i0.0$, has a similar behavior with, $\rho'_{frac} \approx 0.2$ by N=1000, while the 3d aggregate has reached $\rho'_{3d} \approx 0.57$. Also, it should be noted in Fig. 4.11 the curves for the fractal aggregates have almost leveled off, when the curves for the 3d aggregates are still increasing at a

significant rate. Using Eq. (4.15) to estimate, a fractal aggregate with an index of $m = 1.6 + i0.6$, and a monomer size of 20nm would have to have ~5 hundred million monomers to reach a $\rho'_{frac} \approx 1$.

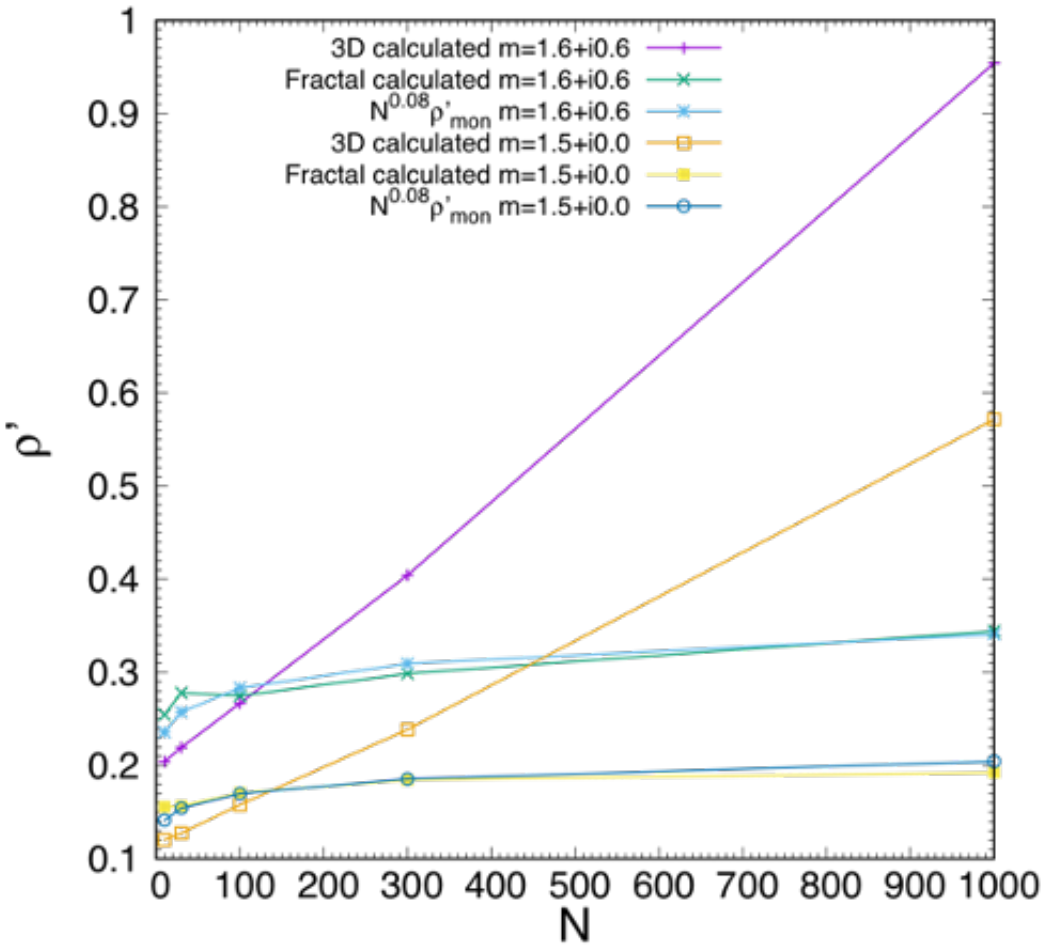

Fig. 4.11 The internal coupling parameter ρ'vs the number of monomer in the aggregate N. Plotted are the results calculated using Eq. (4.3) for fractal aggregates with $k_o = 1.35, D_f = 1.8$, and 3d aggregates with indexes of refraction $m = 1.6 + i0.6$, $1.5 + i0.0$, also shown is the result using Eq. (4.15).

Fig. 4.12 shows the Rayleigh normalized scattering from fractal aggregates and 3d aggregates. The light scattering curves for the fractal aggregates which have $\rho'_{frac} < 0.34$ behave similarly despite having an increasing number of monomers. Because the ρ'_{frac} is

barely changing, the curves for the 3d aggregates show a significant amount of change as ρ'_{3d} approaches unity and the scattering leaves the 3d RDG region and begins to enter the 3d to 2d transition region. This demonstrates the effectiveness of the internal coupling parameter at determining what region the light scattering is in and reiterates the universality of the internal coupling parameter.

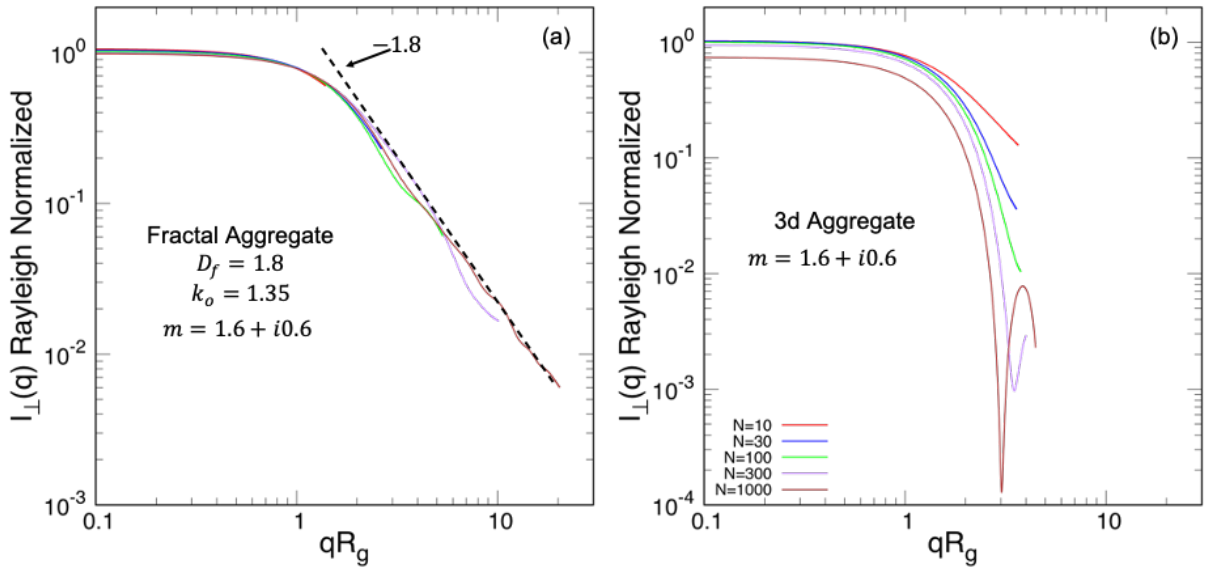

Fig. 4.12 (a) The Rayleigh normalized light scattered by fractal aggregates with $k_o = 1.35, D_f = 1.8$, and $m = 1.6 + i0.6$. (b) The Rayleigh normalized light scattered by 3d aggregates with $m = 1.6 + i0.6$.

Chapter 5 - Conclusions and Future work

When the Rayleigh normalized scattering from any three dimensional particle, no matter the shape, size, aspect ratio, relative index of refraction, or fractal dimension, is plotted vs qR_{veq} the same behaviors are found with the internal coupling parameter ρ'. When $\rho' \lesssim 0.3$, the scattering is in the 3d RDG limit, there will be the forward scattering that goes as unity, followed by the Guinier regime at $qR_{veq} \sim 1$. After the Guinier regime, the scattering enters the power law regimes and follow Porod's law that states the scattering will follow a power law of -$(2D_m - D_s)$. When $0.3 \lesssim \rho' \lesssim 3$ the scattering has begun to leave the 3d RDG limit and transition toward the 2d RDG, the Rayleigh normalized scattering in the forward direction increases above unity in this range of ρ'. The scattering still passes through the Guinier regime at $qR_{veq} \sim 1$, and then enters the power law regime. In the power law regime at this range of ρ' values, the scattering is dominated by refraction, but the ripples do begin to develop a quasi power law of -2 until qR_{veq} begins to approach $2kR_{veq}$, when there is a spike in the scattering referred to as the enhanced backscattering.

When $3 \lesssim \rho' < 30$, the scattering is in the 3d to 2d transition region, the Rayleigh normalized scattering in the forward direction has fluctuations, but has started to settle down to going toward following $1/\rho'^2$. The scattering passes through the Guinier regime and then the envelope of the ripples of the scattering follow a quasi-power law of -2 in the refraction dominated region, until reaching the enhanced backscattering. Finally, once $\rho' \gtrsim 30$ the Rayleigh normalized forward scattering has settled down and goes as $1/\rho'^2$. After the Guinier regime, the scattering enters the power law regime and goes as $\left(qR_{veq}\right)^{-3}$. The power law of -3 comes from the 2d diffraction of the projected area of the 3d particle, the power law remains

until $qR_{veq} \sim \rho'/10$ when the scattering enters the refraction dominated region. When $\rho' \gtrsim 30$ the 2d RDG region and the refraction dominated region are separated by the line denoted by $8/100\pi\left(qR_{veq}\right)^{-5}$.

In the refraction dominated region when $\rho' \gtrsim 30$, there is a large amount of variation in the behavior of the scattering depending on the shape and refractive index. However, all of the scattering in the refraction dominated area is greatly affected by absorption, and the parameter κkR_{veq} provides a universal parameter that describes the reduction in the refraction effects. When $\kappa kR_{veq} < 0.1$, there is little to no effect on the scattering, but as κkR_{veq} approaches 0.1 the reduction in the scattering becomes clearly visible. As $\kappa kR_{veq} \sim 1$, the skin depth is comparable to the size of the particle and almost all of the refraction effects are gone, and certainly once $\kappa kR_{veq} = 3$, they are almost all gone and only the diffraction and reflection component of the scattering remains.

A future goal would be to reach larger ρ' values for spheroids and cylinders, either by the use/development of different numerical programs or access to more computational resources. Also, there is much work that can be done with regards to both ρ' and κkR_{veq}. All of the scattering in this work was orientationally averaged, but what about single fixed orientations? Will the same formulations and concepts work with single fixed orientations, or is there some aspect to the orientational averaging that allows ρ' to work? With κkR_{veq}, how well does κkR_{veq} work for particles with extreme aspect ratios and what would the definition of κkR_{veq} be in the case of extreme aspect ratios?

References

[1] Strutt HJW. XXXVI. On the light from the sky, its polarization and colour. The London, Edinburgh, and Dublin Philosophical Magazine and Journal of Science 1871;41:274–9. https://doi.org/10.1080/14786447108640479.

[2] Mie G. Beiträge zur Optik trüber Medien, speziell kolloidaler Metallösungen. Annalen Der Physik 1908;330:377–445. https://doi.org/10.1002/andp.19083300302.

[3] Hulst HC van de. Light Scattering by Small Particles. Corrected Edition edition. New York: Dover Publications; 1981.

[4] Bohren CF, Huffman DR. Absorption and Scattering of Light. New edition edition. Weinheim: W.V.; 1998.

[5] Mishchenko MI, Hovenier JW, Travis LD. Light Scattering by Nonspherical Particles: Theory, Measurements, and Applications. Elsevier; 1999.

[6] Mishchenko MI, Travis LD, Lacis AA. Multiple Scattering of Light by Particles: Radiative Transfer and Coherent Backscattering. Cambridge University Press; 2006.

[7] Mishchenko MI. Electromagnetic Scattering by Particles and Particle Groups: An Introduction. Cambridge University Press; 2014.

[8] Guinier A. Small-angle Scattering of X-rays [by] André Guinier [and] Gérard Fournet: Translation by Christopher B. Walker; Followed by a Biibliography by Kenneth L. Yudowitch. Wiley; 1955.

[9] Kratky O, Porod G. Röntgenuntersuchung gelöster Fadenmoleküle. Recueil Des Travaux Chimiques Des Pays-Bas 1949;68:1106–22. https://doi.org/10.1002/recl.19490681203.

[10] Feigin LA, Svergun DI. Structure Analysis by Small-Angle X-Ray and Neutron Scattering. Springer US; 1987.

[11] Heinson WR, Chakrabarti A, Sorensen CM. A new parameter to describe light scattering by an arbitrary sphere. Optics Communications 2015;356:612–5. https://doi.org/10.1016/j.optcom.2015.08.067.

[12] Heinson YW, Maughan JB, Heinson WR, Chakrabarti A, Sorensen CM. Light scattering Q-space analysis of irregularly shaped particles. J Geophys Res-Atmos 2016;121:682–91. https://doi.org/10.1002/2015JD024171.

[13] Heinson YW, Maughan JB, Ding J, Chakrabarti A, Yang P, Sorensen CM. Q-space analysis of light scattering by ice crystals. J Quant Spectrosc Radiat Transf 2016;185:86–94. https://doi.org/10.1016/j.jqsrt.2016.08.021.

[14] Sorensen CM, Heinson YW, Heinson WR, Maughan JB, Chakrabarti A. Q-Space Analysis of the Light Scattering Phase Function of Particles with Any Shape. Atmosphere 2017;8:68. https://doi.org/10.3390/atmos8040068.

[15] Gautam P, Maughan JB, Ilavsky J, Sorensen CM. Light scattering study of highly absorptive, non-fractal, hematite aggregates. J Quant Spectrosc Radiat Transf 2020;246:UNSP 106919. https://doi.org/10.1016/j.jqsrt.2020.106919.

[16] Multiple Scattering of Light by Particles: Radiative Transfer and Coherent Backscattering. Cambridge ; New York: Cambridge University Press; 2006.

[17] Taylor JR. Classical Mechanics. University Science Books; 2005.

[18] Eugene. Hecht. Optics. 4th edition.. Reading, Mass.: Addison-Wesley; 2002.

[19] Pedrotti FL, Pedrotti LM, Pedrotti LS. Introduction to Optics. 3 edition. Upper Saddle River, N.J: Pearson; 2006.

[20] Jackson JD. Classical Electrodynamics Third Edition. 3 edition. New York: Wiley; 1998.
[21] Arfken GB, Weber HJ. Mathematical Methods for Physicists, 6th Edition. 6th edition. Boston: Academic Press; 2005.
[22] Stokes GG. On the Composition and Resolution of Streams of Polarized Light from different Sources. Transactions of the Cambridge Philosophical Society 1851;9:399.
[23] Sorensen CM. Q-space analysis of scattering by particles: A review. Journal of Quantitative Spectroscopy and Radiative Transfer 2013;131:3–12. https://doi.org/10.1016/j.jqsrt.2012.12.029.
[24] Sorensen CM. Light Scattering by Fractal Aggregates: A Review. Aerosol Science and Technology 2001;35:648–87. https://doi.org/10.1080/02786820117868.
[25] Hecht E. Optics, 2nd Edition. 2nd edition. Reading, Mass: Addison-Wesley; 1987.
[26] Sorensen CM, Shi D. Guinier analysis for homogeneous dielectric spheres of arbitrary size. Optics Communications 2000;178:31–6. https://doi.org/10.1016/S0030-4018(00)00601-5.
[27] Martin JE, Hurd AJ. Scattering from fractals. Journal of Applied Crystallography 1987;20:61–78. https://doi.org/10.1107/S0021889887087107.
[28] Ping Yang, Liou KN. Single-scattering properties of complex ice crystals in terrestrial atmosphere. Contrib Atmos Phys 1998;71:223–48.
[29] Yang P, Gao B-C, Baum BA, Hu YX, Wiscombe WJ, Mishchenko MI, et al. Asymptotic solutions for optical properties of large particles with strong absorption. Appl Opt, AO 2001;40:1532–47. https://doi.org/10.1364/AO.40.001532.
[30] Born M, Wolf E. Principles of Optics. 5th ed. Pergamon Press; 1975.
[31] Mishchenko MI, Hovenier JW, Travis LD. Light Scattering by Nonspherical Particles: Theory, Measurements, and Applications. Elsevier; 1999.
[32] Oh C, Sorensen CM. Scaling Approach for the Structure Factor of a Generalized System of Scatterers. Journal of Nanoparticle Research 1999;1:369–77. https://doi.org/10.1023/A:1010033111039.
[33] Maughan JB, Sorensen CM. Application of the scaling approach to particles having simple, fundamental shapes, in the Rayleigh-Debye-Gans diffraction limit. J Quant Spectrosc Radiat Transf 2019;222:190–5. https://doi.org/10.1016/j.jqsrt.2018.10.037.
[34] Yang P, Baum BA, Heymsfield AJ, Hu YX, Huang H-L, Tsay S-C, et al. Single-scattering properties of droxtals. Journal of Quantitative Spectroscopy and Radiative Transfer 2003;79–80:1159–69. https://doi.org/10.1016/S0022-4073(02)00347-3.
[35] Muinonen K, Nousiainen T, Lindqvist H, Munoz O, Videen G. Light scattering by Gaussian particles with internal inclusions and roughened surfaces using ray optics. J Quant Spectrosc Radiat Transf 2009;110:1628–39. https://doi.org/10.1016/j.jqsrt.2009.03.012.
[36] Huang H, Oh C, Sorensen CM. Structure factor scaling in aggregating systems. Phys Rev E 1998;57:875–80. https://doi.org/10.1103/PhysRevE.57.875.
[37] Richardson LF. The problem of contiguity : An appendix to statistics of deadly quarrels. General Systems Yearbook 1961;6:139–87. https://cds.cern.ch/record/434833 (accessed September 27, 2020).
[38] Mandelbrot BB. The Fractal Geometry of Nature. Henry Holt and Company; 1983.
[39] Heinson WR, Sorensen CM, Chakrabarti A. A three parameter description of the structure of diffusion limited cluster fractal aggregates. Journal of Colloid and Interface Science 2012;375:65–9. https://doi.org/10.1016/j.jcis.2012.01.062.
[40] Sorensen CM, Roberts GC. The prefactor of fractal aggregates. J Colloid Interface Sci 1997;186:447–52. https://doi.org/10.1006/jcis.1996.4664.

[41] Lattuada M, Wu H, Morbidelli M. Hydrodynamic radius of fractal clusters. Journal of Colloid and Interface Science 2003;268:96–105. https://doi.org/10.1016/j.jcis.2003.07.028.
[42] Meakin P. Formation of Fractal Clusters and Networks by Irreversible Diffusion-Limited Aggregation. Phys Rev Lett 1983;51:1119–22. https://doi.org/10.1103/PhysRevLett.51.1119.
[43] Kolb M, Botet R, Jullien R. Scaling of Kinetically Growing Clusters. Phys Rev Lett 1983;51:1123–6. https://doi.org/10.1103/PhysRevLett.51.1123.
[44] Fry D, Chakrabarti A, Kim W, Sorensen C. Structural crossover in dense irreversibly aggregating particulate systems. Phys Rev E 2004;69:061401. https://doi.org/10.1103/PhysRevE.69.061401.
[45] Kerker M. The Scattering of Light and Other Electromagnetic Radiation: Physical Chemistry: A Series of Monographs. Academic Press; 2016.
[46] van de Hulst HC. Light Scattering by Small Particles. 1957.
[47] Heinson WR, Chakrabarti A, Sorensen CM. Crossover from spherical particle Mie scattering to circular aperture diffraction. J Opt Soc Am A-Opt Image Sci Vis 2014;31:2362–4. https://doi.org/10.1364/JOSAA.31.002362.
[48] Sorensen CM. Q-space analysis of scattering by particles: A review. Journal of Quantitative Spectroscopy and Radiative Transfer 2013;131:3–12. https://doi.org/10.1016/j.jqsrt.2012.12.029.
[49] Maughan JB, Sorensen CM. Universal parameter to describe the reduction of refraction effects in the scattering of absorbing spheres. J Opt Soc Am A, JOSAA 2020;37:1456–64. https://doi.org/10.1364/JOSAA.394401.
[50] Heinson YW, Maughan JB, Ding J, Chakrabarti A, Yang P, Sorensen CM. Q-space analysis of light scattering by ice crystals. J Quant Spectrosc Radiat Transf 2016;185:86–94. https://doi.org/10.1016/j.jqsrt.2016.08.021.
[51] Sorensen CM, Fischbach DJ. Patterns in Mie scattering. Optics Communications 2000;173:145–53. https://doi.org/10.1016/S0030-4018(99)00624-0.
[52] Berg MJ, Sorensen CM, Chakrabarti A. Patterns in Mie scattering: evolution when normalized by the Rayleigh cross section. Appl Opt, AO 2005;44:7487–93. https://doi.org/10.1364/AO.44.007487.
[53] Wang G, Chakrabarti A, Sorensen CM. Effect of the imaginary part of the refractive index on light scattering by spheres. J Opt Soc Am A, JOSAA 2015;32:1231–5. https://doi.org/10.1364/JOSAA.32.001231.
[54] Sorensen CM, Maughan JB, Moosmueller H. Spherical particle absorption over a broad range of imaginary refractive index. J Quant Spectrosc Radiat Transf 2019;226:81–6. https://doi.org/10.1016/j.jqsrt.2019.01.011.
[55] Yang P, Gao B-C, Baum BA, Hu YX, Wiscombe WJ, Mishchenko MI, et al. Asymptotic solutions for optical properties of large particles with strong absorption. Appl Opt, AO 2001;40:1532–47. https://doi.org/10.1364/AO.40.001532.
[56] Laven P. Simulation of rainbows, coronas and glories using Mie theory and the Debye series. Journal of Quantitative Spectroscopy and Radiative Transfer 2004;89:257–69. https://doi.org/10.1016/j.jqsrt.2004.05.026.
[57] Heffernan BM, Heinson YW, Maughan JB, Chakrabarti A, Sorensen CM. Backscattering measurements of micron-sized spherical particles. Appl Optics 2016;55:3214–8. https://doi.org/10.1364/AO.55.003214.

[58] Laven P. How are glories formed? Appl Opt, AO 2005;44:5675–83. https://doi.org/10.1364/AO.44.005675.
[59] Nussenzveig HM. Complex angular momentum theory of the rainbow and the glory. J Opt Soc Am, JOSA 1979;69:1068–79. https://doi.org/10.1364/JOSA.69.001068.
[60] Nussenzveig HM. Diffraction Effects in Semiclassical Scattering. Cambridge University Press; 2006.
[61] Khare V, Nussenzveig HM. Theory of the Glory. Phys Rev Lett 1977;38:1279–82. https://doi.org/10.1103/PhysRevLett.38.1279.
[62] Mackowski DW, Mishchenko MI. A multiple sphere T-matrix Fortran code for use on parallel computer clusters. Journal of Quantitative Spectroscopy and Radiative Transfer 2011;112:2182–92. https://doi.org/10.1016/j.jqsrt.2011.02.019.
[63] Johnson B. Invariant Imbedding T-Matrix Approach to Electromagnetic Scattering. Appl Optics 1988;27:4861–73. https://doi.org/10.1364/AO.27.004861.
[64] Bi L, Yang P, Kattawar GW, Mishchenko MI. Efficient implementation of the invariant imbedding T-matrix method and the separation of variables method applied to large nonspherical inhomogeneous particles. J Quant Spectrosc Radiat Transf 2013;116:169–83. https://doi.org/10.1016/j.jqsrt.2012.11.014.
[65] Bi L, Yang P, Kattawar GW, Mishchenko MI. A numerical combination of extended boundary condition method and invariant imbedding method applied to light scattering by large spheroids and cylinders. J Quant Spectrosc Radiat Transf 2013;123:17–22. https://doi.org/10.1016/j.jqsrt.2012.11.033.
[66] Bi L, Yang P. Accurate simulation of the optical properties of atmospheric ice crystals with the invariant imbedding T-matrix method. J Quant Spectrosc Radiat Transf 2014;138:17–35. https://doi.org/10.1016/j.jqsrt.2014.01.013.
[67] Sun B, Yang P, Kattawar GW, Zhang X. Physical-geometric optics method for large size faceted particles. Opt Express 2017;25:24044–60. https://doi.org/10.1364/OE.25.024044.
[68] Maughan JB, Chakrabarti A, Sorensen CM. Rayleigh scattering and the internal coupling parameter for arbitrary particle shapes. J Quant Spectrosc Radiat Transf 2017;189:339–43. https://doi.org/10.1016/j.jqsrt.2016.12.004.
[69] Baran AJ. A review of the light scattering properties of cirrus. Journal of Quantitative Spectroscopy and Radiative Transfer 2009;110:1239–60. https://doi.org/10.1016/j.jqsrt.2009.02.026.
[70] Liou K-N, Yang P. Light Scattering by Ice Crystals: Fundamentals and Applications. Cambridge University Press; 2016.
[71] Sorensen CM, Yon J, Liu F, Maughan J, Heinson WR, Berg MJ. Light scattering and absorption by fractal aggregates including soot. Journal of Quantitative Spectroscopy and Radiative Transfer 2018;217:459–73. https://doi.org/10.1016/j.jqsrt.2018.05.016.
[72] Medalia AI, Heckman FA. Morphology of aggregates—II. Size and shape factors of carbon black aggregates from electron microscopy. Carbon 1969;7:567–82. https://doi.org/10.1016/0008-6223(69)90029-3.
[73] Medalia AI. Morphology of aggregates: I. Calculation of shape and bulkiness factors; application to computer-simulated random flocs. Journal of Colloid and Interface Science 1967;24:393–404. https://doi.org/10.1016/0021-9797(67)90267-6.
[74] Oh C, Sorensen CM. The Effect of Overlap between Monomers on the Determination of Fractal Cluster Morphology. Journal of Colloid and Interface Science 1997;193:17–25. https://doi.org/10.1006/jcis.1997.5046.

[75] Pierce F, Sorensen CM, Chakrabarti A. Computer simulation of diffusion-limited cluster-cluster aggregation with an Epstein drag force. Phys Rev E 2006;74:021411. https://doi.org/10.1103/PhysRevE.74.021411.
[76] Sorensen CM. The Mobility of Fractal Aggregates: A Review. Aerosol Science and Technology 2011;45:765–79. https://doi.org/10.1080/02786826.2011.560909.
[77] Mishchenko MI, Liu L, Mackowski DW, Cairns B, Videen G. Multiple scattering by random particulate media: exact 3D results. Opt Express, OE 2007;15:2822–36. https://doi.org/10.1364/OE.15.002822.
[78] Muinonen K, Zubko E, Tyynela J, Shkuratov YG, Videen G. Light scattering by Gaussian random particles with discrete-dipole approximation. J Quant Spectrosc Radiat Transf 2007;106:360–77. https://doi.org/10.1016/j.jqsrt.2007.01.049.
[79] Munoz O, Volten H, Hovenier JW, Nousiainen T, Muinonen K, Guirado D, et al. Scattering matrix of large Saharan dust particles: Experiments and computations. J Geophys Res-Atmos 2007;112:D13215. https://doi.org/10.1029/2006JD008074.
[80] Zubko E, Muinonen K, Shkuratov Y, Videen G, Nousiainen T. Scattering of light by roughened Gaussian random particles. J Quant Spectrosc Radiat Transf 2007;106:604–15. https://doi.org/10.1016/j.jqsrt.2007.01.050.

Appendix A - Shape Definitions

Spheroids are formed by rotating an ellipse around one of its principle axes and are defined by

$$\frac{x^2 + y^2}{a^2} + \frac{z^2}{c^2} = 1. \tag{A.1}$$

By the definition of Eq. (A.1) the ellipse would be rotated around c, and the other principle axis is a. The aspect ratio of a spheroid is defined by

$$\varepsilon = \frac{c}{a}. \tag{A.2}$$

When the aspect ratio is less than one the spheroid is said to be oblate, and when the aspect ratio is greater than one it is prolate. The volume of a spheroid is given by

$$V = \frac{4}{3}\pi a^2 c, \tag{A.3}$$

and the surface area can be approximated by

$$S \approx 4\pi \left[\frac{(a^2)^p + 2(ac)^p}{3}\right]^{\frac{1}{p}}, \tag{A.4}$$

with p~1.6075. Fig. A.1 shows spheroids with aspect ratios less than, greater than, and equal to unity.

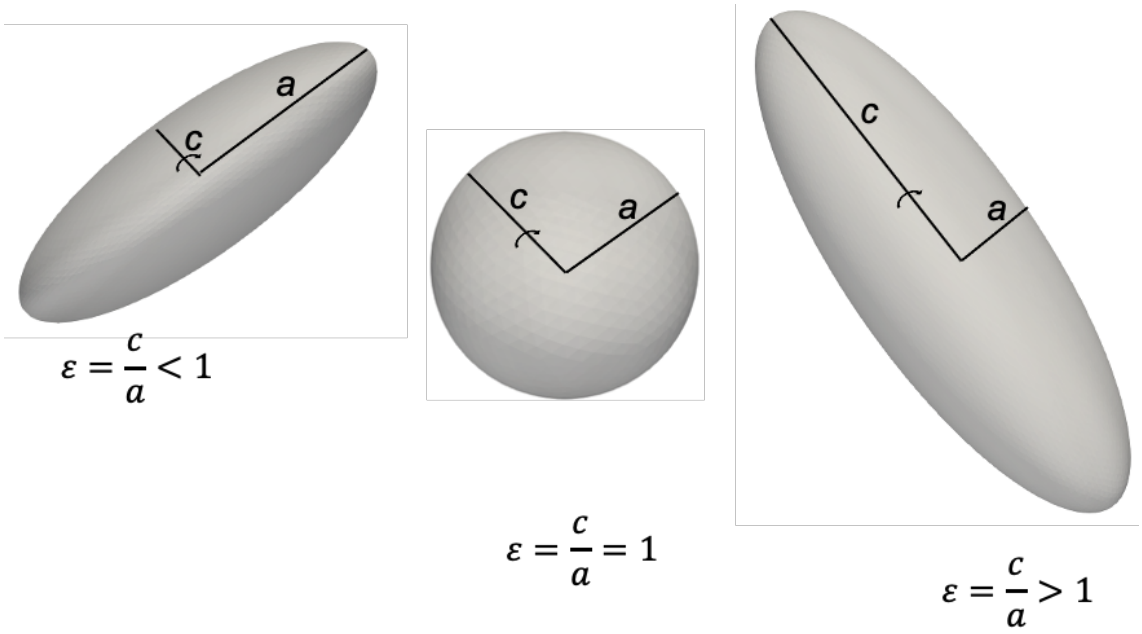

Fig. A.1 Examples of spheroids with aspect ratios $\varepsilon < 1$, $\varepsilon = 1$, and $\varepsilon > 1$.

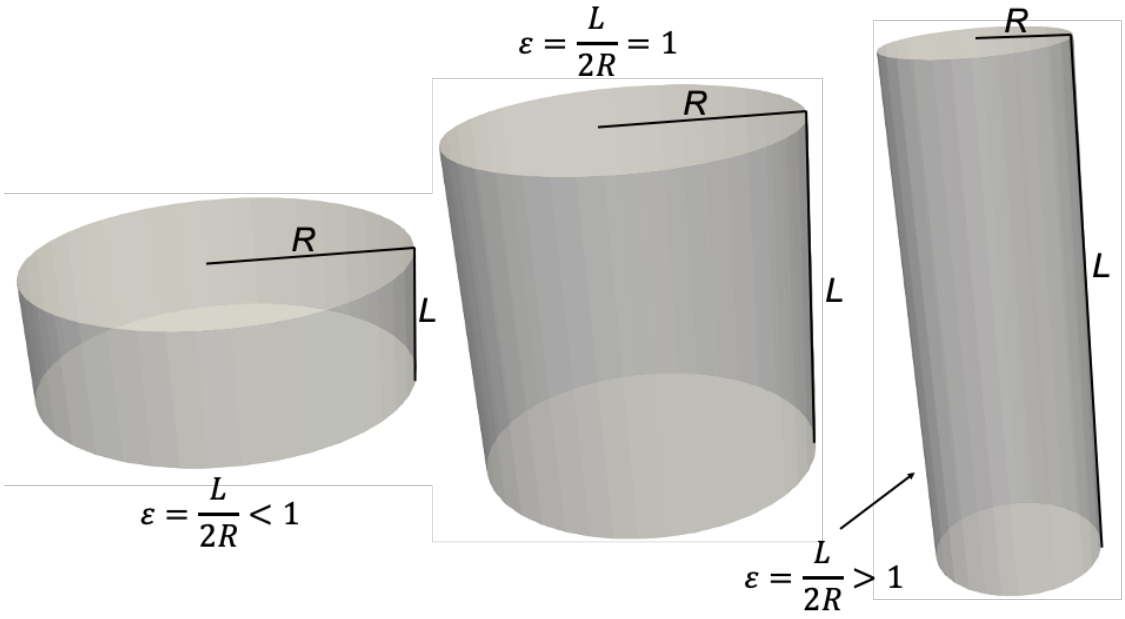

Fig. A.2 Examples of cylinders with aspect ratios $\varepsilon < 1$, $\varepsilon = 1$, and $\varepsilon > 1$.

Cylinders are defined by a radius R and height L, and have an aspect ratio defined by

$$\varepsilon = \frac{L}{2R}. \tag{A.5}$$

The volume of a cylinder is given by

$$V = \pi R^2 L, \tag{A.6}$$

and the surface area is given by

$$S = 2\pi R^2 + 2\pi RL. \tag{A.7}$$

Fig. A.2 shows cylinders with aspect ratios less than, greater than, and equal to unity.

Hexagonal columns are defined by a side length a and height h, and have an aspect ratio defined by

$$\varepsilon = \frac{h}{2a}. \tag{A.8}$$

The volume of a hexagonal column is given by

$$V = \frac{3\sqrt{3}}{2} a^2 h \tag{A.9}$$

and the surface area is given by

$$S = 6ah + 3\sqrt{3}a^2 \tag{A.10}$$

Fig. A.3 shows hexagonal columns with aspect ratios less than, greater than, and equal to unity.

Rectangular columns are defined by a side length b and height a, and have an aspect ratio defined by

$$\varepsilon = \frac{a}{b}. \tag{A.11}$$

The volume of a rectangular column is given by

$$V = b^2 a \tag{A.12}$$

and the surface area is given by

$$S = 2b^2 + 4ab \tag{A.13}$$

Fig. A.4 shows rectangular columns with aspect ratios less than, greater than, and equal to unity.

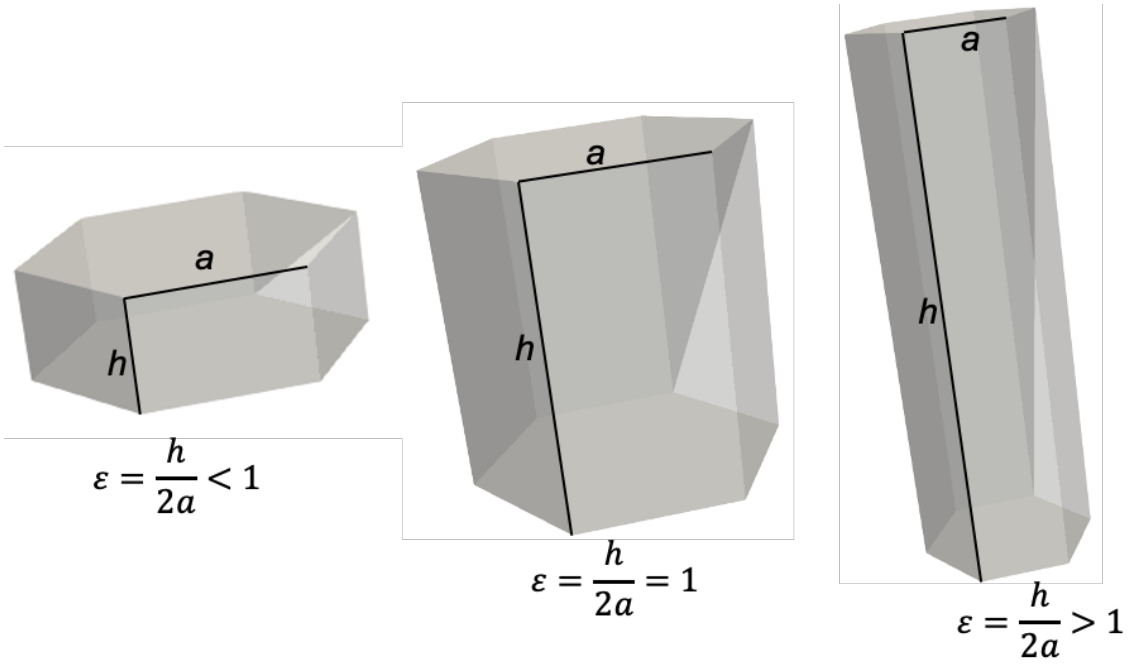

Fig. A.3 Examples of hexagonal prisms with aspect ratios $\varepsilon < 1$, $\varepsilon = 1$, and $\varepsilon > 1$.

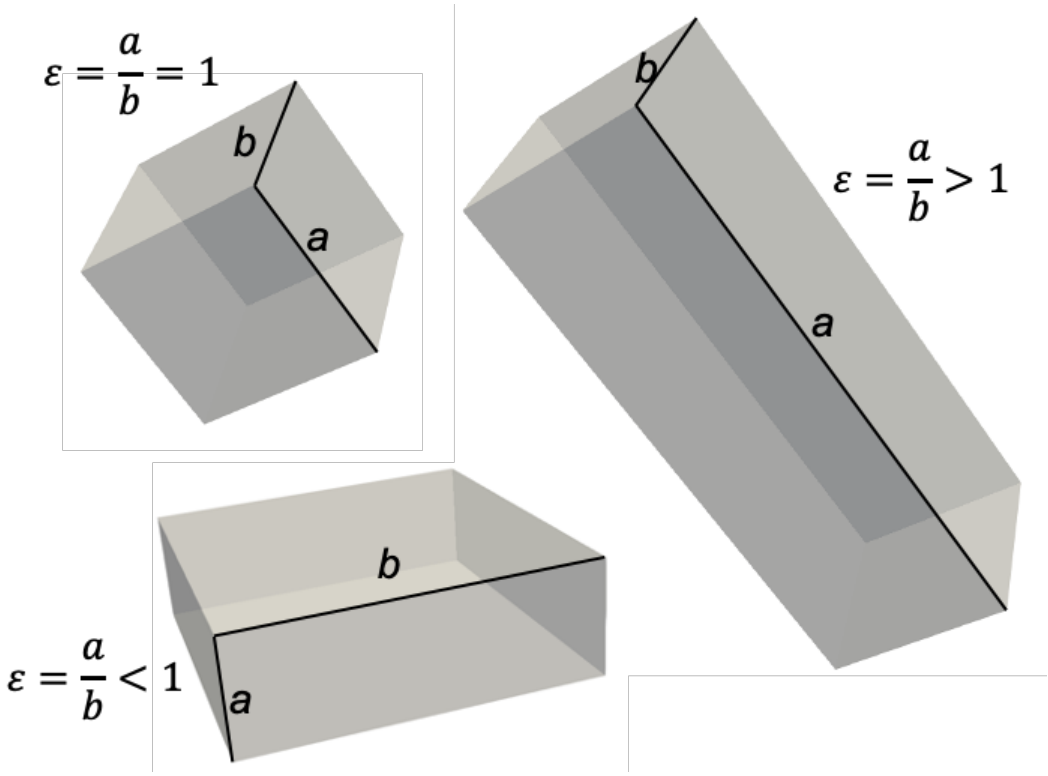

Fig. A.4 Examples of rectangular prisms with aspect ratios $\varepsilon < 1$, $\varepsilon = 1$, and $\varepsilon > 1$.

Gaussian random spheres (GRS) are defined by a mean radius a, a relative standard deviation σ, and a power law index ν [78–80]. There is not a clear definition of the aspect ratio as GRS are randomly perturbed spheres. The ensemble-averaged volume is given by

$$\langle V \rangle = \frac{4\pi}{3}[a(1+\sigma^2)]^3, \tag{A.14}$$

and the volume equivalent surface area of a sphere will be used. The relative standard deviation σ effects the size of the random fluctuations away from the mean radius, the larger σ is the less spherical the shape will be. The power law index effects the number of random fluctuations in a direction tangential to the radius, the smaller ν is the less spherical the shape will be. Fig. A.5 shows several examples of shapes with variations of ν and σ.

Droxtals are defined by the circumscribing sphere radius R, and two angles θ_1, and θ_2 [34]. Further parameters that describe the sphere and are dependent on R, θ_1, and θ_2, are shown in Fig. A.6 and are given by

$$a_1 = R\sin(\theta_1), \tag{A.15}$$

$$a_2 = R\sin(\theta_2), \tag{A.16}$$

$$L_1 = R\cos(\theta_1), \tag{A.17}$$

$$L_2 = R\cos(\theta_2), \tag{A.18}$$

and

$$h = \frac{a_1}{(a_2 - a_1)}(L_1 - L_2). \tag{A.19}$$

The volume of a droxtal is given by

$$V = \sqrt{3}[(h + L_1 + 2L_2)a_2^2 - ha_1^2], \tag{A.20}$$

and the surface area is given by

$$S = 3\sqrt{3}a_1^2 + 12L_2a_2 + 6(a_1 + a_2)\sqrt{\frac{3}{4}(a_2 - a_1)^2 + (L_2 - L_1)^2}. \tag{A.21}$$

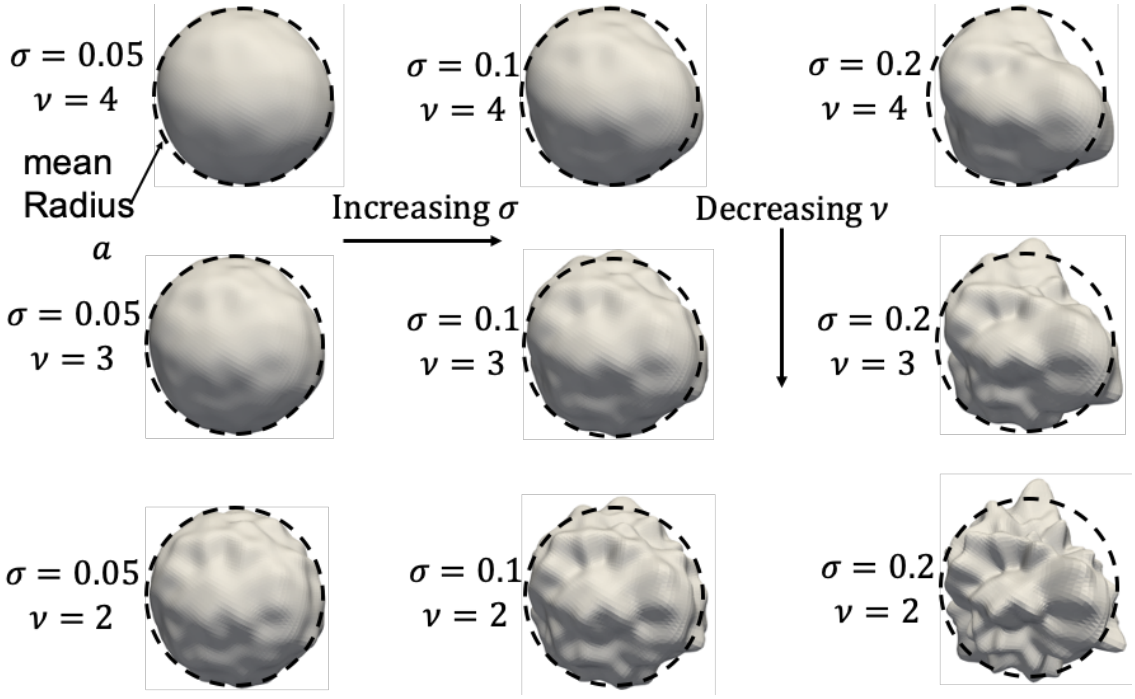

Fig. A.5 Examples of Gaussian random spheres with relative standard deviations of $\sigma = 0.05, 0.1, 0.2$, power law indexes of $\nu = 2, 3, 4$ and mean radius of a.

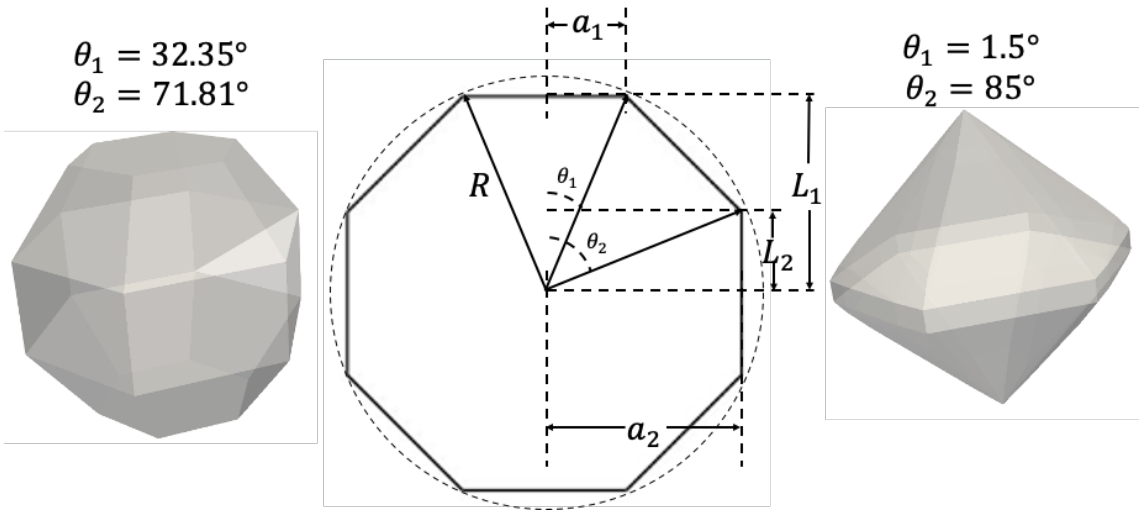

Fig. A.6 Examples of droxtals with circumscribing sphere radius of R, and angle $\theta_1 = 32.35°, 1.5°$ and $\theta_2 = 71.81°,\ 85°$.

Examples of droxtals with $\theta_1 = 32.35°$, $\theta_2 = 32.35°$, $\theta_1 = 1.5°$, and with $\theta_2 = 85°$ are shown in Fig. A.6. The other extreme with $\theta_1 \sim \theta_2$ leads to a hexagonal column which has already been described.